WAVELENGTH-AGILE RAYLEIGH SCATTERING

BY USE OF AN ATOMIC VAPOR CELL

by

Amanda Jo Pertzborn

A thesis submitted in partial fulfillment of the

requirements for the degree of

Masters of Science

(Mechanical Engineering)

at the

UNIVERSITY OF WISCONSIN - MADISON

Abstract

A wavelength-agile technique using an atomic vapor cell is developed and applied to the measurement of Rayleigh scattering. The atomic vapor cell displays a steep change in refractive index as a function of wavelength, thereby creating a wavelength scan over a narrow spectral range. This scan can be utilized for high resolution spectral measurements. For example, a short pulse duration laser was input into the cell and the resulting wavelength-agile scan was used to resolve a single iodine absorption feature. These measurements revealed that the atomic vapor cell distorts the input pulse shape and therefore this technique must be used with care. A wavelength-agile scan of the Rayleigh scattering spectrum was created using the atomic vapor cell; the resolved Rayleigh scattering spectrum can be compared to theory to obtain the temperature, pressure, and velocity of the scattering medium.

The overall goal of this research was to direct light scattered by the gas in a vortex tube into the atomic vapor cell in order to create a wavelength-agile Rayleigh scattering spectrum. The temperature, pressure, and velocity at the scattering location would be resolved from the results of this time-of-flight technique. In this research only the scattering in a fiber was measured due to experimental difficulties. The results of this measurement indicate that this wavelength-agile Rayleigh scattering technique is difficult. Rayleigh scattering is extremely weak and therefore difficult to measure while the atomic vapor cell distorts the light passing through it.

Acknowledgements

I would like to thank my advisor, Dr. Scott Sanders, for showing great patience and answering numerous questions. I also want to acknowledge the efforts of Dr. Joachim Walewski who took the time to explain some physics to an engineer. The faculty and staff in the ERC and the Mechanical Engineering department also provided excellent instruction and were always ready to help when needed.

Thanks also go to all my lab mates who tolerated my large optical setups and occasional requests for a dark lab. I would like to particularly thank my office mates Natalie Bednar and Chris Hagen. Natalie performed the Zemax ray tracing analyses for many parts of this research and Chris was always willing to throw around ideas.

Finally, I want to thank my family and friends who were always supportive of my return to school. I single out my room mates Matt Malecki, Jim Reichling, and Tenley Banik for putting up with me when I hit bumps in the road and providing entertaining distractions.

This material is based upon work supported by the National Science Foundation under Grant No. CTS-0242219.

Table of Contents

List of Figures

List of Tables

List of Symbols

Universal Symbols

c	speed of light in a vacuum $3*10^{8}$ [m/s]
h	Planck's constant $6.63*10^{-34}$ [Js]
k_b	Boltzmann's constant $1.38*10^{-23}$ [J/K]
q	elementary charge $1.602*10^{-19}$ [C]
T	temperature [K]
π	pi (3.14159)

Chapter 2 Scattering

a	speed of sound [m/s]
c_p	specific heat at constant pressure [J/kg-K]
c_v	specific heat at constant volume [J/kg-K]
$d\sigma/d\Omega$	differential scattering cross section [m^2/molec-sr]
$d\sigma/d\Omega_{Rayleigh}$	Rayleigh scattering
$d\sigma/d\Omega_{Raman}$	Raman scattering
$d\sigma/d\Omega_{Mie}$	Mie scattering
etalam	input to S6 code, ratio of shear viscosity to thermal conductivity [kg]
etazet	input to S6 code, ratio of shear viscosity to bulk viscosity
K	constant used in theoretical scattering model
k	thermal conductivity [W/m-K]
L	length of scattering volume [m]
m	mass of scatterer [kg]
N	number of scatterers number density [m^{-3}]
n	number density [m^{-3}] index of refraction
N_o	number density at standard temperature and pressure [m^{-3}]
$\dot{N}_i$	incident photon flux [photons/s]
$\dot{N}_s$	scattered photon flux [photons/s]
P_i	incident power [W]
P_s	scattered power [W]
Q	scattering efficiency
v	speed of scatterer [m/s]
v_o	thermal velocity [m/s]
x	x-units output by S6 model
y	ratio of mean free path to characteristic length of scattering volume
$\Delta\lambda$	Doppler shift of light [nm]
$\Delta\nu$	frequency shift of acoustic sidebands [Hz]
δA	differential cross sectional area [m^2]

η	shear viscosity [kg/m-s]
θ	angle of scattering [rad]
λ	wavelength [m]
λ_o	wavelength of primary light [nm]
ν	primary radiation [Hz]
σ	total scattering cross section [m^2]
σ_{geo}	total geometric scattering cross section
ϕ	angle of observation [rad]
Ω	solid collection angle [sr]

Chapter 3 Spatially Resolved Measurement Techniques

d	groove spacing [m]
	etalon spacing [m]
F	finesse
FSR	Free Spectral Range [Hz]
m	order of interference , integer value
N	number of illuminated grooves
n	index of refraction
R	reflectivitiy
T	transmission
α	angle of incidence [rad]
β	angle of reflectance [rad]
$\Delta\lambda$	resolution [m]
δ	phase shift [rad]
θ	etalon internal angle of incidence [rad]
λ	wavelength [m]
$\lambda/\Delta\lambda$	resolving power

Chapter 4 Atomic Vapor Cell

^{41}K	potassium isotope
^{39}K	potassium isotope
A	constant in hyperfine splitting calculations
B	constant in hyperfine splitting calculations
E_{Dipole}	energy of the dipole
E_J	initial energy level
$E_{quadrupole}$	energy of the quadrupole
F	total angular momentum of an atom
f	oscillator strength
I	angular momentum of nucleus
J	total angular momentum of an electron
K	equation used in hyperfine splitting calculations
L	cell length [m]
	total orbital angular momentum

m	mass of potassium [kg]
m_e	mass of an electron [kg]
N	number density [m^{-3}]
$\tilde{n}$	complex index of refraction
S	axial angular momentum of an electron
t_{delay}	excess time delay [s]
V_g	group velocity [m/s]
v_p	most probable speed [m/s]
α	absorbance
γ	Lorentzian FWHM [rad/s]
Δn	height of index of refraction
$\Delta\nu$	separation between hyperfine lines [MHz]
ε_o	permittivity of free space [C^2/N-m^2]
κ	extinction coefficient
κ_{max}	maximum extinction coefficient
ν	frequency [Hz]
χ	electric susceptibility
ω_o	potassium line center [rad/s]
ω_a	variable of integration [rad/s]
ω	local frequency [rad/s]

Chapter 5 Experimental Setup

B	bandwidth [Hz]
I	signal after passage through both potassium AVC and iodine
I_{dc}	steady current [A]
I_{noise}	shot noise [A]
I_o	signal after passage through just potassium AVC
N_b	number of counts due to the background
N_d	number of counts due to the PMT dark noise
N_{ph}	number of counts due to the signal light
N'_b	number of counts due to the background per second
N'_d	number of counts due to the PMT dark noise per second
N'_{ph}	number of counts due to the signal light per second
n_b	shot noise associated with the background
n_d	shot noise associated with the PMT dark noise
n_{ph}	shot noise associated with the signal
n_{tot}	total noise associated with the measurement
P_o	incident power at the detection limit [W]
SNR	signal-to-noise ratio
α	absorbance
η	quantum efficiency [%]
λ	wavelength [nm]

σ responsivity of photocathode [mA/W]

Appendix A Glossary

Aik Einstein A coefficient for transitions from energy level *i* to *k* [s^{-1}]
Ajk Einstein A coefficient for transitions from energy level *j* to *k* [s^{-1}]
G Gaussian profile
L Lorentzian profile
M molecular weight [g/mole]
P pressure [Pa]
f frequency [Hz]

2γ collisional broadening coefficient [Hz/Pa]
Δf FWHM of a profile [Hz]
$\Delta\lambda$ FWHM of a profile [nm]
$\Delta\nu$ FWHM of a profile [Hz]
FWHM of a profile [cm-1]
$\Delta\nu_c$ FWHM of collisional broadening [Hz]
$\Delta\nu_D$ FWHM of Doppler broadening [Hz]
$\Delta\nu_N$ FWHM of natural broadening [Hz]
λ wavelength [nm]
ν frequency [Hz]
wavenumber [cm^{-1}]
ν_o center frequency [Hz]

Appendix B Etendue

a_1 radius of the beam at location 1 [m]
a_2 radius of the beam at location 2 [m]

θ_1 divergence angle at location 1 [rad]
θ_2 divergence angle at location 2 [rad]

Appendix D Uncertainty

A generic dependent variable
B generic independent variable
C generic independent variable
I signal after passage through both potassium AVC and iodine
I_o signal after passage through just potassium AVC
T temperature of potassium [K]
a assemblage of constants in Doppler width equation [$cm^{-1}/K^{1/2}$]
div measurement of FWHM in terms of data points [point]
sf scale factor to convert from points to color [cm^{-1}/point]
u_A uncertainty of generic dependent variable
u_B uncertainty of generic independent variable
u_C uncertainty of generic independent variable

u_I uncertainty of I measurement
u_{Io} uncertainty of I_o measurement
u_T uncertainty of temperature measurement [K]
u_{div} uncertainty of estimate of FWHM in data points [point]
u_{sf} uncertainty of scale factor measurement [cm^{-1}/point]
u_α uncertainty of absorbance measurement
$u_{\Delta\nu}$ uncertainty of Doppler width measurement [cm^{-1}]

α absorbance
$\Delta\nu$ Doppler width of potassium [cm^{-1}]

Appendix F Dispersion in Solids and Liquids

B1 constant in Sellmeir equation
B2 constant in Sellmeir equation
B3 constant in Sellmeir equation
C1 constant in Sellmeir equation
C2 constant in Sellmeir equation
C3 constant in Sellmeir equation
k spectral absorption coefficient [m^{-1}]
L length [m]
n index of refraction

λ wavelength [μm]
τ transmittance

Appendix G Synthetic Measurement Data

Amp amplitude, fitting parameter
center location of center of Gaussian curve, fitting parameter
$center_{act}$ specified center value
$center_f$ fit center value
FWHM full width at half maximum of Gaussian curve, fitting parameter
$FWHM_{act}$ FWHM based on set parameters
$FWHM_f$ specified FWHM value
lsq equation data is fit to
T_f temperature based on fit [K]
T_{act} temperature based on set parameters [K]
t arrival time [ns]
y number of electrons
$y_{calculated}$ calculated y value
$y_{measured}$ measured y value

σ weighting parameter

List of Acronyms

AVC	Atomic Vapor Cell
CCD	Charge-Coupled Device
CRBS	Coherent Rayleigh Brillouin Scattering
ENI	Equivalent Noise Input
ETC	Extremely Thin Cell
FSR	Free Spectral Range
FWHM	Full Width at Half Maximum
GVD	Group Velocity Dispersion
HFS	HyperFine Splitting
IC	Internal Combustion
MDA	Minimum Detectable Absorbance
NEP	Noise Equivalent Power
PMT	PhotoMultiplier Tube
QE	Quantum Efficiency
SNR	Signal-to-Noise Ratio
STP	Standard Temperature and Pressure
UV	UltraViolet
VUV	Vacuum UltraViolet

Chapter 1 Introduction

Temperature, pressure, and velocity are parameters which can be used to understand a flow or chemical reaction. In some situations an invasive probe such as a pitot tube, hot wire anemometer, or flow meter can directly sample the measurement volume without significantly affecting the measurement. In a device such as a vortex tube this is not the case. In a vortex tube a gas, commonly compressed air, is injected into the side of one end of a tube and then forced into a vortex flow [1]. Some of the flow exits at the far end of the tube at a higher temperature than the input flow while the rest exits at the near end of the tube, where the flow was injected, at a lower temperature than the input flow. If any device is placed into the flow stream it will disrupt the flow and any measurement of temperature, pressure, or velocity will not reflect the uninterrupted flow in the vortex tube. Therefore, it is preferable to make non-invasive measurements, although invasive measurements can provide some useful information. The measurements also need to be spatially resolved if any conclusions are to be drawn.

There are several laser based techniques for measuring temperature, pressure, and velocity which are less invasive than traditional techniques. Some techniques require introducing seeding particles into the flow, but the centrifugal force of the vortex pushes these particles to the exterior of the flow, limiting the usefulness of these measurements in a vortex tube. Absorption spectroscopy is a common and well understood technique from which temperature and pressure can be determined, but often the result is not spatially resolved. This is not true in the case of absorption tomography, but this method can not be used in a vortex tube due to edge effects. Fluorescence spectroscopy, which is

related to absorption spectroscopy, can also be used to obtain point measurements, but it can not practically provide velocity measurements.

Scattering is another technique for making spatially resolved, non-invasive measurements [2]. Two examples of scattering are Raman scattering and Rayleigh scattering. Raman scattering changes the internal energy of the molecule it interacts with while Rayleigh scattering does not. Raman scattering is commonly used to obtain information about temperature, pressure, and species in a measurement volume [3]. Rayleigh scattering is approximately 1000 times more intense than Raman scattering and it provides velocity information in addition to temperature and pressure. This research has focused on developing a method to measure the Rayleigh scattering spectrum in a system such as a vortex tube.

The measurement of the Rayleigh scattering spectrum is nontrivial due to the weak nature of the signal as well as the narrow width of the spectrum. In order to obtain the most useful information the spectrum must be resolved, therefore a sensitive, high resolution measurement system is required. Past measurements have used an etalon, but the resolution of those measurements is questionable. In this research an atomic vapor cell (AVC) was used to create a wavelength-agile source. Near a strong absorption line the variation in the index of refraction is extreme. The speed with which light travels is a function of the index of refraction of the medium as well as the color of the light, therefore as the index of refraction changes so does the speed of light. Each color is affected differently, so the result is a wavelength-agile Rayleigh scattering spectrum; the different colors in the spectrum have been temporally separated so that the spectrum can be measured on an oscilloscope. The resulting measurement is then analyzed. The

temperature and pressure are determined from the shape of the spectrum and the velocity is determined from the frequency shift of the spectrum with respect to the laser frequency.

There were two ultimate goals to this research; one was to create a method for measuring the Rayleigh scattering spectrum and the second was to apply that method to the measurement of temperature, pressure, and velocity in a vortex tube. Due to complications in the first goal, the second goal was left unaccomplished. This report is organized into several sections, starting with background regarding the technique developed for making these measurements followed by some results and a discussion of the usefulness of the technique.

Chapter 2 Scattering

Two important interactions between light and molecules are absorption and scattering, both of which result in attenuation [4]. Absorption is the stronger process (in terms of signal measurement) in which a photon excites an atom or molecule to a higher energy level, but only if the energy of the photon matches the separation between the energy levels. After a finite period of time the atom relaxes to a less energetic state via collisions with particles, interaction with another photon, etc. Scattering occurs instantaneously and is a continuous process which ceases when the light source is turned off. The photon can have any energy; the scattering process is generally independent of the energy levels of the scatterer. In the classical picture of scattering the electric field of the light causes the electron cloud to oscillate with respect to the nucleus of the scatterer, which is an atom, molecule, or particle. This creates an oscillating dipole which results in emission from the scatterer. The incident light is the primary, driving field and the scattered light is the secondary field. The secondary field has the same wavelength (energy) as the primary field in elastic scattering. If the incident light is polarized then the scattered light will have the same polarization. In the case of scattering from a small particle, even when the incident light is depolarized, when the scattered light is observed at 90° from the primary beam path it is almost perfectly polarized [2].

2.1 Types of scattering

There are many types of scattering, but only three will be discussed here. The first is Mie scattering, which is the most intense. Mie scattering is elastic; the internal

energy of the scatterer remains unchanged when it interacts with the photon. The scattered, or secondary, light has the same energy as the incident, or primary, light when the scatterer is stationary. If the scatterer is moving away from the light source the secondary light will be red-shifted; it will be less energetic than the primary light and the kinetic energy of the scatterer will increase accordingly. The scatterers in this case are particles with dimensions larger than the wavelength of the primary light. The properties of the scattered light depend on the scatterer, so the details of Mie scattering are left to other sources while several characteristics are mentioned here. First, the strength of Mie scattering is altered very little by changes in the wavelength of the primary light. This is the reason that clouds are white; the particles scatter all wavelengths of light equally. Scattering in the forward direction is also dominant for these large particles. These characteristics change once the scatterer size becomes smaller [2].

Raman scattering occurs when the wavelength of light is at least ten times the radius of the scatterer, and in this case light is scattered evenly in the forward and backward directions [2]. Unlike Mie scattering, Raman scattering is inelastic; the internal energy of the molecule changes. Raman scattering occurs due to the presence of rotational and vibrational energy levels. The creation of the oscillating dipole can be represented as exciting the electrons to a virtual state, as in Figure 2-1 (b) [4]. The relaxation process is instantaneous, but instead of returning to the initial energy level the electron may return to a lower or higher energy level. The resulting secondary radiation is more (anti-Stokes) or less (Stokes) energetic than the primary radiation, resulting in a frequency shift. This shift is useful because noise due to background scattering, Mie scattering, reflections, etc. can be filtered out of the signal, leaving only Raman

scattering. Raman scattering probes the internal structure of the scatterer by measuring rotational and vibrational energy levels, therefore it can be used to identify the scattering species. Raman scattering is a weak process; the rotational S (Stokes) and S' (anti-Stokes) lines are located near the primary radiation frequency but the vibrational component extends a great distance away, on the order of thousands of wavenumbers. The Q-branch is not shifted from the primary radiation frequency; it is generated when the primary radiation re-orients the molecular spin, resulting in depolarized and incoherent light scattered at the same frequency as the primary radiation [5].

Rayleigh scattering is the third scattering type and the focus of this research. Rayleigh scattering is composed of several components, but the strongest are due to elastic interactions with an atom or molecule that is much smaller than the wavelength of light (wavelength > 0.1 times the scatterer radius). The signal strength is equal in the forward and backward directions and it is approximately 1000 times stronger than Raman scattering. Rayleigh scattering will be explored in more detail in the following sections.

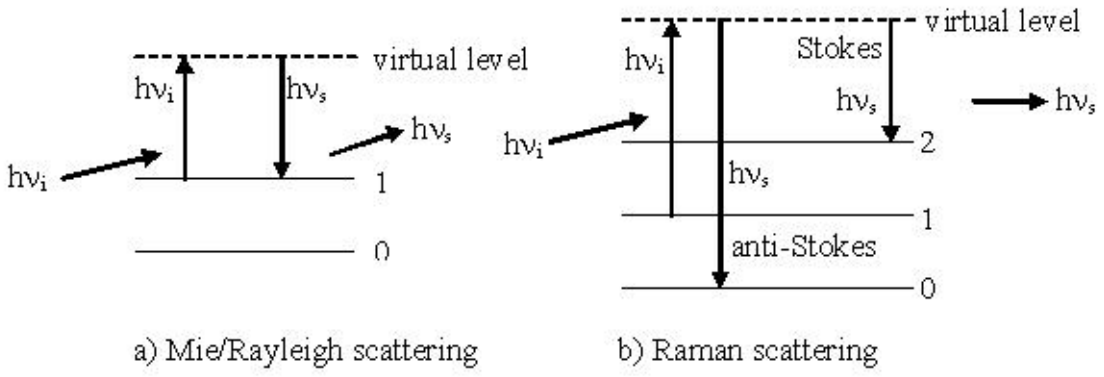

Figure 2-1 Illustration of the scattering process. The scatterer is excited to a virtual state and immediately relaxes to a lower state, emitting a photon. a) Mie and Rayleigh scattering are elastic processes in which the emitted photon has the same energy as the incident photon; b) Raman scattering is an inelastic process in which the emitted photon is more or less energetic than the incident photon.

A natural question is why use Rayleigh scattering for measurements instead of Mie or Raman scattering? Mie scattering requires particles, so it is generally used with seeded flows. In the case of a vortex tube centrifugal force moves the seeding particles to the outside of the vortex, so only the properties on the outside of the vortex can be measured. Mie scattering also measures the seeded particles, not the molecules themselves, so the information that can be gathered is somewhat limited. Raman scattering is useful because it can be used to identify a species, particularly in cases when multiple species are present. However, the likely fluids in the vortex tube are monatomic noble gases, so Raman scattering would not be present. More importantly, Rayleigh scattering is stronger than Raman scattering. The frequency shift in Raman scattering is an advantage; Mie and Rayleigh scattering occur at the same frequency, so Mie scattering can overwhelm Rayleigh scattering. However, the effects of Mie scattering can be minimized by filtering the fluid passing through the vortex tube in order to eliminate large particles. This research therefore aimed to take advantage of the strength of Rayleigh scattering as well as its ability to measure velocity. Rayleigh scattering has the advantage over absorption measurements of spatially resolved rather than line-of-sight measurements [6].

2.2 Typical uses

Mie scattering has been used to measure concentration in a reverse flow reactor [7]. Seeded particles were added to the flow and the light scattered in the forward direction was measured. Based on the intensity of the scattering, the concentration was calculated. This measurement was compared to results obtained via Raman scattering.

In the case of Mie scattering the standard deviation is large due to the agglomeration of seeding particles, interference from particles eroded from the reactor walls, and diffusion effects between the fuel and the seeding particles. The conclusion of this study is that although Mie scattering is a strong process, it is not the best method of obtaining accurate measurements. The usefulness of Mie scattering is also limited by the difficulty of uniformly seeding a flow, limitations on how many particles can be used in seeding, and the inability to make small scale observations [8]. However, Mie scattering is a useful tool for flow visualization.

Raman scattering is commonly used to identify species and calculate an air/fuel ratio in an internal combustion (IC) engine. For example, in one set of Raman scattering measurements in an IC engine the concentrations of H_2O, CO_2, CO, N_2, O_2, and fuel are measured and the air/fuel ratio is calculated from these data. Mie and background scattering are filtered, but the Raman scattering signal is weak [3].

The fuel concentration and equivalence ratio in IC engines in the absence of combustion have been calculated from the intensity of Rayleigh scattering. The technique requires filtering the air prior to the combustion chamber in order to minimize Mie scattering. In some cases the chamber walls are painted black to decrease background scattering. The measurements are generally made at 90° to the injection path and pressure is measured using a pressure transducer. The background scattering is recorded and then subtracted from the measurement in order to obtain the scattering intensity. The gas density is calculated from the intensity measurement and the ideal gas law is applied to calculate the temperature [3].

Measurements of the temperature and density in a premixed combustion zone using both Raman and Rayleigh scattering have also been made. In this experiment the two methods are compared and although the signal-to-noise ratio of the Rayleigh measurement is higher, both methods result in satisfactory data on a time-averaged basis. However, measurements are also made of turbulence. In this case Rayleigh scattering produces satisfactory temperature and density data, but the density data are less reliable. Raman scattering is not used at all for these measurements because the shot noise is too dominant. The author did note, however, that Raman scattering could probably be used with a higher power laser. The overall outcome of this experiment indicates that in an environment free of large particles, Rayleigh scattering produces better results than Raman scattering due to the higher intensity [9].

Measurements of the Rayleigh scattering spectrum have also been made. One method utilizes an optical notch frequency filter, such as iodine. In this measurement the scattered signal passes through the filter and is then imaged on a charge-coupled device (CCD). The image is a function of density (proportional to the intensity of scattering) as well as temperature, pressure, and velocity (due to the Doppler shift) because of the way that the filter overlaps the scattering line shape. The laser is tuned such that the frequency of the scattered light changes with respect to the filter. The interaction between the notch filter and the scattered light provides information about the width of the spectrum (function of temperature and pressure) and the location of the spectrum relative to the incident light (function of velocity) [8, 10].

2.3 Details of Rayleigh scattering

Some previous measurements reported in the literature do not measure the spectral shape of Rayleigh scattering; data are derived from measuring pressure in a reliable way, obtaining density from the intensity of the scattering, and then calculating the temperature based on the assumption of an ideal gas [6]. However, the scattering spectrum can provide much more information. By resolving the spectrum and fitting it to a theoretical model an estimate of temperature, pressure, density, and velocity can be made without using a secondary, invasive method to determine any of these values.

2.3.1 Spectral line shape

Before continuing it is prudent to introduce the terminology involved in a discussion of Rayleigh scattering. Figure 2-2 and Figure 2-3 show the components of scattering; part (a) of Figure 2-2 illustrates that Mie scattering is much stronger than any other scattering. Mie scattering, however, will only occur at the same time as Raman and Rayleigh scattering if large particles are present. Part (b) shows that as one spectrally magnifies the scattering the coherent and incoherent (due to anisotropy) portions of Rayleigh scattering become visible. Further magnification in part (c) shows the actual Rayleigh line, which is composed of three parts: rotational Raman scattering, which is inelastic, Q-branch Raman scattering, which is incoherent and elastic, and coherent and elastic Placzek scattering. The Cabannes line is composed of Placzek scattering and Q-branch Raman scattering. In the model used to generate these curves Q-branch Raman scattering is neglected, however the shape in part (a) of Figure 2-3 is still the Cabannes line, which has a Gaussian line shape at low pressure. Part (b) shows the Cabannes line

without the Q-branch scattering, so it is actually just the Placzek triplet, although it may occasionally be referred to as the Cabannes line in order to remain general. The Placzek triplet will be discussed in more detail, but for now it is composed of the Gross line in the center and framed by the Brillouin – Mandel'shtam doublet, which are acoustic sidebands [5, 11].

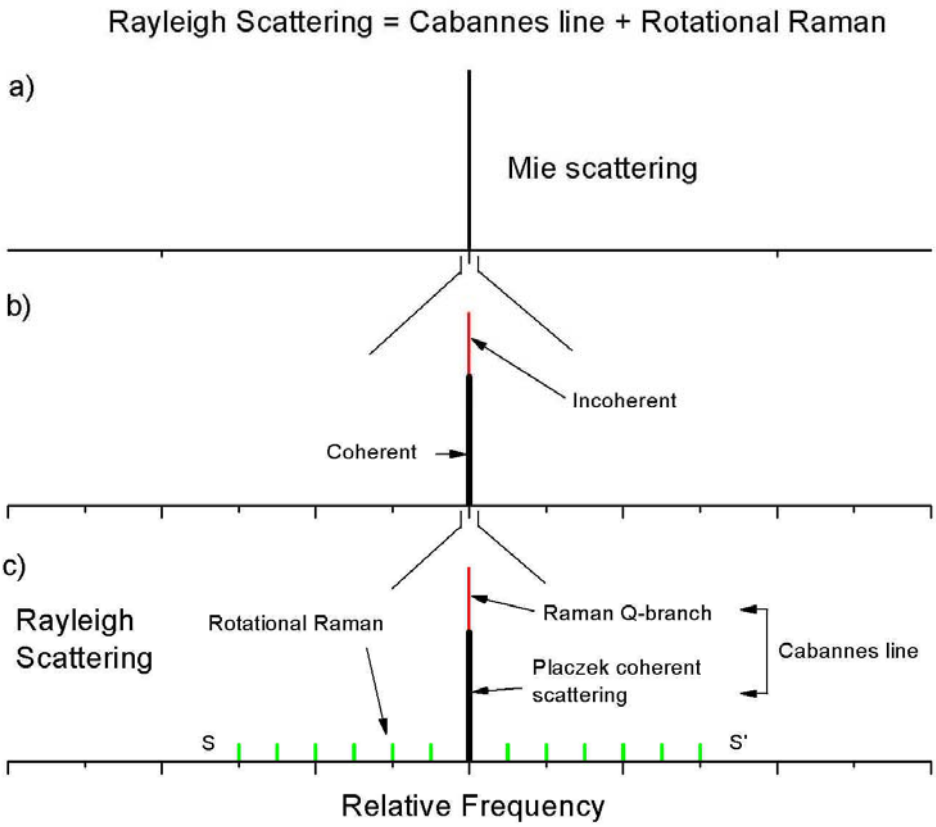

Figure 2-2 Components of scattering, not to scale. a) Mie scattering is the strongest and tends to overwhelm the other forms. Mie scattering is created only if large particles are present. b) In the case of an anistropic molecule there are coherent and incoherent portions of scattered light. c) Rayleigh scattering is composed of rotational Raman scattering, Raman Q-branch scattering, and Placzek scattering. The last two components are referred to as the Cabannes line.

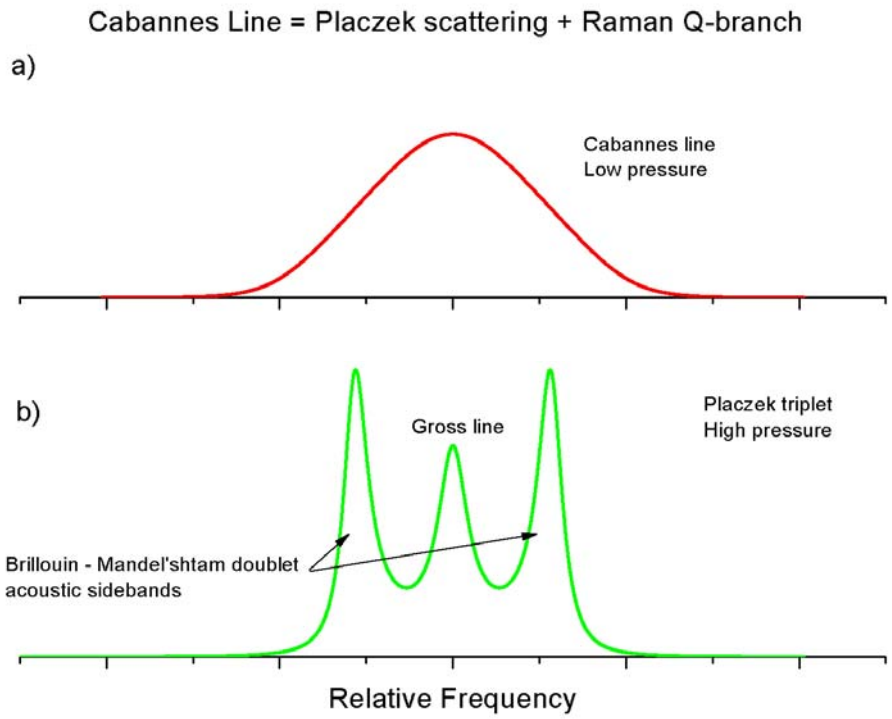

Figure 2-3 Close up of the Cabannes line of Rayleigh scattering, not to scale. a) At low pressure or high temperature the line shape is Gaussian, it is dominated by temperature effects. b) At high pressure or low temperature the Placzek triplet appears. The Brillouin-Mandel'shtam acoustic sidebands are caused by density fluctuations in the gas.

The Rayleigh scattering line shape is effectively a result of the Doppler Effect; this is the same effect that causes a passing train whistle to increase in pitch as the train approaches the observer and decrease in pitch as it recedes. When an atom moves toward a light source the scattered light is blue-shifted (more energetic) and when an atom moves away from the light source the scattered light is red-shifted (less energetic). Rayleigh scattering, therefore, "creates" more colors. The scattered spectrum is broader than the incident laser spectrum; how much broader is dependent on the condition of the scattering fluid. Figure 2-4 illustrates the effects of temperature and pressure on the shape of the Cabannes line, while Figure 2-5 further illustrates the effects of pressure. In Figure 2-4 (a) the Cabannes line shape is modeled at atmospheric pressure for a low, 300

K, and high, 600 K, temperature. At the low temperature the Placzek triplet is barely visible. As the temperature increases there is more movement within the gas and therefore an increase in the range of speeds of the atoms; this causes the breadth of the spectrum to increase due to the Doppler Effect. At low pressure the Placzek triplet is "smeared out" by the broadening. In Figure 2-4 (b) the pressure is increased by a factor of 3.4. This increase in pressure causes the amplitude of the three peaks in the Placzek triplet to increase. As temperature increases from 300 K to 600 K, although the spectrum is broadened, the triplet is still visible.

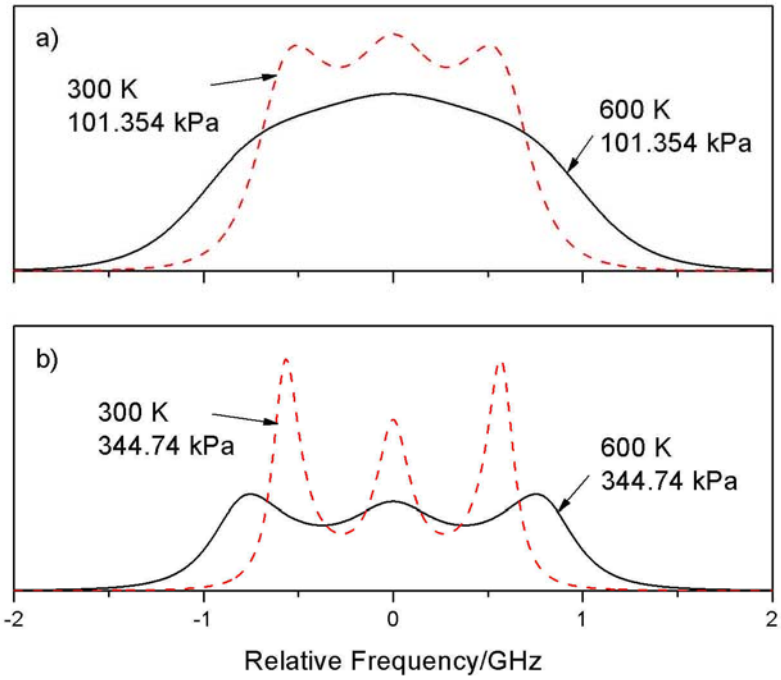

Figure 2-4 Effect of temperature and pressure on the Cabannes line. The Doppler Effect is visible as a broadening of the spectrum as temperature increases. a) At low temperature and pressure the Placzek triplet is just visible, but as temperature increases there is more movement in the gas and the spectrum is broadened. b) At a higher pressure the Placzek triplet is more defined.

In a low density or high temperature gas the mean free path is much larger than the wavelength of light, corresponding to a large Knudsen number and a thermally dominated, Gaussian line shape; the atoms rarely interact. In a high density or low

temperature gas the mean free path is much less than the wavelength of light, resulting in a small Knudsen number and therefore the gas is in the hydrodynamic regime; the atoms frequently collide. The Placzek triplet is the result of density fluctuations due to acoustic waves which are introduced by either a high pressure or a low temperature. At high pressure the three peaks are dominated by a Lorentzian line shape; the higher the pressure, the taller and sharper the peaks, as illustrated in Figure 2-5. Note, however, that the location of the peaks does not change significantly with changes in pressure. The amplitude of the peaks is primarily a pressure effect; a denser, higher pressure gas will scatter more light. The location of the peaks is primarily a temperature effect. The acoustic waves propagate at the speed of sound, therefore the density fluctuations also move at the speed of sound. The acoustic sidebands are then shifted by a frequency that is related to the speed of sound in the scattering gas by Equation (2-1) [5, 11].

$$\Delta\nu = \pm 2\nu \frac{a}{c} \sin\left(\frac{\theta}{2}\right) \tag{2-1}$$

a [m/s] is the speed of sound, θ [rad] is the angle of scattering, ν [Hz] is the frequency of the primary radiation, and c [m/s] is the speed of light in a vacuum [11]. The speed of sound in an ideal gas is proportional to the square root of the temperature.

The spectrum provides more information than just temperature and pressure. For example, the ratio of the intensity of the central peak to the total intensity of the outer peaks is equal to c_p/c_v-1 and the central peak is related to the thermal diffusion of the density fluctuations. As previously mentioned the intensity is also a function of number density.

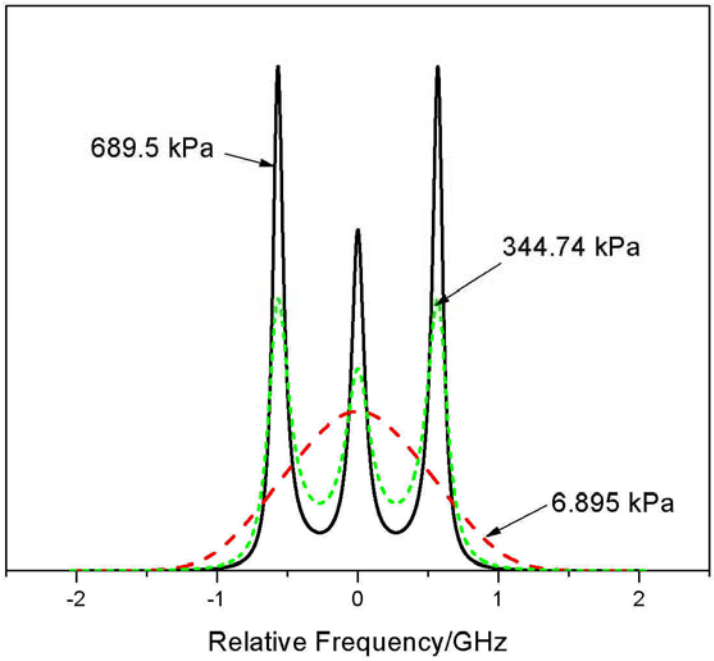

Figure 2-5 Effect of pressure on the Cabannes line. As pressure increases the Placzek triplet forms due to density fluctuations. The higher the pressure the sharper the peaks. The location of the acoustic sidebands is a function of temperature.

Velocity can be determined by examining how much the spectrum is shifted from the frequency of the primary radiation (see Figure 2-6) utilizing the Doppler Effect, presented in Equation (2-2), where $\Delta\lambda$ [nm] is the shift between the secondary and primary wavelengths, λ_o [nm] is the primary wavelength, v [m/s] is the velocity of the scattering volume (negative if it is moving toward the source), and c [m/s] is the speed of light.

$$\frac{\Delta\lambda}{\lambda_o} = \frac{v}{c} \tag{2-2}$$

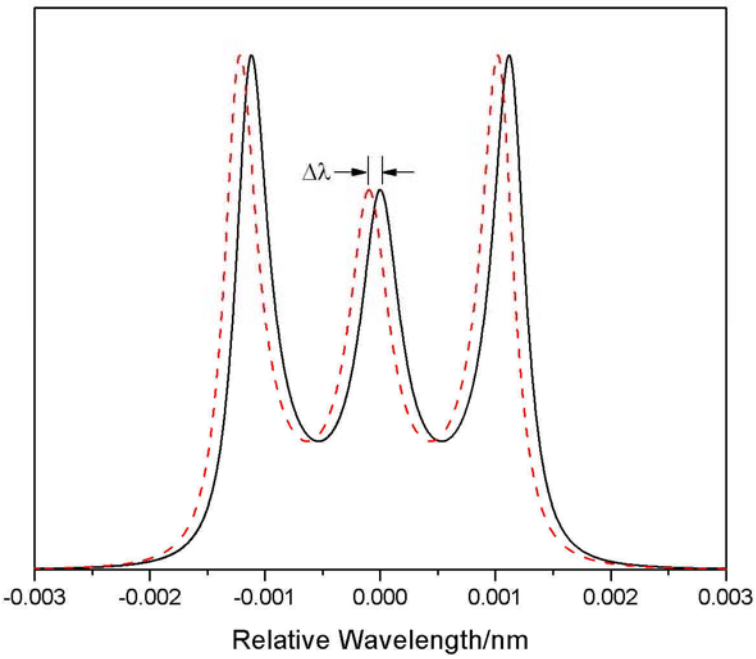

Figure 2-6 The velocity can be calculated based on the shift in the frequency of the central peak from the primary radiation. In this figure one peak is centered at zero, so the scatterer was not moving, but in the case of the other spectrum the light is red-shifted by 0.0001 nm, indicating that the scatterer was moving away from the light source at a speed of 154 m/s.

2.3.2 Calculation of scattered power

The equations used to calculate the intensity of the scattered light are now presented. The derivation is based on a differential volume of scatterers. Equations (2-3) and (2-4) are the incident, P_i [W], and scattered, P_s [W], powers, respectively.

$$P_i = \dot{N}_i h\nu \tag{2-3}$$

$$P_s = \dot{N}_s h\nu \tag{2-4}$$

$\dot{N}_i$ and $\dot{N}_s$ are the number of incident photons per second and the number of scattered photons per second on the differential cross sectional area, respectively, and $h\nu$ [J] is the energy of each photon. The number of scattered photons can be related to the number of incident photons by Equation (2-5).

$$\dot{N}_s = \frac{\dot{N}_i}{\delta A} N \frac{\partial \sigma}{\partial \Omega} \Omega \tag{2-5}$$

$$N = n \delta A L \tag{2-6}$$

The flux of photons interacting with the differential cross sectional area is $\dot{N}_i / \delta A$, where δA [m^2] is the differential cross sectional area. Each molecule has a differential cross section $d\sigma/d\Omega$ [m^2/molec-sr] and Ω [sr] is the total solid collection angle (scattering occurs over a complete sphere but only a portion of that light is collected). Steradians can be calculated from an angle in radians, θ, using Equation (2-7); this equation is only valid between 0 and $\pi/2$ radians.

$$\Omega = 2\pi\left(1 - \cos\theta\right) \tag{2-7}$$

The differential cross section is essentially the efficiency of scattering; a larger value indicates a better scatterer. The total number of scatterers in the scattering volume, N, is the number density n [m^{-3}] times the total volume, which is δA times length, L [m]. The total area of the scatterers is N times $d\sigma/d\Omega$ times Ω. Substituting Equations (2-5) and (2-6) into Equation (2-4) and dividing P_s by P_i results in the ratio of the scattered power to the incident power as described in Equation (2-8) [12].

$$\frac{P_s}{P_i} = nL \frac{\partial \sigma}{\partial \Omega} \Omega \tag{2-8}$$

This equation holds true for the three types of scattering mentioned here; the differences reside in the value of the differential cross section. Equation (2-9) is used to calculate the cross section of Rayleigh scattering in the presence of linearly polarized

light. The derivation of this equation is based on the electric field of the dipole moment of the secondary wave and the Poynting vector, as well as some geometric relationships.

$$\frac{\partial\sigma}{\partial\Omega} = \frac{9\pi^2}{N_o{}^2\lambda^4}\left(\frac{n^2-1}{n^2+2}\right)^2 \sin^2\phi \tag{2-9}$$

ϕ [rad] is the angle of observation; if this value is $\pi/2$ radians then the $sin^2\phi$ term is one. n is the index of refraction, λ [m] is the wavelength, and N_o [m^{-3}] is the number density at standard temperature and pressure ($2.69*10^{25}$ m^{-3}). If n is approximately one then the following two simplifications can be made, resulting in Equation (2-12).

$$n^2 + 2 \approx 3 \quad for\ n \approx 1 \tag{2-10}$$

$$(n^2-1)^2 \approx 4(n-1)^2 \tag{2-11}$$

$$\frac{\partial\sigma}{\partial\Omega} = \frac{4\pi^2}{N_o{}^2\lambda^4}(n-1)^2\sin^2\phi \tag{2-12}$$

The following equations are presented merely to complete the picture, but in the final calculations Equation (2-8) is used. These equations calculate the total cross sectional area by integrating the differential cross sectional area over a full sphere of 4π sr.

$$\sigma_m = \int_0^{4\pi} \frac{4\pi^2}{N_o{}^2\lambda^4}(n-1)^2\sin^2\phi\, d\Omega \tag{2-13}$$

$$d\Omega = \sin\phi d\phi d\theta \tag{2-14}$$

$$\sigma = \frac{4\pi^2}{N_o{}^2\lambda^4}(n-1)^2\int_0^{2\pi} d\theta \int_0^{\pi} \sin^3\phi\, d\phi \tag{2-15}$$

$$\sigma = \frac{32\pi^2}{3N_o{}^2\lambda^4}(n-1)^2 \tag{2-16}$$

σ [m^2] is the total scattering cross section integrated over an entire sphere and θ [rad] is the scattering angle [2].

By measuring the scattering at $\pi/2$ radians to the direction of propagation as well as using a diffuse gas in which the index of refraction is near one, the simplifications leading to Equation (2-12) result in Equation (2-17) for Rayleigh scattering. The differential cross section for Raman scattering is approximately 1/1000 that of the Rayleigh scattering differential cross section (Equation (2-18)), indicating that Raman scattering is that much weaker. The equation for Mie scattering, Equation (2-19), is different because it applies only to large particles. In this case the geometric scattering cross section is based on the size of the scatterer and the value Q, which is the scattering efficiency, is the ratio of the total scattering cross section to the geometric cross section, σ_{geo}.

$$\frac{\partial\sigma}{\partial\Omega}_{Rayleigh} = 4\pi^2 \frac{(n-1)^2}{N_0^2 \lambda^4} \tag{2-17}$$

$$\frac{\partial\sigma}{\partial\Omega}_{Raman} \approx 0.001 \frac{\partial\sigma}{\partial\Omega}_{Rayleigh} \tag{2-18}$$

$$\frac{\partial\sigma}{\partial\Omega}_{Mie} = \frac{Q\sigma_{geo}}{4\pi} \tag{2-19}$$

2.3.3 Generation of Rayleigh spectral shape

The line shapes in Figure 2-5 were generated using what is considered the best model at present for monatomic gases [5, 13], the S6 model developed by Tenti, et al. [14]. This model neglects the central Raman Q-branch scattering and assumes a single species. The vertical axis of the output is in arbitrary units and the horizontal axis is in x-units. Comparisons with experiments have shown that the model is accurate for monatomic gases but inexact for diatomic gases. One input into this model is a y parameter, presented in Equation (2-20), which behaves like the inverse of the Knudsen

number; if $y>>1$ the gas is in the hydrodynamic limit and if $y<<1$ the gas is in the thermal limit.

$$y = \frac{Nk_bT}{|K|v_o\eta\sqrt{2}} \tag{2-20}$$

The y parameter is the ratio of the characteristic length of the scattering volume to the mean free path, but it can be approximated by Equation (2-20), where N [m^{-3}] is the number density, k_b [J/K] is Boltzmann's constant, T [K] is the temperature of the scatterer and η [kg/m-s] is the shear viscosity. K [m^{-1}] is a constant related to the angle of observation, θ [rad], and λ [m], the wavelength. It is presented in Equation (2-21).

$$|K| = \frac{4\pi}{\lambda}\sin\left(\frac{\theta}{2}\right) \tag{2-21}$$

Equation (2-22) calculates v_o [m/s], which is a thermal velocity where m [kg] is the mass of the scatterer.

$$v_o = \sqrt{\frac{k_bT}{m}} \tag{2-22}$$

A second input parameter is referred to as *etalam* [kg]. It is the ratio of shear viscosity to thermal conductivity, k [W/m-K], as presented in Equation (2-23).

$$etalam = \frac{\eta}{k}k_b \tag{2-23}$$

The final input is referred to as *etazet*, and it is the ratio of shear viscosity to bulk viscosity. For a monatomic gas the bulk viscosity is zero. For diatomic gases the value must be found in other references or estimated. Equation (2-24) calculates the frequency, ν [Hz], from the x values output by the code in x-units [5].

$$\nu = \frac{xKv_o\sqrt{2}}{2\pi} \tag{2-24}$$

2.4 Selection of scatterer

The equations in sections 2.3.2 and 2.3.3 explain the line shapes in Figure 2-7, which displays the scattering profiles for xenon, argon, and helium. The focus was on noble gases because they are inert and they are of interest in the vortex tube. The S6 model for monatomic gases is also reliable. The scattering amplitude varies with the value of *n*-1, as indicated by Equation (2-17), which is largest for xenon and least for helium. This explains why xenon has the strongest scattering. The breadth of the curves is explained by the use of Equation (2-24) to convert from x-units to frequency; the conversion is inversely proportional to the mass of the molecule. Of the three gases, xenon is the heaviest and helium is the lightest, so helium is spectrally broader due to a higher thermal velocity, which relates back to the Doppler Effect (more colors). Figure 2-7 was important in selecting a gas because the spectral breadth and the intensity have to be balanced such that both can be measured. This combination led to the selection of argon. Although xenon appears to be a better choice because it is much stronger and only slightly narrower, models indicated that in order to achieve results of similar quality to argon using the chosen method (see section 3.9), there would be significant attenuation of the signal (see Chapter 4). Xenon is also very expensive and, based on simulations, the argon results are acceptable.

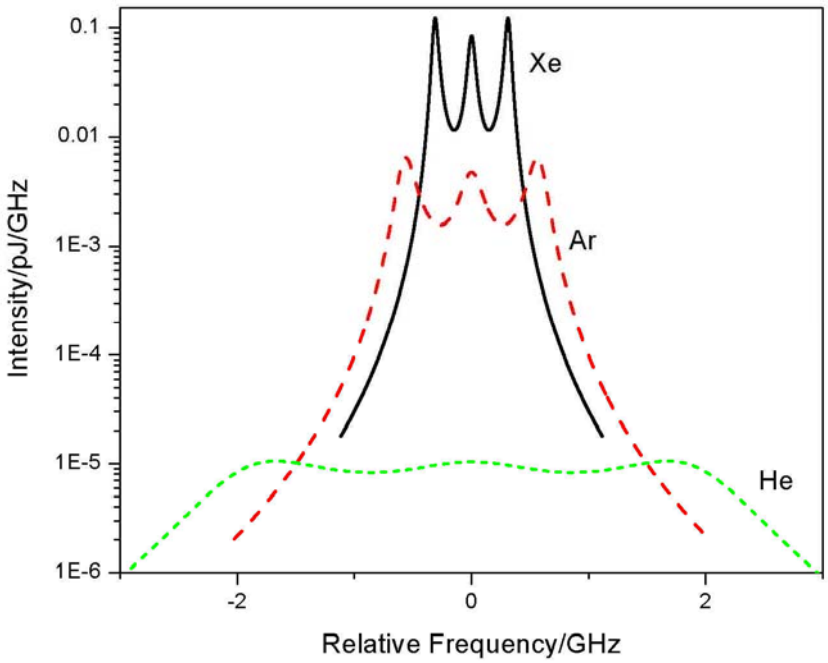

Figure 2-7 Effect of species selection on the Cabannes line. Due to the high mass and index of refraction, the scattering spectrum of xenon at 344.74 kPa is narrow and tall. Due to the low mass and index of refraction, the scattering spectrum of helium is broad and short. All spectra were modeled at a temperature of 300 K and a pressure of 344.74 kPa.

2.5 Historical perspective

This section is a brief discussion of John William Strutt, third Baron Rayleigh (1842 – 1919), after whom "Rayleigh scattering" is named [15]. Strutt studied mathematics and physics at Trinity College in Cambridge. His scientific interests ranged far and wide; in his lifetime he published 446 articles and a book entitled *The Theory of Sound.* In addition to optics he is well known for his work in acoustics as well as his discovery of argon, for which he received the 1904 Nobel Prize in Physics. His optical work began with an interest in photography, which led to the derivation of the resolving power of a grating (see section 3.5) as well as the Rayleigh criterion, which quantifies the minimum distance between two interference fringes for which each fringe can still be resolved. Strutt also developed an equation to describe blackbody radiation at long

wavelengths. Max Planck later derived a relationship for blackbody radiation which reduced to Strutt's equation at long wavelengths and one introduced by Wilhelm Wien at short wavelengths.

In regard to this work Strutt's key achievement was the utilization of scattering to explain the blue sky, presented in an 1871 paper titled *On the Light from the Sky, its Polarization and Colour* [16]. He resolved many of the questions surrounding the origin of the blue sky and used dimensional analysis to prove that the light was not due to reflections from thin plates or bubbles, as had been proposed, but rather due to scattering from particles which were smaller than the wavelength of light. This resulted in the relationship presented in section 2.3.2, which indicates that the intensity of the scattered light is proportional to λ^{-4}.

Chapter 3 Spatially Resolved Measurement Techniques

The Rayleigh scattering spectrum is very difficult to measure because it requires a method with both high spectral resolution and high sensitivity; most measurement techniques sacrifice one of these requirements for the sake of the other. This section discusses some possible measurement techniques, although it is not exhaustive. The first four techniques can be used to measure temperature, pressure and density and the last five techniques measure temperature, pressure, density, and velocity by resolving the Rayleigh scattering spectrum. In the case of scattering measurements and fluorescence, the spatial resolution is determined by the collection optics and the size of the focused laser beam.

3.1 Absorption tomography

Absorption tomography is a technique which can be used to obtain spatially resolved temperature, pressure, and density by measuring absorption across a circular plane. Line-of-sight measurements are obtained at several locations across the cross section. The cross section is then divided into a series of concentric rings. Via mathematical methods the temperature and pressure in each ring can be obtained and this information can be used to infer point values. This method is not well suited to the vortex tube because it suffers from edge effects; the edges of the containment vessel act as lenses, affecting the laser path. In addition, velocity information is unavailable and the point values are inferred from line-of-sight measurements rather than being directly measured.

3.2 Raman scattering

In Chapter 2 Raman scattering was eliminated from consideration due to poor signal strength; however, it is worth further discussion. The Raman spectrum is composed of lines related to rotational and/or vibrational energy states, so it can be used to identify species. As the temperature of the measurement volume changes, so does the Raman spectrum, as indicated in Figure 3-1 and Figure 3-2 [17]. Some lines become stronger and some become weaker, but by measuring the spectral envelope the temperature can be obtained without resolving individual lines. In addition, stray background light can be filtered from the signal because Raman scattering is shifted from the frequency of the incident light. As previously mentioned, however, Raman scattering is extremely weak.

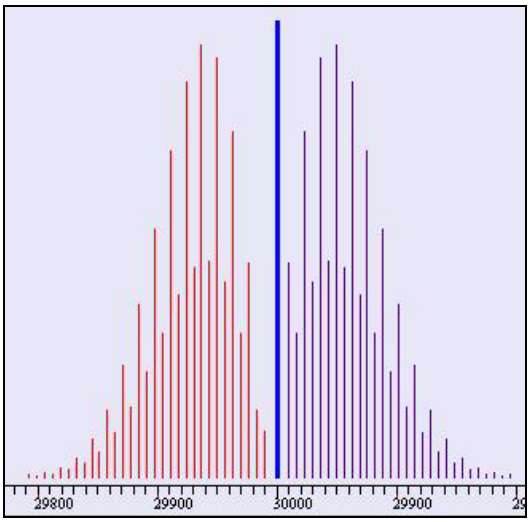

Figure 3-1 Simulation of Raman scattering in diatomic nitrogen at 300 K. The lines on the right are more energetic (anti-Stokes) than the incident light and the lines on the left are less energetic (Stokes).

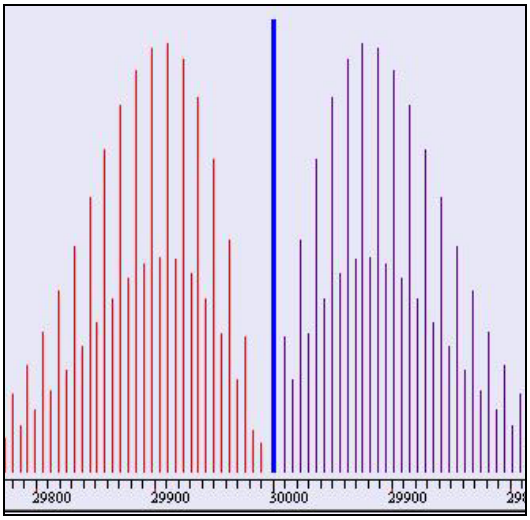

Figure 3-2 Simulation of Raman scattering in diatomic nitrogen at 800 K. Note that some lines increase in amplitude and some decrease as compared to Figure 3-1. The lines on the right are more energetic (anti-Stokes) than the incident light and the lines on the left are less energetic (Stokes).

3.3 Formaldehyde fluorescence

The process of fluorescence begins by seeding the flow with a molecule such as formaldehyde. Fluorescence accompanies absorption; the laser light is absorbed by the tracer and then emitted some time later. The emitted light is not necessarily at the same frequency as the incident light, as is the case in Figure 3-3.

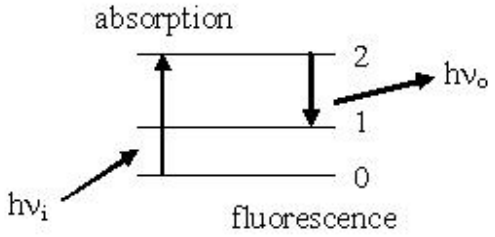

Figure 3-3 Fluorescence accompanies absorption. Some time after a photon is absorbed another photon is emitted. It may not have the same energy as the incident photon.

Measurements are generally recorded at 90° to the direction of beam propagation. Fluorescence is essentially high power Raman scattering. The frequency of the

fluoresced light is generally shifted from the primary light, so background scattering can be eliminated. The signal is roughly eight orders of magnitude stronger than Raman scattering and it too measures the rotational/vibrational spectrum. However, fluorescence requires a tracer and that tracer is what is measured, so fluorescence could not be used to identify species in the measurement volume. Sometimes it is possible for the tracer itself to be a natural part of the system. The tracer may also be toxic, as in the case of formaldehyde [12, 18].

3.4 Two-photon xenon absorption

This is another absorption based method which results in a spatially resolved measurement. The concept is simple. Xenon has an absorption line at 128 nm, but this frequency is difficult to work with. However, this transition can be accomplished by introducing a photon at 256 nm, exciting the xenon to a virtual state, and introducing a second photon at 256 nm to complete the transition, as shown in Figure 3-4.

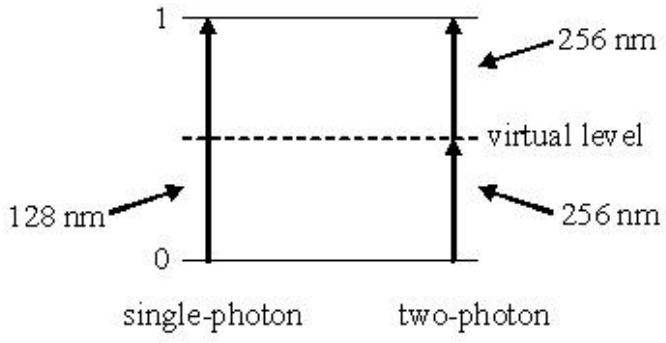

Figure 3-4 Xenon has an absorption transition at 128 nm, but the same transition can be completed using two photons at a frequency of 256 nm. The first photon excites the atom to a virtual energy level and the second photon completes the transition.

In the case of xenon a laser at 256 nm is focused at a point in the measurement volume. Only at this point is there a significant probability that two photons of 256 nm

will be absorbed and complete the transition. The result is a measurement of absorption only at that location. The intensity of the absorption is a function of the number density, so by measuring pressure with a different technique (such as a pressure transducer) the temperature at the point can be calculated from the ideal gas law [18, 19].

The remaining sections discuss techniques which can be used to resolve the Rayleigh scattering spectrum.

3.5 Grating spectrometer

A grating is a grooved plate which is used to spatially separate light. Light is reflected from the grooves in a direction based on the angle of incidence, the wavelength, and the spacing of the grooves. The light interferes, creating an intensity distribution with peaks due to constructive interference and troughs (no signal) due to destructive interference. The peaks occur at phase shifts of $2m\pi$ [rad], where m is any integer and is defined as the order of interference. The resolving power, stated in Equation (3-1), is equal to the order, m, times the number of illuminated grooves, N; the higher the order the higher the resolution.

$$\frac{\lambda}{\Delta\lambda} = mN \tag{3-1}$$

λ [m] is the wavelength and $\Delta\lambda$ [m] is the resolution. In order to resolve the Rayleigh scattering spectrum the best option is to use an echelle grating. The grooves of the echelle grating are right angle steps in which the light is incident upon the shorter edge. Therefore, the light is incident at a high angle, i.e. it is incident at an angle which is large with respect to the grating normal. The groove spacing, d, is also much larger than the

wavelength of light, which results in higher orders and therefore higher resolution. Equation (3-2) relates d [m], m, λ, the angle of incidence (with respect to the grating normal), α [rad], and the angle of reflectance, β [rad]. The plus sign is used when α and β are on the same side of the grating normal.

$$d(\sin\alpha \pm \sin\beta) = m\lambda \tag{3-2}$$

Another important parameter is the blaze angle, which is the angle between the grating normal and the groove normal. The optimum blaze angle is the difference between α and β divided by two. In a Littrow grating α and β are equal, resulting in the most efficient grating [18].

Calculations were made to determine the feasibility of using a grating to resolve the Rayleigh scattering spectrum, neglecting the fact that due to the nature of scattering the light will be incident on the grating at a variety of angles. If the angle of incidence is 79° (blaze angle is 78°), the angle of reflectance is 78.85°, and there are 0.013 grooves/mm, the order of the grating is 192450; this results in the ability to measure a Rayleigh scattering spectrum with a full width at half maximum (FWHM) of 0.067 cm^{-1}. However, the angular separation of the reddest and bluest colors will only be 0.003°; this is the reason why the output of a grating is often input into a prism to further spatially separate the colors. Assuming that 100 points are measured from the grating spectrum (i.e. one data point per 0.00003°) the grating size needs to be approximately 1.7 m. Based on these calculations it is possible to use a grating to resolve the Rayleigh scattering spectrum. The difficulties include obtaining a large grating, measuring wavelengths that are spatially only 0.00003° apart and coping with the variation in the

angle of incidence due to the characteristics of scattering. The advantage of this method is that the entire signal can be measured at one time.

3.6 Density gradient prism

A prism is another device which spatially separates light. Traditionally it is a crystal which refracts different wavelengths of light by different amounts, leading to a spatially resolved spectrum. This traditional prism does not have the resolution required to measure the Rayleigh scattering spectrum, but a different type of prism has been developed. It is a density gradient prism, created by introducing a density gradient into a cell containing rubidium vapor [20]. The density gradient is created by maintaining the upper surface of the cell at a higher temperature than the lower surface. As discussed in Chapter 4, regarding the atomic vapor cell, as the density of a substance changes so does the index of refraction, therefore, light passing through the gradient experiences a spatial deviation. The advantage of this prism over a grating is that the dispersion is only slightly a function of color and within 1 nm of the rubidium absorption line center the dispersive power of the prism exceeds that of a grating. This prism is particularly useful in Raman scattering because it creates dispersion across a wide band of wavelengths and, if the laser light is tuned properly, it simultaneously filters Rayleigh scattering. Based on the results of the experiment performed by Tang, et al., in order to resolve the narrow Rayleigh scattering spectrum the laser would have to be tuned very near the rubidium absorption line and the attenuation may be too severe to obtain any measurements.

3.7 Interferometer/Etalon

A Fabry-Perot interferometer is a device composed of two reflective parallel plates. Light is input into the device through one plate and is reflected back and forth between the two plates, with some light transmitting through the plates with each pass. The light interferes with itself due to the phase shifts introduced by the different path lengths traveled through the interferometer. The output of the device is a ringed interference fringe pattern. If the input light is collimated then several measurements must be taken, varying the spacing between the two plates, in order to obtain temporal separation of the colors of the light. If the input light is diverging then a single measurement can be made which creates spatial separation of the colors of light. An etalon is a special type of interferometer in which the parallelism of the plates is not adjusted by moving one of the plates; it is instead adjusted by screwing down on a spacer [4]. An etalon may be a solid crystal or the space between the two plates can be filled with a gas. One characteristic of the etalon is the free spectral range (FSR), which is defined by Equation (3-3) and shown in Figure 3-5.

$$FSR = \frac{c}{2nd} \tag{3-3}$$

FSR has units of [Hz], *c* [m/s] is the speed of light, *n* is the index of refraction, and *d* [m] is the separation between the two plates of the etalon. FSR is a measure of the maximum wavelength separation that can be measured without overlap. For example, if the spectrum to be measured is wider than the FSR, each measurement will consist of multiple peaks corresponding to the maximum transmission of the instrument function.

If the FSR is wider than the spectrum, there will be only one peak per measurement. Figure 3-5 is an image of the instrument function of an etalon.

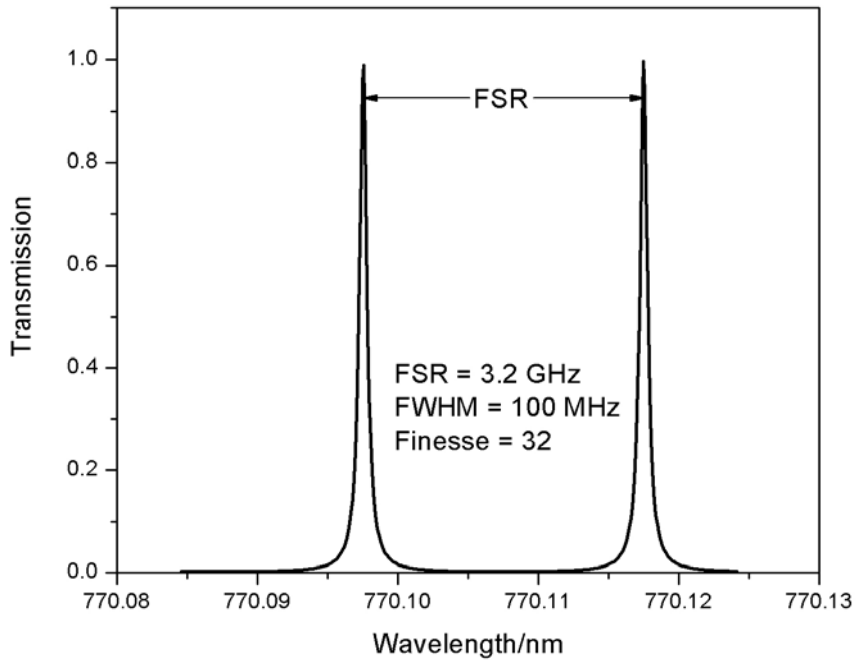

Figure 3-5 Instrument function of an etalon with a FSR of 3.2 GHz, a FWHM of 100 MHz, and a finesse of 32. If a 3 GHz Rayleigh scattering spectrum was measured with this instrument 30 data points would result.

The finesse is a measure of the instrument resolution. Higher resolution requires higher finesse and therefore higher reflectivity. In Equation (3-4) the finesse, F, is defined by the reflectivity, R, of the etalon surfaces.

$$F = finesse = \frac{\pi\sqrt{R}}{1-R} \tag{3-4}$$

The FWHM of the instrument function, as shown in Figure 3-5, is defined as the ratio of the FSR to the finesse. Higher resolution can be achieved by minimizing the FWHM by minimizing the FSR and maximizing finesse. In order to increase the finesse the reflectivity must increase, which can be an expensive and difficult process. In decreasing

the FSR care must be taken to ensure that it will still be larger than the spectrum to be measured. FSR can be decreased by increasing the index of refraction and/or the separation of the plates. The index of refraction can be changed if the etalon is filled with a gas which can be pressurized. The problem with changing the index of refraction or increasing the separation is that the parallelism of the plates will be more difficult to maintain, leading to lower than expected performance and increased production costs.

The transmission of an etalon, assuming that there is no absorption in the etalon material, is defined in Equation (3-5). T is the transmission, δ [rad] is the phase shift, θ [rad] is the etalon internal angle of incidence and λ [m] is the wavelength [21].

$$T = \frac{1}{1 + \frac{4R}{(1-R)^2}\sin^2\left(\frac{\delta}{2}\right)} \tag{3-5}$$

$$\delta = \frac{4\pi}{\lambda} nd\cos\theta \tag{3-6}$$

Equation (3-5) was used to produce Figure 3-5. For a FSR of 3.2 GHz, a finesse of 32, a FWHM of 100 MHz, and a Rayleigh scattering spectrum FWHM of 2 GHz, the resulting etalon would have to be 4.69 cm long and would result in an angular separation of 0.225° between the 121762nd and 121763rd fringes. This results in an etalon diameter of about 0.7 m. The problem with this design is that the resolution is probably insufficient and it would be difficult to make this size cell to specification.

The Rayleigh scattering spectrum has been measured using an etalon in order to obtain velocity and temperature [22, 23]. In the work of Seasholtz, et al., the Rayleigh scattering from a jet of compressed air exiting a nozzle is measured and from these measurements velocity and temperature are determined. They also use traditional means

to measure velocity and temperature for comparison. They found that the velocity measurements are very good, but the temperature measurements are questionable. It is quite possible that the resolution of the etalon was insufficient to fully resolve the shape of the spectrum, which is used to calculate temperature, while the location of the central peak of the spectrum, which is used to calculate the velocity, was measured with sufficient resolution. The other difficulty addressed by these experiments was the sensitivity of the etalon to vibrations and temperature. In one case the etalon was housed in a room away from the experiment; the scattered light was transmitted to the etalon via a fiber.

An alternative method which utilizes an etalon is coherent Rayleigh-Brillouin scattering (CRBS) [24]. In this technique a single pump laser is split into two pump beams which are crossed nearly collinearly at their foci in a measurement volume. A grating like interference pattern results from the interaction due to density perturbations. A second laser is used to probe the volume and create a Rayleigh scattering spectrum. This spectrum is different from the usual scattering pattern in that it is a collimated beam. This collimated, scattered beam is input into a Fabry-Perot etalon with adjustable spacing. In order to scan the spectrum, the spacing of the etalon can be changed (it would be used like an interferometer) or the probe beam can be scanned in color. The latter option tends to be preferred because a scanning probe laser is fairly easy to obtain. By creating a beam of scattered light, this method side steps the issue of low intensity scattering. It also addresses concerns regarding the angle of incidence of the light in the etalon. Like the grating, the etalon function depends on the angle of incidence of the light, which is variable in scattering. However, in this experiment the light is collimated,

so the concern over how the angle of the incident light will affect the performance of the etalon and the accuracy of the measurement is removed.

3.8 Extremely thin cell

The prior methods rely on temporal or spatial separation to measure the Rayleigh scattering spectrum, but this method relies simply on a very narrow line width filter similar to the notch filter system previously described. The scattered light passes through the filter and the laser producing the scattering is scanned in color. The scattering is measured with a detector and an oscilloscope. When the color is tuned away from the frequency of the filter the total power of the scattering spectrum is measured; the spectrum is not resolved. As the laser is scanned to the frequency of the filter the spectrum is slowly measured. At the portion of the scattering spectrum near the filter frequency light is removed from the output, resulting in a dip on the oscilloscope. After scanning the entire spectrum the resulting output through the filter is the Rayleigh scattering spectrum, as shown in Figure 3-6. In order to obtain the necessary resolution, the filter must have a line width which is substantially smaller than the width of the scattering spectrum. One potential problem with this method is dynamic range. If the amplitude of the unfiltered light is much stronger than that of the absorbed light, then the measurement resolution will be poor. In order to illustrate this problem the analogy of "the captain and the boat" is used; a poor method for determining the weight of the captain is to first measure the weight of the boat, then measure the weight of the boat plus the captain, and subtract the difference. The boat weighs much more than the captain, so the weight of the captain will not be accurately determined.

An extremely thin vapor cell (ETC) is a cylindrical glass cell which contains an atomic vapor and can be used as a very narrow line width filter. The dimension of the cell in the direction of laser propagation is small in comparison to the diameter of the light passing through it. This dimension is also small with respect to the mean free path of the gas; many of the gas particles therefore collide with the walls of the cell, thereby preventing those particles from interacting with the laser. The result of this design is that molecules traveling along the direction of propagation experience less interaction with the light than particles which travel perpendicular to the direction of propagation, or parallel to the cell face. The final outcome is that the output of the cell is most affected by particles which travel slowly parallel to the face of the cell and therefore experience no Doppler shift with respect to the light source. The resulting absorption spectrum of the vapor in the cell has a sub-Doppler line width, assuming pressure broadening is negligible. By tuning the laser color this cell would be used as a narrow line width filter in order to measure the Rayleigh scattering spectrum.

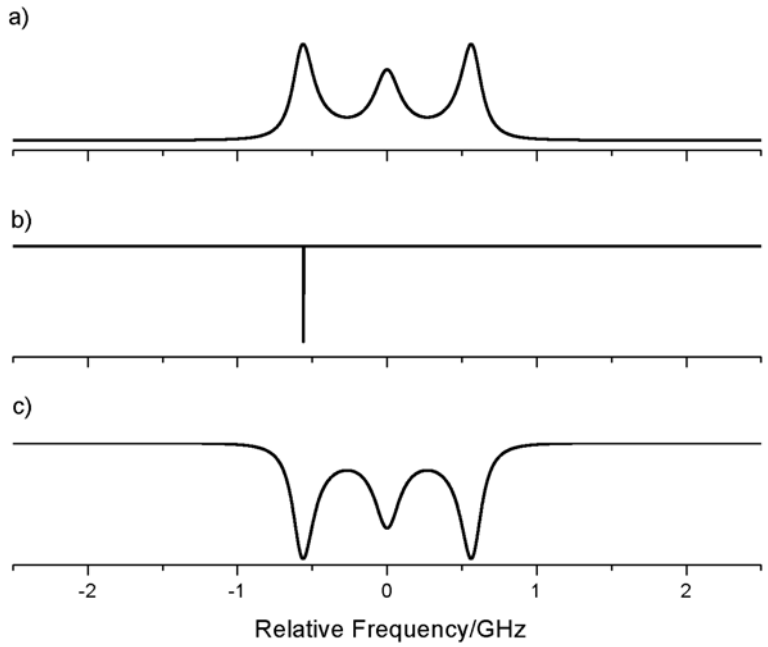

Figure 3-6 Illustration of the use of an extremely thin cell as a filter. a) Rayleigh scattering spectrum as it looks entering the cell. b) One data point of the Rayleigh scattering spectrum as measured using the cell as a filter. c) The final spectrum as measured by the cell.

ETC's have been made and tested [25, 26]. One experiment performed by Sarkisyan, et al., used cesium as the fill gas and in the resulting absorption spectrum of the cell hyperfine lines were resolved. In a standard cesium cell when the D2 absorption line is measured two lines are resolved despite the presence of six hyperfine lines (see section 4.2). In the referenced experiment using an ETC with a nominal thickness of 300 nm all of the hyperfine lines are visible. Cesium under the experimental conditions has a Doppler width of 400 MHz and the hyperfine lines have a width of 40 – 45 MHz. Based on the figures presented in the paper the hyperfine lines are not fully resolved, but the technique is promising. In using an ETC a few simple precautions must be followed. First, the direction of propagation needs to be normal to the cell face otherwise a Doppler shift may be introduced. This could be a problem in measuring the Rayleigh scattering

spectrum because the light is un-collimated. Second, the ETC must be operated at a temperature where pressure broadening will be negligible otherwise the absorption line will be broadened and the resolution will suffer. This may mean that several ETC's must be used in series in order to create enough absorption to avoid the captain and the boat problem.

There are several reasons why this method is not used in this research. First, and perhaps most important, the cells are not currently commercially available. Second, at this point the line width of the filter is unknown. In order to resolve the Rayleigh scattering spectrum a line width of less than 100 MHz will be needed and this may not be possible at this stage of development. This method also becomes mathematically difficult if the vapor in the ETC has hyperfine lines which are spaced closer together than the width of the spectrum; a de-convolution would become necessary in order to extract the spectrum.

3.9 Atomic vapor cell spectrometer

This method is used in this research to temporally stretch the Rayleigh scattering spectrum with a potassium atomic vapor cell (AVC); Chapter 4 describes the AVC in much more detail. This method uses the dramatic change in the index of refraction near a strong absorption line to create a scan of the Rayleigh scattering spectrum. The speed of light in a substance is dependent on the index of refraction, so when the index of refraction is changing quickly with color so is the speed of light. This results in a scan of colors that is referred to as a wavelength-agile scan. The temporal delay introduced into the propagation of the spectrum by passage through the potassium vapor is accompanied

by attenuation. Each color is delayed and attenuated by a different amount, so data reduction must be performed in order to recover the Rayleigh scattering spectrum.

The variation of properties with color is one disadvantage of this method because it requires more data reduction in order to obtain temperature, pressure, density, and velocity. In order to obtain the required time delay the cell was large and a multi-pass system was used, which complicated the optical elements involved. One advantage of this method is that the performance of the AVC is independent of the angle of incidence of the light, unlike in the case of a grating or etalon. In addition, the amount of delay and attenuation can easily be changed by varying the temperature and/or length of the AVC. The AVC is also more forgiving of an adverse environment than an etalon. The etalon is affected by temperature, vibrations and slight variations in alignment but the AVC is not. The location of the potassium absorption line does not vary due to outside influences and the alignment of the multi-pass cell is robust.

3.10 Summary

Nine methods for obtaining temperature, pressure, and velocity have been presented. Absorption and fluorescence were eliminated because it is difficult to obtain velocity measurements using these methods. Raman scattering was rejected because it is very weak. Of the remaining methods several observations can be made. First, size is a major issue. In order to achieve the desired resolution both the grating and the etalon need to be large. In the case of the etalon, this will make manufacturing difficult because maintaining parallelism between two large plates is difficult. The grating, etalon, and the atomic vapor prism are all angle dependent, whereas the AVC is not. The angular

dispersion of those three methods is also fairly small, requiring propagation through a large distance in order to sufficiently separate the colors. The etalon has better resolution and transmission than a grating or a prism, but it is sensitive to environmental conditions. The extremely thin cell is commercially unavailable and the best resolution it can achieve is unknown.

The cost of the equipment is also an issue. The AVC is inexpensive. The setup is theoretically simple and versatile. For example, if an error is made in pretest calculations and the length of the cell needs to be longer or shorter in order to obtain the desired delay with acceptable attenuation, then changing the temperature will change the properties. The cell is readily available from sources such as Thorlabs and Triad Technologies in custom sizes for under $2000. This method also requires only one laser. Standard etalons are expensive and one of the required size would be extremely expensive. The same is true for an unusually large grating. The atomic vapor prism is a possibility, but it is uncertain that the dispersion for the narrow Rayleigh scattering spectrum would be any better than that produced by an etalon or grating; although if it was on a similar scale this method is probably less expensive and more compact. Coherent Rayleigh-Brillouin scattering would probably work but it is potentially more expensive because it requires two lasers. It also may be more difficult to use in something like a vortex tube because the beams need to be nearly collinear. The conclusion is that although the AVC method was difficult, the potential for it to be simple once it was better understood made it worth pursuing.

Table 3-1 Summary of the advantages and disadvantages of the possible measurement methods

Spatially Resolved Techniques – Pressure, Temperature, Density			
Method	Utilizes	Disadvantages	Advantages
Absorption Tomography	Absorption	• Edge effects • Indirect point measurement	• Absorption can be strong
Raman Scattering	Scattering	• Very weak	• Identify species • Do not need to resolve individual lines
Formaldehyde Fluorescence	Fluorescence	• Requires a tracer	• High power Raman
Two-photon Xenon Absorption	Absorption	• Measure pressure using a secondary method	• No quantum mechanics, fairly simple concept
Resolved Rayleigh Scattering Techniques – Pressure, Temperature, Density, Velocity			
Method	Utilizes	Disadvantages	Advantages
Grating Spectrometer	Spatial separation	• Large • Angle dependent • Small angular dispersion • Expensive	• All data recorded at once
Density Gradient Prism	Spatial separation	• Unknown resolution • Angle dependent • Small angular dispersion	• Conceptually simple
Interferometer/Etalon	Spatial or temporal separation	• Expensive • Sensitive to environment • Angle dependent • Already being used	• Previously used/reference literature exists
Extremely Thin Cell	Temporal separation	• Commercially unavailable • Unknown properties	• Simple conceptually • Simple setup
Atomic Vapor Cell Spectrometer	Temporal separation	• Large • Can alter spectrum (distortion) • Properties are difficult to model	• Inexpensive • Independent of angle • Easy to change properties • Has not been tried

Chapter 4 Atomic Vapor Cell

An AVC is a cell with windows that contains a specified substance. In this research potassium was placed inside an evacuated cell. As the temperature of the cell was increased some potassium vaporized, thereby increasing the vapor pressure. This AVC was used to produce a wavelength-agile source. A wavelength-agile source rapidly scans through a broad range of wavelengths; the scans can be used, for example, to measure absorption features from which temperature and pressure can be obtained by comparing the results to previously measured or simulated data. A common method of producing a wavelength-agile laser is to inject a spectrally broadband pulse into a long optical fiber. The index of refraction depends on wavelength and velocity depends on the index of refraction, therefore different wavelengths travel through the fiber at different speeds. If red travels faster than blue in the fiber, then the output is a wavelength scan from red to blue. The literature contains many examples of wavelength-agile sources [27-34].

An AVC can be used in place of the long fiber to create a wavelength-agile laser, but there are several differences. Near an atomic absorption line the index of refraction drastically changes with small changes in color, thereby creating a wavelength scan over a narrow range of frequencies. The resulting wavelength scan can be used to create higher resolution measurements than is achievable with a fiber, although over a much narrower wavelength range. The advantage of an AVC is that it can be used at any wavelength at which a strong absorption line can be found. The ability to make high resolution measurements is the reason for using an AVC to measure the Rayleigh

scattering spectrum. However, because the attenuation and delay vary with wavelength the spectrum is distorted; the three peaks of the spectrum are delayed and attenuated by different amounts, which must be factored into the analysis.

Atomic vapor cells have been used previously for similar purposes. Yalin, et al. use a mercury vapor cell to measure the laser seeding efficiency of a Ti:Sapphire laser [35]. The seeded portion of the laser is narrow-band and therefore, when it is tuned near a mercury absorption line, the group velocity dispersion (GVD) is large. The GVD is a measure of the variation in the speed of light with color. The unseeded portion of the laser is broadband and therefore very little of that light is affected by the absorption line. Kash, et al. use a hot rubidium atomic vapor cell to slow the speed of light to 90m/s [36]. Phillips, et al. essentially stop light, storing it in rubidium vapor until choosing to release it [37]. Atomic vapor cells have also been used for spatial, rather than temporal, dispersion. For example, as described in section 3.6, Tang, et al. create a prism from a rubidium vapor cell with a density gradient and use it as a Raman spectrometer [20].

4.1 Description of AVC

Figure 4-1 shows the theoretical absorbance, scan rate, and excess delay for a 22.4 m long potassium AVC maintained at a temperature of 362 K. In part (b) of this figure it appears that the excess delay, i.e. the extra time required for the light to pass through the potassium rather than a vacuum, can have negative values. Negative values of excess delay mean that the light exits the cell before it enters the cell; it is traveling faster than the speed of light. This would seem to be a violation of the special theory of relativity,

but it is not. An explanation will be presented after some additional variables are introduced.

All of the values in Figure 4-1 were derived from the electric susceptibility. The electric susceptibility, χ, is related to the complex index of refraction by Equation (4-1), where $\tilde{n}$ is the complex index of refraction; both variables are functions of frequency, ω [38].

$$\tilde{n}(\omega) = \sqrt{1 + \chi(\omega)} \tag{4-1}$$

Demtröder presents the electric susceptibility in two equations, one for a Lorentzian dominated feature and one for a Gaussian dominated feature [18]. The convolution of these two equations is the electric susceptibility for this research, with the Lorentzian features dominating in the wings of the curves. The electric susceptibility was calculated for all eight of the hyperfine split lines of the potassium D1 line and the summation of these values resulted in the composite line in Figure 4-1. More information about hyperfine splitting can be found in section 4.2 and Appendix E.

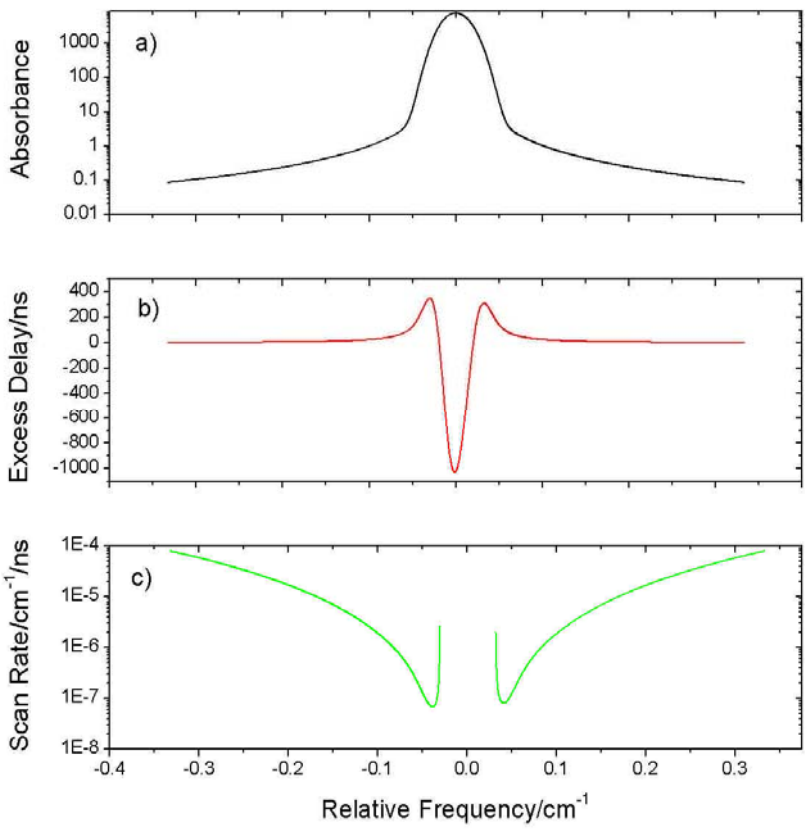

Figure 4-1 Properties of potassium AVC at 362 K. a) Absorption line. Close inspection reveals it is asymmetric. b) Excess delay curve. c) Scan rate, which is the inverse of the derivative of excess delay with respect to color.

The electric susceptibility is calculated in Equation (4-2), where f is the oscillator strength of each hyperfine line, c [m/s] is the vacuum speed of light, N [m^{-3}] is the number density, q [C] is the charge of an electron, v_p [m/s] is the most probable speed of atoms in the AVC, ε_o [C^2/N-m^2] is the permittivity of free space, m_e [kg] is the mass of an electron, ω_o [rad/s] is the potassium line center, ω_a [rad/s] is a variable of integration, ω [rad/s] is the local frequency, and γ [rad/s] is the Lorentzian FWHM.

$$\frac{1}{2}\chi = \frac{f \cdot c \cdot N \cdot q^2}{2 \cdot \sqrt{\pi} \cdot v_p \cdot \varepsilon_o \cdot m_e \cdot \omega_o} \cdot \int \left[\left(\frac{1}{\omega_a^2 - \omega^2 + i \cdot \gamma \cdot \omega} \right) \cdot \exp\left(- \left[c \cdot \frac{\omega_a - \omega_o}{\omega_o \cdot v_p} \right] \right)^2 \right] d\omega_a \quad (4\text{-}2)$$

The most probable speed is calculated in Equation (4-3) from Boltzmann's constant, k_b [J/K], the temperature of the potassium, T [K], and the mass of the potassium, m [kg].

$$v_p = \sqrt{2 \cdot k_b \cdot \frac{T}{m}} \quad (4\text{-}3)$$

In Equation (4-4) the index of refraction, n, is calculated from the real portion of the electric susceptibility and in Equation (4-5) the extinction coefficient, κ, is calculated from the imaginary portion.

$$n = \frac{1}{2} real(\chi) + 1 \quad (4\text{-}4)$$

$$\kappa = -\frac{1}{2} imag(\chi) \quad (4\text{-}5)$$

These values can also be related by the Kramers-Kronig relation represented by Equations (4-6), (4-7), and (4-8). Here Δn is the total height of the index of refraction data and κ_{max} is the maximum extinction coefficient.

$$\kappa \approx \kappa_{\max} \left(\frac{\gamma}{2} \right)^2 \left[(\omega_0 - \omega)^2 + \left(\frac{\gamma}{2} \right)^2 \right]^{-1} \quad (4\text{-}6)$$

$$n - 1 \approx \Delta n \left(\frac{\gamma}{2} \right) (\omega_0 - \omega) \left[(\omega_0 - \omega)^2 + \left(\frac{\gamma}{2} \right)^2 \right]^{-1} \quad (4\text{-}7)$$

$$\Delta n = \kappa_{\max} \quad (4\text{-}8)$$

In Equation (4-9) the group velocity, V_g [m/s], is calculated [35]. The shape of a pulse injected into the AVC is distorted based on the speed with which each individual color

progresses. This distorted pulse has a certain envelope, and the group velocity represents the velocity with which a recognizable portion of that envelope, such as the leading edge, propagates [4]. In Equation (4-10), the excess delay due to potassium atomic vapor, t_{delay} [s], is calculated from the length of the cell, L [m], group velocity, and speed of light. In Equation (4-11) the absorbance, α, is calculated from the extinction coefficient, speed of light, and length of the cell.

$$V_g = \frac{c}{n + \omega \cdot \frac{dn}{d\omega}} \tag{4-9}$$

$$t_{delay} = \frac{L}{V_g} - \frac{L}{c} \tag{4-10}$$

$$\alpha = 2 \cdot \kappa \cdot L \cdot \frac{\omega}{c} \tag{4-11}$$

In Figure 4-1 the absorbance was plotted using Equation (4-11). The excess delay was plotted using Equation (4-10), which is related to frequency via the group velocity presented in Equation (4-9). The scan rate was calculated from the inverse of the derivative of excess delay versus frequency. A small value for the scan rate results in a higher resolution measurement. At this point, the seeming violation of relativity can be explained. The excess delay is based not on the velocity of each color, but on the group velocity of all of the colors. This group velocity can exceed the speed of light in a vacuum, but relativity states that *information* can not be transmitted faster than the speed of light. It has been shown that in the anomalous dispersion that occurs near an absorption line the signal velocity no longer is the same as the group velocity because the signal is distorted. The signal velocity is limited by the speed of light but the group

velocity can be larger. A more complete explanation for the interested reader can be found in the references [4, 39].

Figure 4-2 illustrates the effect of the variable scan rate and attenuation near the potassium absorption line on a pulsed laser spectrum. At the left of the figure a Spectra Physics Ti:Sapphire laser was tuned away from the potassium line, so the result was a measurement of the laser time trace within the limits of the electronic equipment; these data were scaled for the figure. As the laser was tuned closer to the potassium line the intensity decreased while the FWHM increased. The amplitude decrease was due to the increase in attenuation near the potassium absorption line and the decrease in the scan rate. The reduction in the scan rate stretched the pulse in time, and therefore the amplitude decreased consistent with conservation of energy.

The amount of attenuation and delay is affected by the amount of potassium vapor which the light passes through. In this experiment potassium was placed in an evacuated Pyrex cell. The quantity of potassium vapor was varied by adjusting the length and/or vapor pressure of the potassium. The length was adjusted using a multi-pass White-cell and the vapor pressure was adjusted by increasing or decreasing the temperature of the potassium (see section 5.5.1.1).

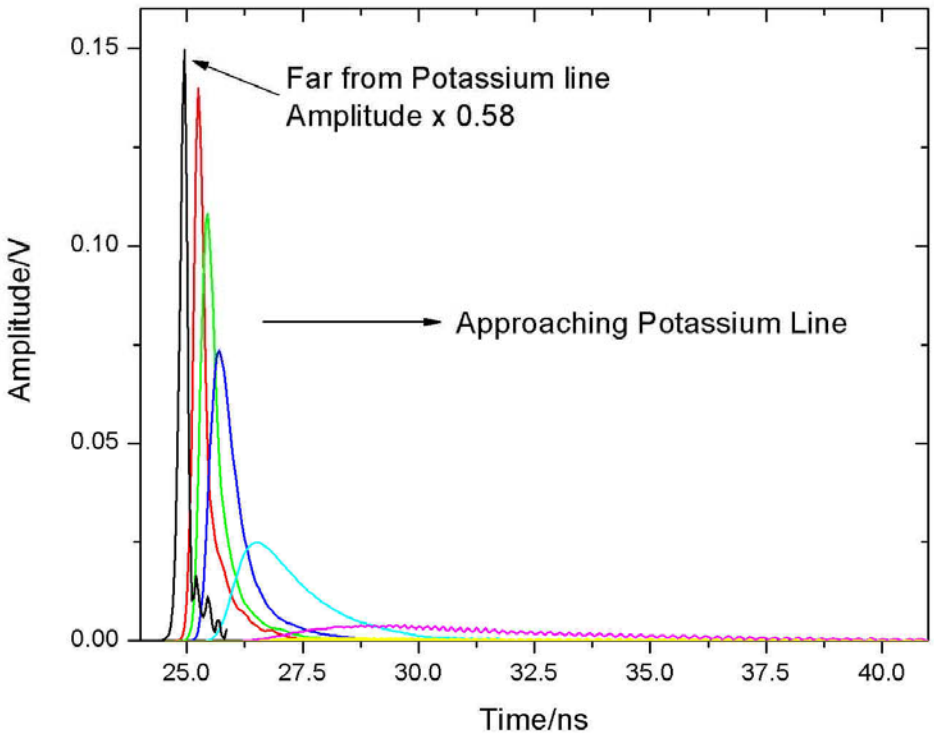

Figure 4-2 Illustration of the effect of the atomic vapor cell on the laser. The curves move further to the right as the laser is tuned closer to the absorption line of the potassium in the atomic vapor cell. The laser spectrum is attenuated and broadened as the absorption line is approached.

4.2 Hyperfine splitting

Many elements, including potassium, exhibit hyperfine splitting (HFS). The cause of hyperfine splitting is described below, but the outcome is that what may appear to be one broad absorption line are actually many narrow hyperfine absorption lines. Usually these lines are too narrow and too close together to be resolved, so they effectively add together to create a "composite" line. In a standard atomic spectral line database or table generally only the composite line is listed. In most cases this is sufficient, but in this experiment the shape of the absorption line determines the wavelength-agile properties of the AVC, therefore hyperfine splitting must be accounted

for. The following equations outline how to calculate the strength and location of the hyperfine lines.

The total angular momentum of an electron in an atom is represented by the letter *J* and has integral or half-integral values. *J* is the summation of the total orbital angular momentum, *L*, and the electron axial angular momentum, *S*. When *L* is greater than or equal to *S* there are $2S+1$ values of *J* and when *S* is greater than *L* there are $2L+2$ values; fine structure results from the multiple values of *J*. The D1 and D2 lines in alkali atoms are examples of fine structure. In these atoms the value of the ground state *J* is 1/2, but two values are possible for the excited state: 1/2, which corresponds to the D1 line, and 3/2, which corresponds to the D2 line. The D2 line is stronger, as indicated by the larger value of angular momentum.

The angular momentum of the nucleus is represented by the letter *I*. The total angular momentum of the atom is represented by the letter *F* and is the summation of *J* (electron) and *I* (nucleus). The interaction between the spinning electrons and the spinning nucleus leads to hyperfine splitting of the fine split energy levels, as seen in Figure 4-3. This results in multiple absorption lines near the frequency of the fine split line. In the case of potassium, with two isotopes, there are eight hyperfine lines which compose the D1 line. These lines are so close together that they appear to be one line located at 12985.17 cm^{-1}. Figure 4-3 also shows the two dominant isotopes of potassium. If only one isotope is present, then only four hyperfine lines compose the D1 line. The isotopes are not centered at the same location because they vary in weight, which affects the interaction between the electrons and nucleus [40].

The location and relative strengths of hyperfine lines can be quantified. The first set of equations describes how to determine the location of each hyperfine line. First, a relative location is calculated based on the energy of the atom. In the case of the D1 and D2 potassium lines, E_J, the initial energy level, is zero [41, 42].

$$E_F = E_J + E_{Dipole} + E_{Quadrupole} \tag{4-12}$$

$$\nu = \frac{E}{h} \tag{4-13}$$

$$E_{Dipole} = \frac{h}{2} A\kappa \tag{4-14}$$

$$E_{Quadrupole} = hB\frac{\frac{3}{2}\kappa(\kappa+1) - 2I(I+1)J(J+1)}{2I(2I-1)2J(2J-1)} \quad I,J \geq 1 \tag{4-15}$$

$$\kappa = F(F+1) - I(I+1) - J(J+1) \tag{4-16}$$

h [Js] is Planck's constant, ν [Hz] is the frequency of the transition, and A and B are constants. For the D1 transition, B is zero. The value of ν is calculated for the ground state and for the excited states. Note in Figure 4-3 that in the case of the D1 line there are only two hyperfine excited levels, but in the case of the D2 line there are four. This difference is due to the larger value of J in the D2 state. F equals $I \pm J$ and $I \pm J$-1 when J is greater than one and $I \pm J$ when J is less than one. Due to selection rules only transitions in which the change in F between energy levels is -1, 0, or +1, are allowed. These equations result in the ν values in the figure such as -288.57 MHz, 173.14 MHz, etc. These values do not provide the absolute location of the hyperfine lines. In order to locate the lines the differences between the levels of the allowed transitions need to be determined. Looking first at ^{39}K only, the transitions from the $4s^2S_{1/2}$ to the $4p^2P^0_{1/2}$ state are calculated in Table 4-1:

Table 4-1 Calculation of transitions of ^{39}K in the D1 line

$4s^2S_{1/2}$	$4p^2P^0_{1/2}$	^{39}K $\Delta\nu$ (MHz)
1	1	-(-288.57)+(-36.063) = 252.51
1	2	-(-288.57)+(21.638) = 310.21
2	1	-(173.14)+(-36.063) = -209.20
2	2	-(173.14)+(21.638) = -151.50

These values are the location of each hyperfine line with respect to the center of gravity of the line, which is measured as 12985.17 cm^{-1}. The first column contains the *F* values for the lower energy state and the second column contains the *F* values for the higher energy state. Table 4-2 shows the calculations for the ^{41}K isotope. This isotope is shifted from the center of gravity of the ^{39}K isotope (and the center of gravity of the line) by 235 MHz.

Table 4-2 Calculation of transitions of ^{41}K in the D1 line

$4s^2S_{1/2}$	$4p^2P^0_{1/2}$	^{41}K $\Delta\nu$ (MHz)
1	1	-(-158.76)+(-19)+235 = 374.76
1	2	-(-158.76)+(11.4)+235 = 405.16
2	1	-(95.255)+(-19)+235 = 120.75
2	2	-(95.255)+(11.4)+235 = 151.15

The absolute line locations are listed in Table 4-3, determined by converting the $\Delta\nu$ values to wavenumber and adding them to the overall line center of gravity.

Table 4-3 Absolute location of hyperfine lines in D1 line

12985.163 cm^{-1}
12985.1649 cm^{-1}
12985.174 cm^{-1}
12985.175 cm^{-1}
12985.1784 cm^{-1}
12985.1803 cm^{-1}
12985.1825 cm^{-1}
12985.1835 cm^{-1}

The relative strengths of the hyperfine lines can be determined in two ways. The computationally simpler method is to use the transition strength diagrams in Appendix D of Metcalf [42]. For potassium the D1 and D2 figures for $I = 3/2$ are used. First, the numbers in the figure for each allowed transition from $F = 1$ to $F = 2$, $F = 1$ to $F = 1$, etc. are summed. In order to obtain a relative strength, the value of each transition is divided by the sum of the values obtained for all transitions. For potassium this results in four values, but the two isotopes have the same I value, so the same four values are used for each isotope, resulting in eight lines. These values are converted to relative strengths by multiplying the four values by the abundance of each isotope. If the I values differed, then calculations would have to be performed for each value.

The second method is more general, but requires more computation. The following equations are used when the value of J is the same for both the ground and excited states.

$$\frac{(F-I+J+1)(F+I-J+1)(I+J+F+2)(I+J-F)}{4(F+1)} \qquad F \text{ to } F+1 \qquad (4\text{-}17)$$

$$\frac{[F(F+1)-I(I+1)+J(J+1)]^2(2F+1)}{4F(F+1)} \qquad F \text{ to } F \qquad (4\text{-}18)$$

$$\frac{(F-I+J)(F+I-J)(I+J+F+1)(I+J+1-F)}{4F} \qquad F \text{ to } F-1 \qquad (4\text{-}19)$$

When the transition is from J to J-1 the following equations are used [43]:

$$\frac{(F+I-J+1)(J+I-F)(F+I-J+2)(J+I-F-1)}{4(F+1)} \qquad F \text{ to } F+1 \qquad (4\text{-}20)$$

$$\frac{(F+J-I)(F+I-J+1)(I+J+1+F)(I+J-F)(2F+1)}{4F(F+1)} \qquad F \text{ to } F \qquad (4\text{-}21)$$

$$\frac{(F+J-I-1)(F+J-I)(I+J+F+1)(I+J+F)}{4F} \qquad F \text{ to } F-1 \qquad (4\text{-}22)$$

In these six equations the variables provided by the reference must be substituted so that J becomes F, S becomes J, and L becomes I; these substitutions have already been made in the equations presented here. When the transition is from J-1 to J, as in the case of the potassium D2 line, the following equations are used [40]:

$$\frac{(J+F+I+1)(J+F+I)(J+F-I)(J+F-I-1)}{F} \qquad F-1 \text{ to } F \qquad (4\text{-}23)$$

$$-\frac{(J+F+I+1)(J+F-I)(J-F+I)(J-F-I-1)(2F+1)}{F(F+1)} \qquad F \text{ to } F \qquad (4\text{-}24)$$

$$\frac{(J-F+I)(J-F+I-1)(J-F-I-1)(J-F-I-2)}{F+1} \qquad F+1 \text{ to } F \qquad (4\text{-}25)$$

Figure 4-3 shows the energy levels of the hyperfine split lines of potassium, indicating the relative strength and location as well as the absolute location of each hyperfine line. The composite line shape is created by first applying the equations in section 4.1 to each line and then adding the lines together. The Matlab code which was used to calculate the hyperfine line locations, relative strengths, and line shapes is located in Appendix E.

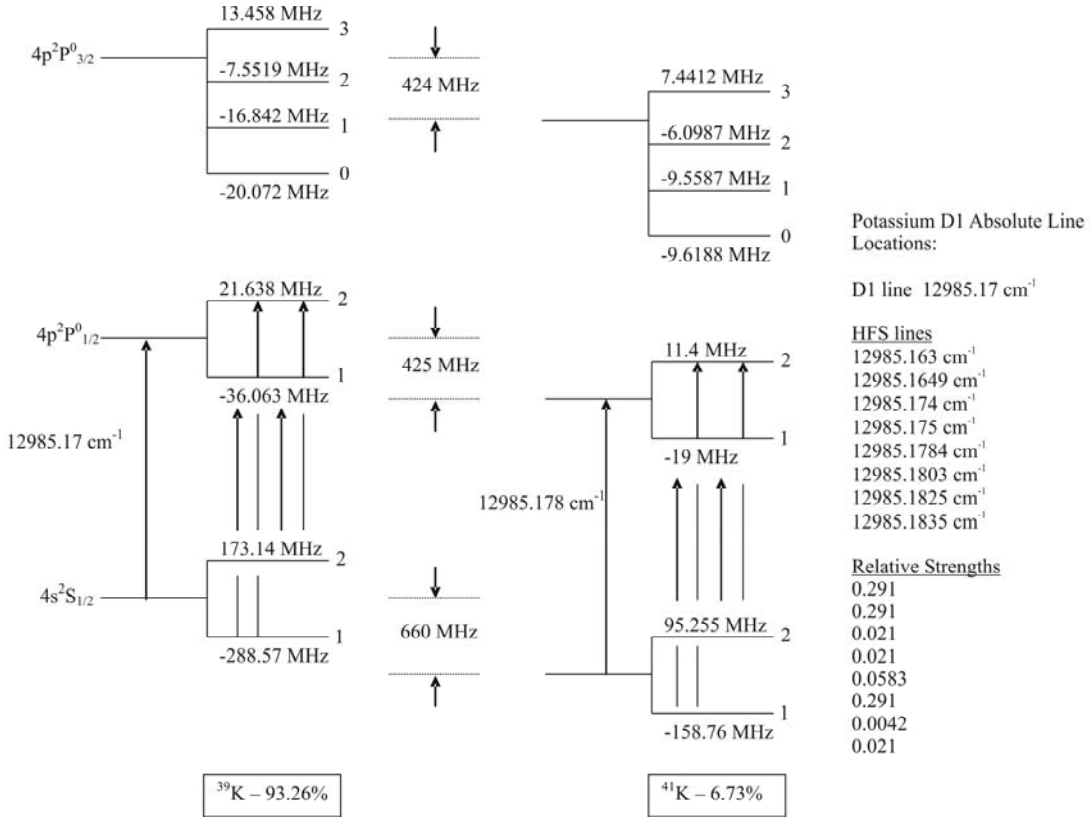

Figure 4-3 Diagram of hyperfine splitting of the potassium D1 line. The D1 fine line is created in the transition from $4s^2S_{1/2}$ to $4p^2P^o_{1/2}$. The D2 fine line is created in the transition from $4s^2S_{1/2}$ to $4p^2P^o_{3/2}$.

Chapter 5 Experimental Setup

The intent of this research was to measure the temperature, pressure, and velocity of the flow in a vortex tube. As the research progressed the development of the measurement technique became difficult, so rather than measuring a vortex tube a proof-of-concept measurement of the Rayleigh scattering in a fiber was completed. The setup for this experiment is described here, but the setup is similar to that which would be used to measure a vortex tube.

The experimental fiber setup is shown in Figure 5-1. A pulsed Ti:Sapphire laser was first attenuated and then focused into a 50 μm core fiber with a total length of 8.795 km. The average laser power was reduced to approximately 30 mW from 2 W in order to avoid damaging the fiber. As the light passed through the fiber some of it was scattered by the fiber and some of this scattered light was directed back out of the fiber. A fiber was selected for the scattering measurement because the scattering signal is stronger than it would be in a gas and the experimental setup was simpler; the system was aligned by shining a visible light source through the fiber. In a future test a vortex tube could replace the fiber as the scattering volume as shown in Figure 5-2. The backscattered light was directed through a polarizer and then into the pulse picker. The multimode fiber used in this experiment led to partial depolarization of the laser and, therefore, the scattered light; one polarization had to be selected in order for the pulse picker to be operational. The pulse picker was set to a 6 μs delay based on the laser pulse. This delay guaranteed that the measured signal was due to scattering deep within the fiber and not reflections from lenses or the fiber face. The signal then passed through the potassium

AVC, which was maintained at 361 K in the center and 370 K at the ends. A White-cell was used to multi-pass the AVC. Upon exiting the White-cell the laser was directed into a photomultiplier tube (PMT), the output of which was connected to a combination amplifier and discriminator. The signal was then sent to an oscilloscope where the histogram function was used to obtain the measurement. This signal was analyzed as described in Chapter 6. The following sections will discuss each of the experimental components in detail.

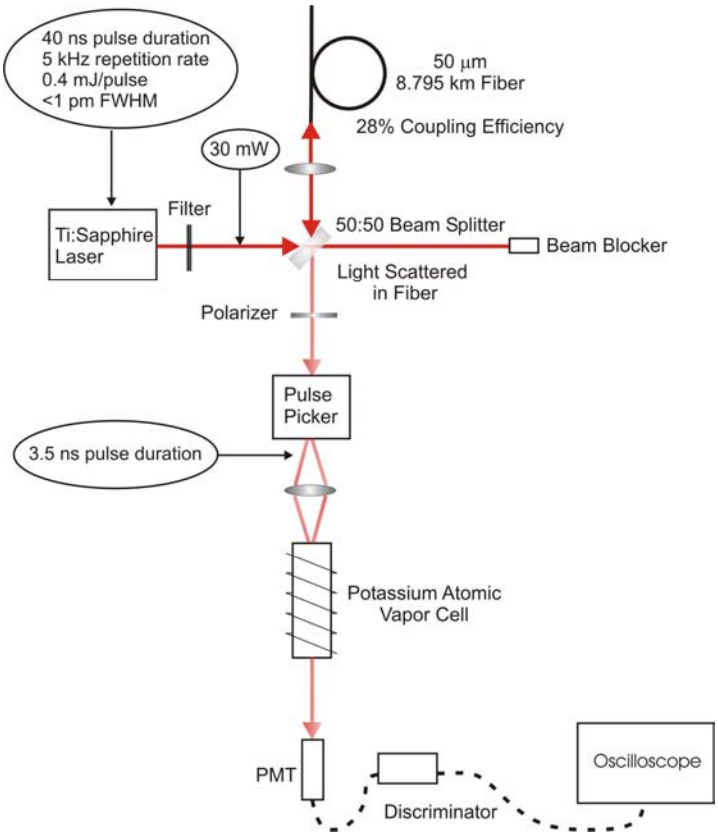

Figure 5-1 Schematic of experimental setup used to measure Rayleigh scattering in a fiber. The Ti:Sapphire laser was focused into a fiber. The scattered light passed through some optical elements and then entered the AVC where it was temporally delayed. A photon counting PMT was used to measure the signal.

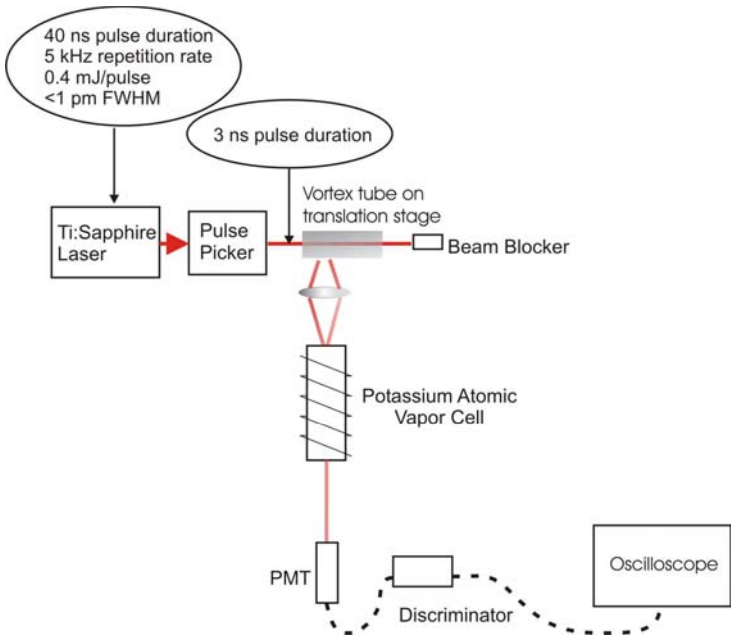

Figure 5-2 Schematic of experimental setup that could be used to measure Rayleigh scattering in a vortex tube.

5.1 Laser

The laser was a Class IV tunable solid state Positive Light (now Coherent) Indigo-Oscillator with an Evolution-15 pump laser. The pump laser contained a Q-switched Nd:$LiYF_4$ laser which emitted light at 1053 nm. This light was doubled in an LBO crystal to 527 nm. The final output was 15 W with energy of 3 mJ/pulse. This light was directed through a Ti:Sapphire crystal. The laser could be operated in the seeded or unseeded modes. In the seeded mode the power output was 2 W and the color could be tuned from 764 nm to 781 nm. In unseeded operation the power was only 1 W and the pulse was spectrally broadened.

Seeding occurred via an external cavity diode laser (6312 New Focus); this laser had a 5 to 10 mW output power with 20 fm wavelength actuation. Seeding is a process by which the Ti:Sapphire laser light is forced to be a certain color. The result is a very spectrally narrow line width laser, in this case less than 1 pm in width at the wavelengths

of operation compared to approximately 4 nm in width for the unseeded laser. This system used a scanning etalon with a free spectral range of 1500 MHz and a resolution of 10 MHz to maintain a time-averaged line width of 27 MHz. The seeding could be maintained manually, but in all experiments it was maintained automatically utilizing the software supplied with the laser. The final laser output was a horizontally polarized pulse with a 40 ± 10 ns duration and a 5 kHz repetition rate.

5.2 Fiber

The alignment procedure using a fiber was simple; a visible light source was directed into one end of the fiber and that strong beam was aligned with the system. Unfortunately there is little in the literature about the spectrum of Rayleigh scattering in a fiber, so the results may be of limited interest. However, as a means of testing the measurement method scattering, from a fiber was very useful. The fiber for this experiment had a 50 μm core, 125 μm cladding, and a numerical aperture of 0.192. The ends were connectorized and angle polished at 8° and the length was 8.795 km. The fiber was mounted at an 11° angle.

5.3 Vortex tube

The vortex tube was not measured in this research, but the measurement technique was developed with the vortex tube in mind, so a general description is in order. More detailed descriptions can be found in the references [1, 44]. A vortex tube is a device that was developed early in the 20th century. A fluid, such as compressed air, is introduced via an inlet port located near one end of the tube. The fluid is forced into a vortex flow via tangential inlet holes. The fluid travels down the tube and some of it

escapes at the far end of the tube. This fluid is hotter than the inlet fluid. The rest of the fluid is "reflected" back to the other end of the tube, where it exits. This fluid is colder than the inlet fluid. The vortex tube is therefore a device with no moving parts which can create hot and cold flows from a single fluid stream. There are several theories regarding how this process takes place, but thus far no experimental measurements have confirmed any of the theories. The reason is that although the inlet and outlet properties can be easily measured, the process which creates the different temperature streams occurs within the vortex tube and that region is difficult to measure. Traditional devices, such as a pitot tube, are invasive and therefore change the flow; the measurement then no longer reflects the behavior of the vortex tube. For this reason this research focused on developing a non-invasive technique which could measure the characteristics of the vortex tube within the tube itself. Due to the difficulty in developing the technique no measurements were completed but it is possible that some may be completed at a future date.

5.4 Pulse picker

In order to measure the Rayleigh scattering spectrum a spectrally narrow laser pulse was required, but a spectrally narrow pulse results in a temporally broad pulse due to the Heisenberg uncertainty principal. The temporal delay introduced by the AVC was not large enough to achieve the desired temporal resolution if a 40 ns laser was used, so a modulator was introduced into the setup in order to reduce the temporal width. After modeling several values of the temporal FWHM, it was determined that 4 ns would yield better temporal resolution without reducing the spectral resolution. The spectral

resolution can be degraded by using a pulse picker because once the pulse passes through the pulse picker it will be spectrally broadened and if it is broadened enough then the convolution of the laser pulse and the Rayleigh scattering spectrum will result in a broadened spectrum. The pulse picker also results in a reduction in power which is proportional to the ratio of the output pulse width to the input pulse width. A Conoptics M360-80 S.E. modulator with an extinction ratio at 770 nm of 8:1 sliced the 40 ns pulse to 3.5 ns. The pulse picker was oriented such that the input and output polarizations were vertical.

5.5 Atomic vapor cell

The AVC in this experiment contained potassium. The windows were set at Brewster's angle (55.7°) resulting in a parallelogram cross section; the length of the cell from the center of one window to the next was 1.4 m. The inside diameter of the cell, which was constructed of Pyrex, was 7.62 cm.

5.5.1 AVC variables

The attenuation and dispersion of the potassium AVC were easily controlled by varying the number density. The number density could be varied by changing the vapor pressure (by varying the temperature) and/or length of the cell. The color of the scattered light relative to the potassium absorption line also determined the amount of dispersion and attenuation. The nearer the two colors were to each other the greater the dispersion, but the attenuation was also greater. Due to hyperfine splitting the absorption line was asymmetric. Increasing temperature increased the number density of potassium, thereby increasing delay and attenuation. A balance was found by varying both temperature and

length. In this experiment it was easier to use a long cell and a low temperature. The low temperature was easier to work with and decreased the likelihood of potassium condensation on the cell windows because convection and radiation were reduced. There was also a decrease in beam steering. It should be noted that no matter how the desired characteristics were achieved, the attenuation and delay varied with frequency; this variation must be accounted for in the data analysis.

5.5.1.1 AVC heater

One method of changing the number density of potassium is to adjust the vapor pressure by adjusting the temperature. In numerous prototypes there were several problems introduced by heating the cell. The first was that in a cell with a large diameter the center of the windows tended to be at the lowest temperature if precautions were not taken. The result was condensation of potassium on the windows, which distorted and blocked the passage of the laser through the cell. A second problem was beam steering. If the cell was much hotter than room temperature then temperature gradients were large, creating density gradients that caused the laser beam to move. In the final heater design the goal was to create an oven in which the temperature of the potassium AVC was constant from end to end, with only one location near the center of the AVC at a slightly lower temperature. This low temperature determined the vapor pressure and therefore number density of the potassium in the cell. In order to avoid irregularities in the amount of delay and attenuation due to variations in number density, this low temperature was maintained at 361 K while the rest of the cell was maintained at 370 K. The heater enclosure was made of a 2180 mm long 101.6 mm square aluminum tube with four 240

W 25.4 mm by 609.6 mm blanket heaters attached to the tube; the heaters were used at about 5 – 10% capacity. The exterior was covered by 38.1 mm thick fiberglass insulation, except for two holes that were left open for the passage of the laser into and out of the cell. The center was cooled by placing a small aluminum rod in contact with the AVC near the center of its length.

5.5.1.2 White-cell

In order to achieve the desired results an AVC that was 22.4 m long was required, but this length is not practical for either construction or for a laboratory, so instead a 1.4 m long base path length cell was purchased. The 22.4 m length was achieved by placing the AVC inside a multi-pass White-cell [45]. The White-cell used a set of three mirrors with the same radius of curvature of 2 m; the mirrors were separated by the radius of curvature. One mirror was 50.8 mm in diameter and the other two mirrors were 25.4 mm in diameter. The smaller mirrors were placed side by side 2 m away from the large mirror such that the radius of curvature of the large mirror was located in between the small mirrors. The light entered and exited the cell, as shown in Figure 5-3, on either side of the 50.8 mm mirror. The beam expanded through the cell until it fell on the 25.4 mm mirror, at which point the light was refocused and directed to the 50.8 mm mirror. The light then fell on the other 25.4 mm mirror and was then refocused onto the large mirror. This process was repeated until the last image fell off the end of the large mirror and exited the cell. If there was 1 image on the large mirror there were 4 passes through the cell, 3 images resulted in 8 passes, 5 images resulted in 12 passes, 7 images resulted in 16 passes, etc. The number of passes was controlled by varying the location that the

image appeared on the large mirror. The alignment of the system was forgiving and the losses were limited to the efficiency of the mirrors, and in this case, the efficiency of the Brewster angle windows on the potassium cell.

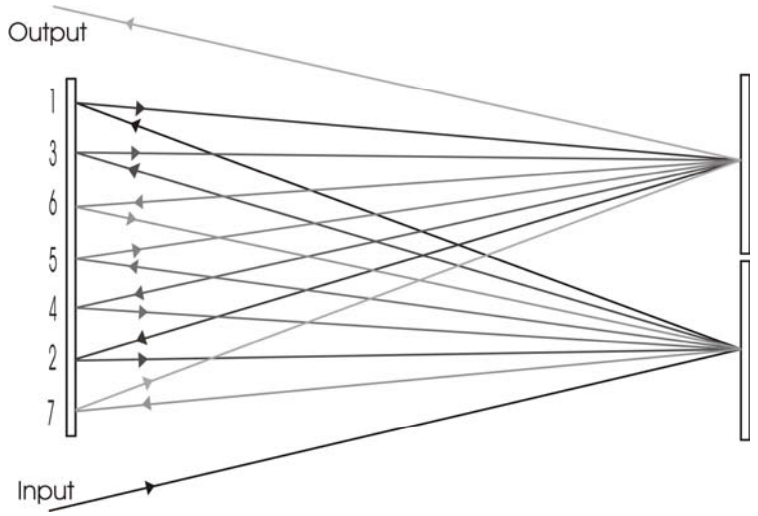

Figure 5-3 Illustration of a 16 pass White-cell.

Figure 5-4 is an illustration of the AVC heater assembly. Note that the White-cell mirrors were placed inside the heater and a portion of the heater could be removed in order to access the mirrors. The insulation which surrounded the final assembly is not shown.

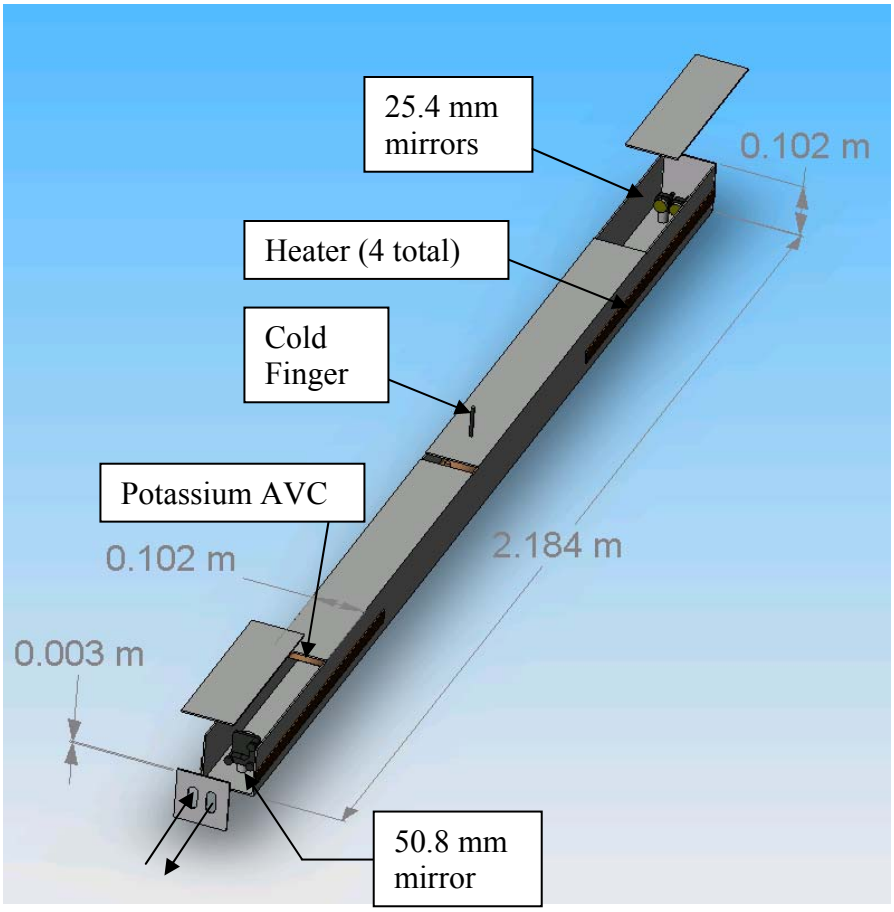

Figure 5-4 Solidworks model of the AVC inside the aluminum heater. Note that there are only two holes for the input and output light. The White-cell mirrors can be easily accessed by removing a portion of the top of the heater at each end. A layer of insulation which enclosed the entire cell is not shown.

5.5.2 Verification of AVC theory

In order to better understand the AVC, to verify predicted characteristics, and to verify the operation of the cell, an iodine absorption feature was measured [46]. The measurement setup is shown in Figure 5-5. Short-duration pulses were emitted by a Ti:Sapphire laser and directed through an AVC to generate the wavelength scan. The scan was then directed through an iodine cell in order to measure an iodine absorption feature.

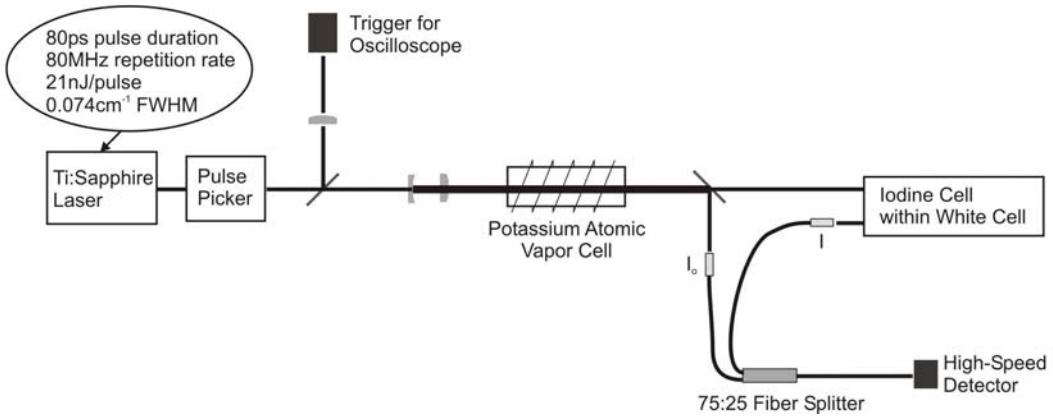

Figure 5-5 Schematic of the experiment. The laser is expanded prior to transmission through the atomic vapor cell to avoid nonlinearities.

A Spectra-Physics Tsunami Ti:Sapphire laser emitted pulses of 80 ps duration at 80 MHz repetition rate and was tuned near the potassium D1 line. The laser energy was 21 nJ/pulse and the spectral FWHM was estimated as 0.171 cm^{-1} based on manufacturer data. A pulse picker was used to select one pulse approximately every 51 μs. About 8% of this beam was directed into a detector in order to provide a trigger signal for the oscilloscope (Tektronix TDS7404 – 4 GHz analog bandwidth, 20 Gs/s). The remainder of the beam was expanded and collimated prior to entering the potassium AVC. The beam was expanded to avoid nonlinear processes that could occur in the potassium. The atomic vapor cell was a 0.3 m long Pyrex cell containing only potassium metal in the presence of a vacuum. The cell was heated to approximately 390 K; the vapor pressure of potassium at this temperature is 0.0135 Pa. Unlike in the current experiment this cell did not have Brewster angle windows because the laser only passed through the cell once. Figure 5-6 shows the attenuation, scan rate, and excess delay of the AVC used in this experiment at the above conditions. The location of the iodine line is advantageous because the scan rate is low and the attenuation is tolerable.

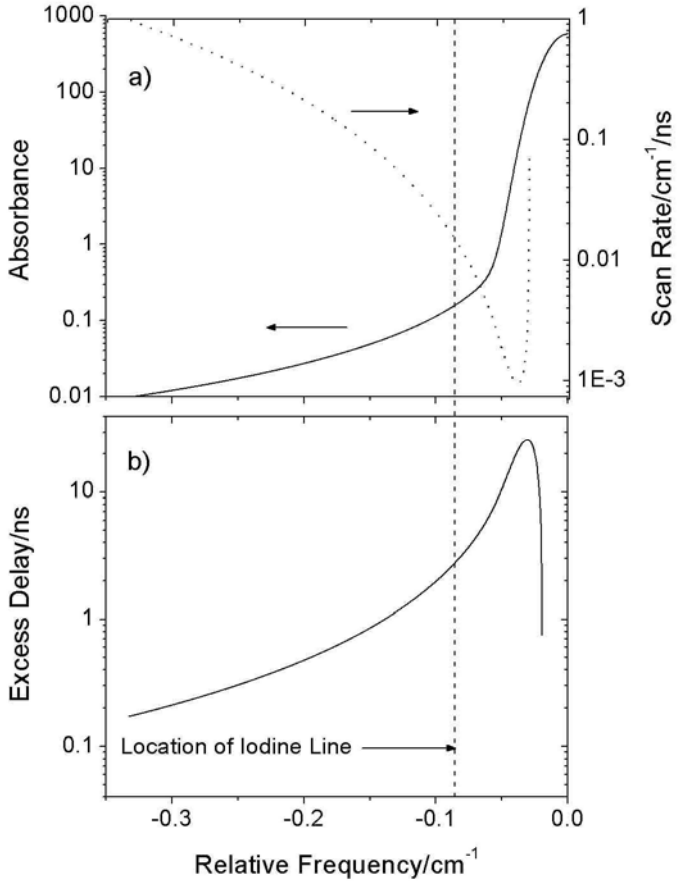

Figure 5-6 Theoretical characteristics of potassium at 12985.17 cm^{-1}, 390 K, and 0.3 m. Only the red side is shown, but the blue side is roughly symmetric. a) Absorbance and scan rate. b) Excess delay time. The absorbance is the convolution of a Gaussian and Lorentzian line shape, with the Lorentzian line shape dominating in the wings. The excess delay is based on the real part of the electric susceptibility while the absorbance is based on the imaginary part. The scan rate is the inverse of the derivative of the excess delay with respect to frequency.

The beam was refocused prior to entering the iodine cell. The iodine cell contained iodine crystals in the presence of a vacuum. The windows of the cell were attached at Brewster's angle in order to minimize reflection and the cell was 1.4 m long at the center of the windows. The cell was placed between mirrors forming a multi-pass White-cell configuration to achieve a total path length of 11.2 m of iodine. The reason for the long cell is that the iodine feature of interest has a high lower-state energy (estimated to be 2800 cm^{-1}) and is therefore relatively weak at ordinary temperatures.

The iodine cell body was heated to 471 K while a cold finger at the center of the cell was held at approximately 320 K, resulting in a vapor pressure of 235 Pa. At this condition, the collisional broadening was approximately 1/18 of the Doppler broadening; the latter is calculated to be 0.012 cm^{-1} at 12985 cm^{-1}. The collisional broadening was calculated by multiplying the broadening coefficient, 0.2 ± 0.05 cm^{-1}/atm [47], by the vapor pressure of iodine. An 8% beam splitter was used to pick off the reference signal ("I_o") just after the light passed through the potassium cell. The signal transmitted through the iodine cell ("I") was then multiplexed with the I_o signal using a 75:25 fiber splitter, with the I signal passing through the 75% branch. The I signal traveled through a longer distance, so when the two signals were recorded by the oscilloscope the I_o signal appeared approximately 62 ns prior to the I signal. In this way both I and I_o were obtained in the same measurement using the same high-speed detector (New Focus 1480). This "time-of-flight multiplexing" approach has been particularly stable and reliable in these types of experiments. Note that the apparent imbalance in the multiplexing (8% x 25% = 2% for I_o vs. 92% x 92% x 75% = 63% for I) was made-up in the iodine cell, due to both White-cell mirror losses and "broadband" absorption in I_2 vapor. The latter loss was dominant; near 770 nm but tuned away from I_2 resonances, the net iodine transmission (corrected for mirror losses) was on the order of 2%. This broadband I_2 absorption is presumed to be due to a predissociative transition.

To verify the performance of the AVC the $R(101)$ $A^3\Pi_{1u}$-$X^1\Sigma^+_g(0,13)$ iodine feature was measured with the AVC as well as with a diode laser. A diode laser has relatively narrow line width, so it was used to perform a high-resolution measurement of the iodine feature. This measurement was then treated as a standard for comparison with

the AVC measurement. The diode laser was a New Focus model 6312. This laser was directed through the iodine cell and White-cell at the previously described conditions. After exiting the White-cell, the diode laser passed through a room-temperature, 7.62 cm long potassium cell with no buffer gas and the signal was measured with a Thorlabs PDA55 detector. This potassium cell was not used to create a wavelength-agile scan, in this case the potassium D1 absorption line was merely used as a frequency standard. A 50 Hz sawtooth signal was applied to the frequency modulation input of the diode laser to cause it to scan over the potassium line and several iodine lines. Figure 5-7 displays the result of this scan, which was obtained in a single scan. The Doppler width of the potassium line at room temperature (0.0258 ± 0.0002 cm^{-1}) was used as a scale to estimate the line width of the iodine line. The measured iodine FWHM was 0.0232 ± 0.0002 cm^{-1}, which is wider than the Doppler width. However, the feature at 12985.0843 cm^{-1} contained multiple lines, most likely as a result of the hyperfine structure of iodine. The iodine feature at 12984.8994 cm^{-1} also contained multiple lines, resulting in a total FWHM of 0.0161 ± 0.0002 cm^{-1}. However the lines were not blended together to the same degree, so by modeling this feature as two Gaussian lines, an estimate for the Gaussian FWHM of 0.0124 ± 0.0002 cm^{-1} was made, which is within approximately 2% of the Doppler width. The separation between the iodine feature and the potassium line in this figure was 0.0814 cm^{-1}. This value is within 6% of reported literature values [48-50].

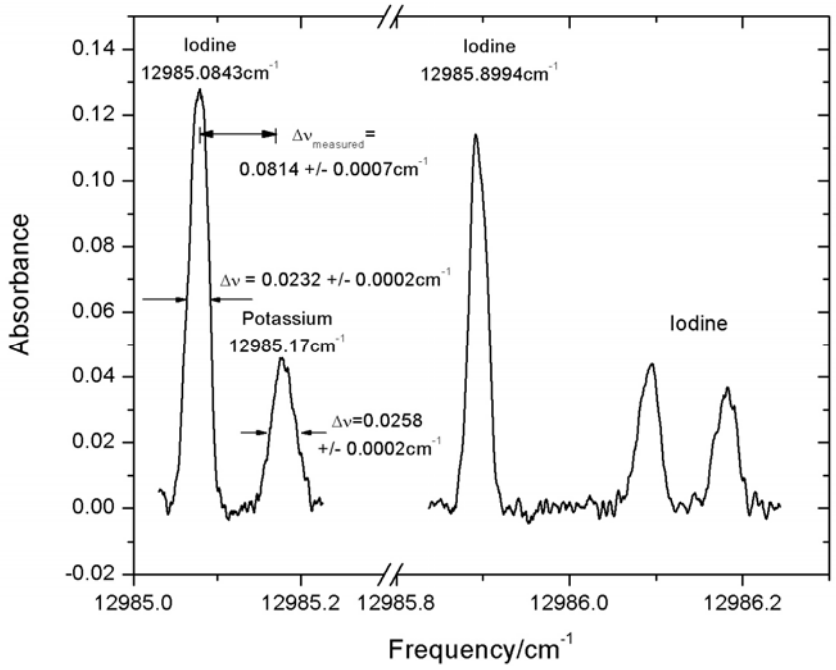

Figure 5-7 Absorbance spectrum of iodine as measured with a diode laser. A potassium cell was used to locate the *R*(101) $A^3\Pi_{1u}$-$X^1\Sigma^+_g$(0,13) iodine feature in the diode laser scan. It was also used to obtain a frequency scale by assuming the FWHM of the potassium line to be the Doppler width. The iodine line at 12985.0843 cm^{-1} is wider than the Doppler width because it contains multiple lines, but the width of the iodine feature at 12985.8994 $cm^{-1}$is within 2% of the calculated Doppler width. The data were obtained in a single scan over approximately 12.5 ms.

A measurement of the same iodine feature using the AVC to create a wavelength-agile scan was then obtained. The results of this measurement are shown in Figure 5-8, which was obtained from 1000 averages and used as the basis of subsequent figures. Figure 5-8 represents the direct output from the fiber splitter, except for a simple processing step: in the raw data the *I* signal appears approximately 62 ns after the I_o signal, but in this figure the *I* signal has been translated and scaled so that it overlays the I_o signal. The discrepancy between the two traces near the peak amplitude was due to iodine absorption. This figure displays the data against both time and relative frequency, where the frequency is relative to the potassium line center. The raw data were measured on a temporal scale and converted to a spectral scale using the data in part (b) of Figure

5-6; because of the dramatic variation in delay shown in Figure 5-6, the shape of the curve changed when the temporal scale was converted to a spectral scale. In order to illustrate this change, corresponding points on the temporal and spectral curves are labeled in Figure 5-8 as a and a', b and b', c and c', and d and d', respectively. The temporal data clearly show a steep progression from point a to b, whereas the spectral data show a more gradual progression from a' to b'. The reverse is true for the progression at the end of the scan; the change from c to d is gradual and the change from c' to d' is steep. The net result is that the apparent peak in the spectrum was shifted.

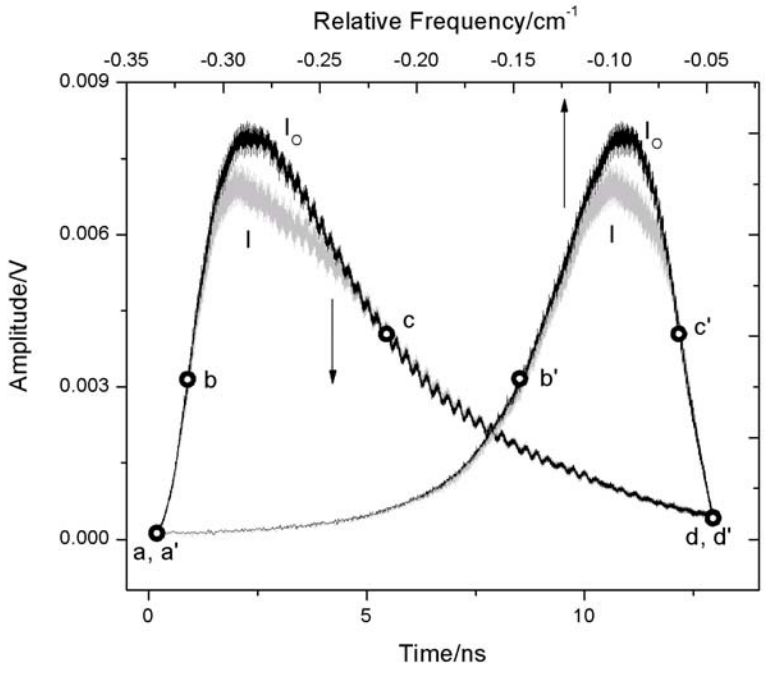

Figure 5-8 Iodine is visible as the difference between *I*, recorded after the iodine cell, and I_o, recorded before the iodine cell. When the time axis was converted to frequency the data that were stretched in time were shortened in color. In order to clearly see this, points which represent the same data are labeled a and a', b and b', c and c', d and d'. This figure represents 1000 averages. The frequency axis is relative to the potassium line.

The I_o trace plotted versus the top (frequency) axis in Figure 5-8 approximates the laser spectrum. However, because of the wavelength-dependent absorption of the

potassium, the trace does not appear symmetric. Figure 5-8 was smoothed using a first order Butterworth filter and then the amplitude was corrected for potassium absorption using the data from Figure 5-6, resulting in the laser spectrum shown in Figure 5-9. The laser spectrum FWHM was measured as 0.074 cm^{-1}. After comparing the fitting of several different curve shapes to the laser spectrum data it was determined that a Lorentzian line shape provided the best fit. The result of a Fourier transform on the Lorentzian fit resulted in a temporal FWHM of 105 ps, which was 24% greater than the reported 80 ps laser FWHM. Another interesting feature of Figure 5-9 was the ripples which are visible in the portion of the spectrum nearest the potassium line. The Ti:Sapphire laser has an 80 MHz (0.0027 cm^{-1}) mode structure. In this experiment the resolution was never high enough to entirely resolve the mode structure, but the expectation was that the mode structure would be partially resolved as a weak 80 MHz structure modulating the laser spectrum. However, the ripples did not occur at a consistent 80 MHz; the measured structure varied steadily from approximately 90 MHz (far from the potassium line) to 20 MHz (near the potassium line).

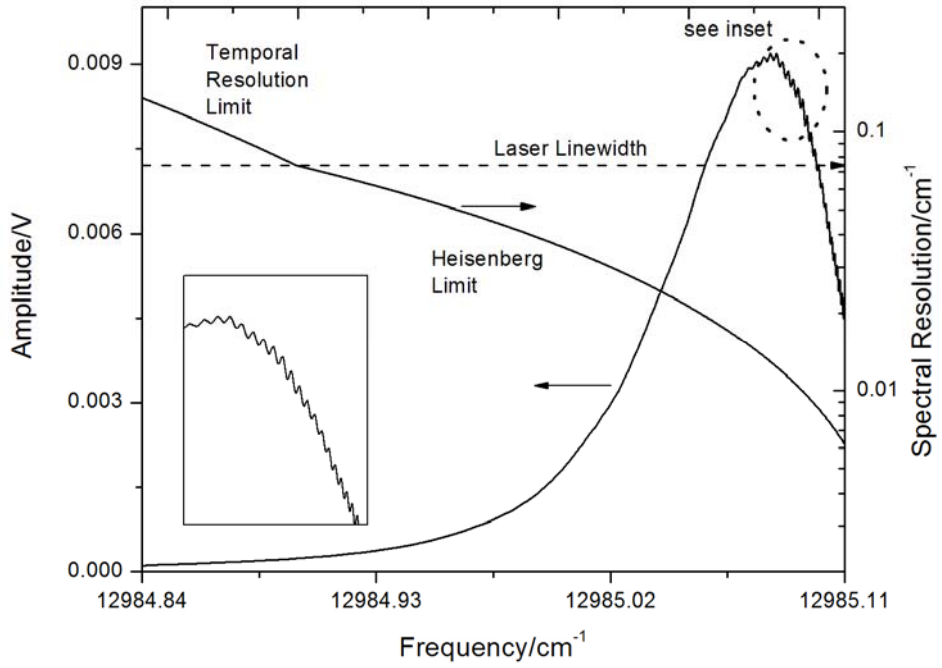

Figure 5-9 Laser spectrum derived from measurements after the potassium atomic vapor cell. The FWHM is less than expected. The inset figure is a close up of a portion of the curve which displays the ripples in more detail.

There were two unexpected results of using the potassium AVC as a spectrometer for the laser pulse. First, the temporal FWHM calculated from the measured spectral FWHM, even assuming perfectly transform-limited operation, was 105 ps rather than the actual 80 ps. Second, the ripples, which were assumed to be due to the mode structure of the laser, were not measured as a consistent 80 MHz. These two results indicate that the simple time-to-frequency mapping based on Figure 5-6 (b) may be over-simplified. To further investigate the appropriateness of this mapping, detailed simulations of pulse propagation through highly dispersive media have been begun. This research is still in progress [51].

Although the AVC can not be used as a reliable spectrometer for the laser pulse until the pulse propagation in the potassium vapor is better understood, it could be used to measure the iodine absorption feature, which was derived from the data in Figure 5-8. Beer's law (Equation (5-1)) was applied to the filtered data and the iodine absorption feature was obtained.

$$\alpha = -\ln \frac{I}{I_o} \tag{5-1}$$

Figure 5-10 shows the result of this calculation as well as the spectral resolution across the iodine feature.

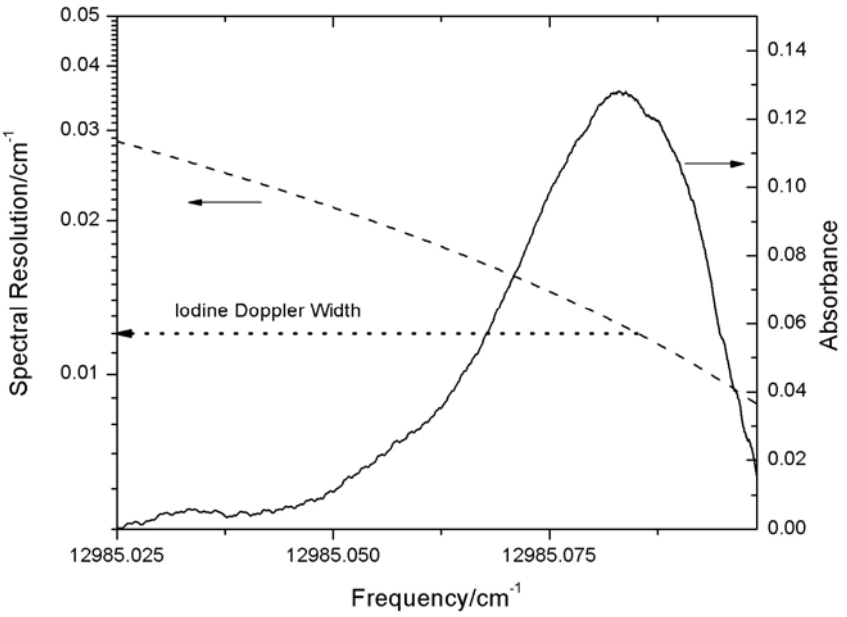

Figure 5-10 Iodine absorption spectrum measured using the wavelength-agile scan. The spectral resolution varies with distance from the potassium absorption line. Where the spectral resolution is greatest, artificial broadening of the iodine absorption feature is expected to be most severe.

In accordance with the varying scan rate, the spectral resolution gradually improved toward the potassium side (right side) of Figure 5-10. Calculated spectral

resolutions are shown in Figure 5-9 and Figure 5-10 for reference. The variation implies that the measured spectra would be more fully resolved nearer the potassium feature. In Figure 5-11 the iodine spectrum measured using the diode laser scan was overlaid on the iodine spectrum in Figure 5-7. The two spectra match fairly well; some of the discrepancies may be due to an artificial broadening of the line associated with the variable spectral resolution of the agile measurement. It is also theorized that the potassium AVC does distort the iodine line in much the same way that the laser line is distorted. Due to the use of averaging and the jitter in the laser pulse, much of the distortion in the iodine signal is "smeared" out, resulting in a measurement that may be useful for some purposes.

The diode laser measurement data had a moderate signal-to-noise ratio (minimum detectable absorbance of 0.005) due to a low transmitted power (~ 90 nW). A weak diode laser and broadband absorption in the iodine were responsible for the low power. The atomic vapor cell scan had about 2400 times the power of the diode laser scan, allowing measurements of comparable quality in a shorter time. Considering the 1000 averages in the AVC data, the cumulative time for the acquisition was 12.5 μs, almost 1000 times shorter than the diode laser scan. In order to compare the two measurements, a theoretical minimum detectable absorbance (MDA) for the AVC scan was estimated based on the diode laser scan results. First, the MDA was scaled by the square root of the ratio of the cumulative measurement durations. Thus, it was estimated that a 90 nW AVC scan would result in a MDA of 0.16 (square root of 1000 times the diode laser MDA of 0.005). This MDA was then scaled to account for the power difference between the two scans by dividing by 2400, resulting in a value of about $7*10^{-5}$. Finally, the high-

speed detector used for the AVC measurement has a noise equivalent power approximately 11 times the detector used for the diode scan. The theoretical MDA for the AVC scan was degraded accordingly to obtain an estimate of $8*10^{-4}$. This estimate places the MDA for the AVC within an order of magnitude of that for the diode laser scan, and in rough agreement with the data shown in Figure 5-11.

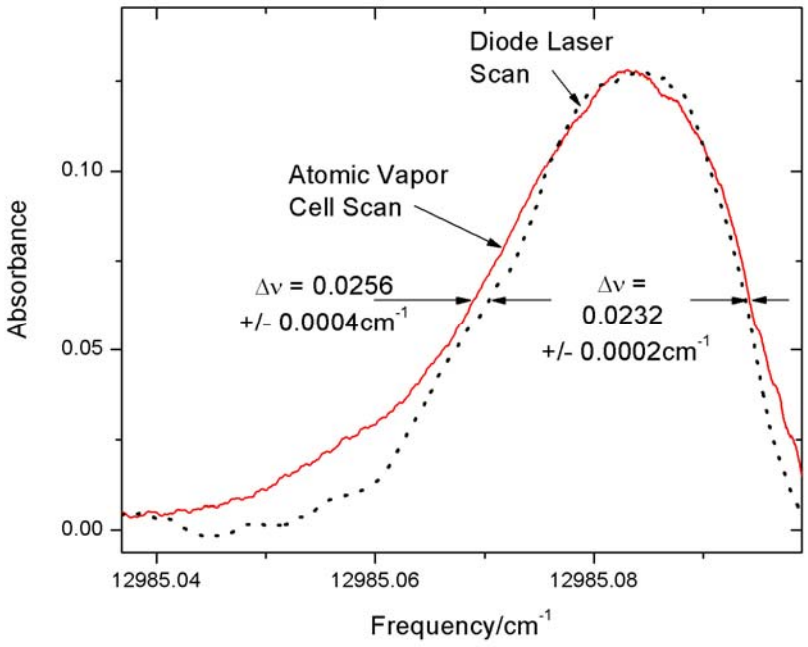

Figure 5-11 The iodine absorption feature measured using the diode laser scan and the atomic vapor cell scan compare favorably.

5.5.3 Effects of AVC on the measurement

As indicated by the measurement of the laser spectrum in the experiment described in the previous section, the atomic vapor cell distorts a signal [51]. Since the completion of this experiment several references [39, 52, 53] have been located which indicate that in anomalous dispersion the signal is strongly distorted. The current conceptual understanding of the cause of the distortion relates to interference. All pulses, even extremely spectrally narrow pulses, are composed of multiple colors. These colors

interfere in a given way to produce the spectral envelope. The potassium preferentially absorbs certain colors, thereby changing the interference pattern and leaving "gaps" in the spectrum. In the case of the iodine line, the use of averaging and the jitter in the laser resulted in some of those gaps being filled in, and therefore the measurement did not appear to be terribly distorted. However, it must be noted that some distortion does occur; therefore, even in the measurement of an absorption line, care must be taken.

5.6 Photon counting

The Rayleigh scattering signal is inherently weak and it is further attenuated by the AVC; simulations indicated that on average less than one photon would be incident on the detector per measurement. For this reason photon counting was the detection method of choice. Photon counting uses an extremely sensitive photomultiplier tube (PMT) in combination with a discriminator in order to count individual photons.

5.6.1 Photomultiplier tube

A PMT is generally constructed of an evacuated glass tube. On one end of the tube is a photocathode, which is a material that may emit an electron when a photon is incident upon it, and the other end of the tube is the anode. Different materials are sensitive to different wavelengths and in general materials are more sensitive to bluer wavelengths. In the situation when a photon interacts with the photocathode and an electron is emitted, the electron is attracted to a dynode which is near the photocathode. When the electron strikes the dynode secondary electrons are released. This group of electrons is then directed through a series of dynodes, with the number of electrons increasing throughout the dynode chain. The total amplification of the initial signal is

determined by the amount of voltage applied to the dynode chain, in a photon counting PMT the gain can be as much as a factor of 10^7. At the end of the dynode chain the electrons are collected at an anode, thereby providing a current which is then output from the PMT [54].

PMT's are characterized by several factors including noise, quantum efficiency, and rise time. Noise has several causes. First there is shot noise, which is due to the fact that current is just the flow of discrete electrons. This means that there are fluctuations in the flow. If the current is small then it can be assumed that the electrons behave independently and Equation (5-2) holds true [55].

$$I_{noise} = \sqrt{2qI_{dc}B} \tag{5-2}$$

B [Hz] is the measurement bandwidth, q [C] is the charge of an electron, and I_{dc} [A] is the value of the steady current. As indicated by this equation, the smaller the current, the larger the relative fluctuation of the current, therefore this noise dominates in weak signals.

Another form of noise is dark noise, which is present even when no signal is applied to the photocathode. It is a result of a small current which is always flowing through the anode circuit for a variety of reasons. In this experiment the PMT is operated at high voltages where the dominant dark noise is due to thermionic emission. Thermionic emission occurs when the photocathode randomly emits an electron even though no photons are present. This electron is amplified through the dynode chain; therefore the amplitude of this noise is proportional to gain. Thermionic emission is difficult to identify because it is random. It should be noted that in the realm where this

noise dominates, the signal-to-noise ratio remains steady as gain is increased because both the signal and the noise are proportional to gain. Because it is a function of temperature, thermionic emission can be minimized by cooling the PMT.

Regenerative noise is another source of dark noise. It occurs at high gain and is erratic. One source is dynode glow, in which the dynodes emit blue light in response to electron bombardment from light reflected from the photocathode. This effect can be minimized by shielding the dynode chain. Afterpulsing is another source of regenerative noise; it occurs when a secondary pulse is emitted from the PMT after the initial pulse. It generally occurs with short pulsed signals and it can be created by the ionization of gas in the area around the photocathode. This pulse is usually delayed from the actual signal by 0.2 to 1 μs. These are the primary sources of noise, although cosmic rays and previous light exposure can also lead to noise.

The other two most important factors in selecting a PMT are quantum efficiency (QE) and rise time. QE is a measure of how often an electron is emitted from the photocathode when a photon is present. This value varies with material and wavelength from 0% to 100%, which is the desired value. Equation (5-3) quantifies the value.

$$\eta = \frac{hc}{q}\frac{\sigma}{\lambda} = 124\frac{\sigma}{\lambda} \tag{5-3}$$

h [Js] is Planck's constant, c [m/s] is the speed of light in a vacuum, q [C] is the charge of an electron, σ [mA/W] is the responsivity of the photocathode, λ [nm] is the wavelength and η [%] is the efficiency. An event occurs every time an incident photon results in an electron. The rise time is the amount of time required for the PMT output pulse to rise

from 10% to 90% of the peak amplitude. As in the case of this experiment, a small value of the rise time is required when high temporal resolution is desired [54].

Now that the relevant variables have been defined, the noise can be quantified as it relates to photon counting. In this case the shot noise is not represented by Equation (5-2) because the signal is not very strong. Instead of a current, the noise is measured in terms of counts. The signal-to-noise ratio (*SNR*) is calculated from the various components of the noise: shot noise associated with the signal, n_{ph}, the background, n_b, and the PMT dark counts, n_d. The equations for each noise source are presented below.

$$n_{ph} = \sqrt{N_{ph}} \tag{5-4}$$

$$n_b = \sqrt{N_b} \tag{5-5}$$

$$n_d = \sqrt{N_d} \tag{5-6}$$

N_{ph} is the number of counts from the signal light, N_b is the number of counts from the background light, and N_d is the number of counts from the PMT dark noise. The value of N_{ph} can not be directly measured because N_b and N_d are always present during this measurement. Instead measurements must be made with the signal light on and then with the signal light off. These two measurements are subtracted in order to obtain the value of N_{ph}. The total noise level, n_{tot}, is given in Equation (5-7).

$$n_{tot} = \sqrt{N_{ph} + 2(N_b + N_d)} \tag{5-7}$$

The *SNR* is just the signal divided by the noise and is presented in Equation (5-8). It is also common for this ratio to be calculated on a time basis. N'_{ph}, N'_b, and N'_d are calculated by dividing N_{ph}, N_b, and N_d by the measurement time, t [s], respectively. The *SNR*, factoring in time, is presented in Equation (5-9).

$$SNR = \frac{N_{ph}}{\sqrt{N_{ph} + 2(N_b + N_d)}} \tag{5-8}$$

$$SNR = \frac{N'_{ph}\sqrt{t}}{\sqrt{N'_{ph} + 2(N'_b + N'_d)}} \tag{5-9}$$

The possible noise degradation of the signal can be quantified by calculating a detection limit (a.k.a. equivalent noise input, ENI, or noise equivalent power, NEP). The detection limit is a measure of what the signal strength needs to be in order to maintain the *SNR* at one. The detection limit is shown in Equation (5-10), where t is 1 s and N'_b is negligible.

$$SNR = 1 = \frac{N'_{ph}}{\sqrt{2(N'_d)}} \tag{5-10}$$

The incident power, P_o [W], at the detection limit can be calculated using Equation (5-11), in which η is no longer in percent and λ is in units of nm; h [Js] is again Planck's constant and c [m/s] is the speed of light [56].

$$P_o = \frac{hc}{\lambda}\frac{\sqrt{2(N'_d)}}{\eta} \approx \frac{2.8 \cdot 10^{-16}\sqrt{N'_d}}{\lambda\eta} \tag{5-11}$$

The PMT selected for this experiment was H7422P-50 from Hamamatsu Corporation. The photocathode material was GaAs and it was designed for photon counting; the maximum gain was approximately $2*10^6$. Peltier elements were used in conjunction with an external heat sink, in this case a water cooled aluminum block, to cool the PMT and minimize dark counts. The dark counts were specified as nominally 125 counts/second with a maximum of 300 counts/second. The QE at 770 nm was

approximately 14.5%, which corresponds to responsivity of 90 mA/W. The rise time was 1 ns. Using these values the incident power at the detection limit, calculated using Equation (5-11) and the maximum dark count value of 300 counts/second, is $4.34*10^{-17}$ W. Based on a laser pulse rate of 5000 pulses/second, this corresponds to an energy of $8.7*10^{-21}$ J, which corresponds to a requirement of about 0.03 photons per measurement for a *SNR* of one.

5.6.2 Discriminator

The second component required for photon counting was a combination amplifier and discriminator. The output of the PMT was very low, which is why it was directed through an amplifier prior to entering the discriminator. The discriminator was used to eliminate as much noise from the signal as possible. In this experiment a Phillips Scientific 6908 combination 300 MHz amplifier and discriminator was used. It had a threshold setting (variable from -1 mV to -100 mV) which determined the lowest signal level which was to be considered a photon. For example, if the threshold was set to 10 mV only signal levels exceeding 10 mV would be counted as photons. Using this function noise such as dark counts, which are generally weaker in amplitude than the signal, could be reduced without degrading the signal. This setting had limited value in this experiment because the signal amplitude was often on the same level as the noise. A width setting could be adjusted such that the FWHM of the discriminator output pulse was as small as 2 ns. The pulse-pair resolution of the 6908 was less than 3.3 ns, which means that if there were two events in less than 3.3 ns, only one event was recorded.

5.6.3 Oscilloscope

The discriminator was connected to a Tektronix TDS 7154 Digital Phosphor Oscilloscope with a 1.5 GHz bandwidth and 20 GS/s; the measurements were obtained at a 10 GS/s rate. The histogram function of the oscilloscope in conjunction with a delay measurement was used to construct the signal. The delay between a trigger pulse and a photon was measured and each photon was assessed as a count in the histogram. A measurement was taken when the laser was tuned away from the potassium absorption line in order to determine at what time an event occurred if there was no interaction with the potassium. This time was compared to that obtained when the laser was tuned near the potassium line in order to obtain the excess delay induced by the potassium. These measurements required 10 to 40 minutes to complete.

5.6.4 Advantages and disadvantages

Photon counting has the advantage of being an on or off measurement; either there is a signal which indicates a photon or there is no signal, indicating no photon. Assuming a strong enough signal, most noise can be eliminated by the discriminator. The amplifier noise and thermionic emission from the dynodes can be discriminated because they are weak sources of noise. However, due to the weak nature of this signal, not all noise could be eliminated.

The sensitivity of photon counting is both an advantage and a disadvantage. It was difficult to eliminate stray light. Initially the pulse picker was placed before the fiber, so any light due to scattering from surfaces and reflections was recorded at the same time as the scattered signal, overwhelming the signal. The only way to eliminate

this spurious signal was to change the setup by placing the pulse picker after the fiber and setting the delay time such that only scattering from within the fiber would be recorded.

Chapter 6 Experimental Results

The scattering in a fiber was measured using the setup in Figure 5-1. Figure 6-1 shows the results of the measurements. In this figure four sets of data are plotted. Each set was measured at a different position relative to the potassium absorption line; position 1 was far from the line and position 4 was near the line. As in Figure 4-2, as the signal neared the potassium line the spectrum was attenuated and broadened. The spectral envelope was also distorted by the potassium. Using the methods outlined in section 5.6.1 the signal level, represented by the number of histogram counts, that corresponded to a SNR of one was calculated and plotted in the figure. All data below these lines are suspect. When measurements were made with the laser tuned near the potassium line, there was a peak located at an excess delay of zero. This peak was due to the imperfection of the laser seeding. In this experiment the oscilloscope was triggered by the Q-switch on the laser, therefore every time there was a laser pulse, whether or not it was seeded, the oscilloscope recorded data. The unseeded laser is spectrally broad, so most of the unseeded light was far from the potassium line frequency. The peak located at zero in the position 2, 3, and 4 data was due to this unseeded light.

Figure 6-1 also shows that there was a lot of noise in the signal. In a multimode fiber the light is partially depolarized, therefore the scattered light is partially depolarized. A polarizer was placed before the pulse picker in order to select one polarization. The pulse picker operates based on polarization; if the input light is perfectly polarized then when the pulse picker is off, no light passes through, but when the pulse picker is on, all of the light passes through. If the input light is not perfectly polarized, or the pulse picker

is poorly aligned or malfunctioning, then light of the wrong polarization will leak through the pulse picker. This is the situation in these measurements, however it is unknown if the cause is poor performance of the pulse picker or poor performance of the polarizer. By improving this portion of the setup the noise would be significantly reduced.

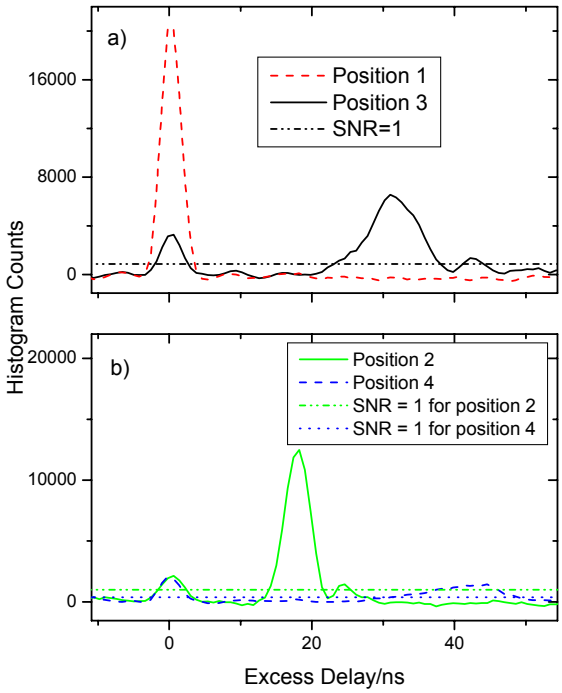

Figure 6-1 Results of scattering measurement in a fiber. The two figures show measurements made at varying distances from the potassium line. Position 1 is furthest from the line and position 4 is closest to the line. The number of counts that equate to a SNR of 1 is also shown. All data below these lines are suspect.

Several references which contain figures of Rayleigh and Brillouin scattering in various kinds of glass were located in order to try to verify the results of these measurements [57-60]. Most references indicate that the spectral shape is approximately Gaussian and the FWHM is 2 GHz or less, but these measurements are limited by the spectral resolution. The purpose of most of these references is not to resolve the

Rayleigh scattering spectrum, but rather to measure the intensity of the scattering and locate the Brillouin sidebands. The result is that the Rayleigh measurement is incidental and it is not measured with high resolution.

Assuming, however, that these references were adequate, a model of the Rayleigh scattering spectrum with a FWHM of 2 GHz was created. This model was then distorted for attenuation and dispersion in potassium, but not for the more advanced distortion which occurs in the potassium; the data were plotted on a temporal rather than spectral axis. This initial model was compared to the measurement results and the comparison was very poor. The modeled data were broader than the measured data near the potassium line. The FWHM was therefore reduced to 0.5 GHz and this model compared more favorably, although it was still somewhat too broad.

Another reference only partially shows the Rayleigh spectrum [61], but it does show a very detailed Brillouin spectrum measured with a resolution of approximately 50 MHz. This reference indicates that the Brillouin FWHM is on the order of 15 MHz. Based on the significantly higher resolution and the supposition that the Rayleigh scattering spectrum FWHM is similar to that for Brillouin scattering, it is possible that Rayleigh scattering in glass is extremely narrow. If it is on the order of 15 MHz and the laser is on the order of 27 MHz, then the data in Figure 6-1 are actually a measurement of the laser; the convolution of the Rayleigh scattering spectrum and the laser spectrum would result primarily in the laser spectrum.

The scattering in a fiber is not necessarily that useful in itself, but it provides a stepping stone to evaluate the feasibility of completing measurements using this methodology in a gas or liquid. It is estimated that the scattering intensity in a fiber is

approximately 1000 times that in a high pressure gas. This approximation accounts for the long length of scattering in the fiber as well as the higher density of a solid versus a gas. The situation for a gas would be improved because filters could be removed from the setup as there would no longer be any danger of damaging a fiber. In order to test the feasibility of this situation a measurement of the scattering was made with the laser tuned away from the potassium and then a second measurement was made with filters inserted into the path of the scattered light. The total filtering had an optical density of 3.1, corresponding to a reduction in the signal strength of 0.0008. The results of these measurements are shown in Figure 6-2. Although the filtered signal was recorded over 60 minutes while the stronger signal was recorded over 13 minutes, the filtered signal was significantly noisier. The total number of histogram counts for each measurement was divided by the total measurement time in order to estimate a flux. The unfiltered signal had a flux of 19.8 hits/s while the filtered signal had a flux of 1.5 hits/s. A reduction of the background noise would improve the signal and make it more feasible to measure a weak spectrum. The noise could be reduced by improving the pulse picker alignment and also the polarization. The polarization would be improved in gas scattering because the scattered light would be polarized.

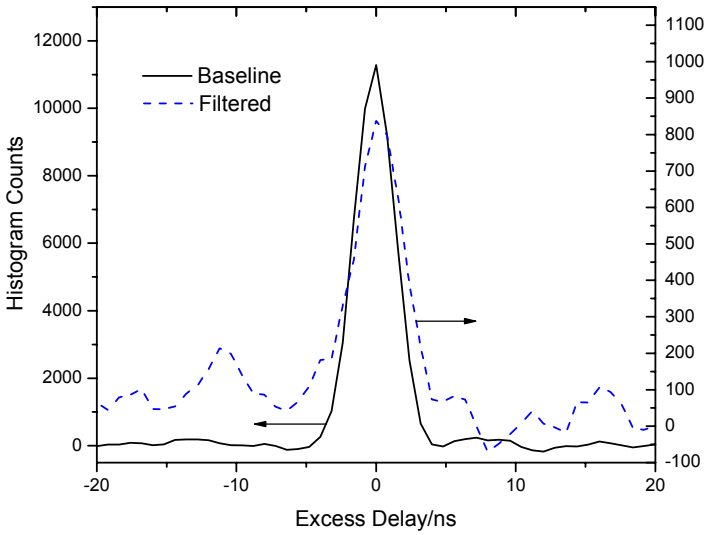

Figure 6-2 Comparison of a baseline measurement far from the potassium line and the same measurement made with filters with optical density of 3.1 placed in line. The filtered signal is considerably weaker and was measured over a longer time period.

Chapter 7 Conclusions and Recommendations

This research demonstrated the use of an atomic vapor cell in the creation of a wavelength-agile scan and the inherent difficulties in measuring a Rayleigh scattering spectrum. The initial goal of this research, to measure the properties in a vortex tube, was left unfulfilled; the final mission was to gain an understanding of the AVC and explore the difficulties in measuring Rayleigh scattering. These final sections outline some of the lessons learned and how they can be applied to future research.

7.1 Conclusions regarding the method

This research began with a seemingly straightforward idea, use an AVC to temporally disperse and therefore resolve a Rayleigh scattering spectrum. The experimental difficulties, however, were numerous. One of the first that was overcome was the difficulty of aligning the multi-component system. The White-cell composed perhaps the greatest challenge, but with practice the alignment became a non-issue. The layout of the experiment was large, covering the majority of an optical table (244 cm x 122 cm), but this size could be reduced if the method was deemed promising.

The more significant problems relate to the fundamentals of the AVC and Rayleigh scattering. The AVC distorts a signal passing through it. Before using the AVC for further measurements it first must be better understood. Can the AVC really be used for absorption measurements as it was used here? Can it be used for these measurements, but only under certain resolution constraints? The iodine line measured in this research was better than simulated versions because of averaging and jitter. The

random laser jitter helped remove some of the "wiggles" created by the AVC distortion. Preliminary simulations also indicate that the line shape is distorted, but the area, FWHM, and intensity may still be used to estimate the temperature, pressure, and number density of the absorber. Can the AVC be used with a weak signal? Will the same distortion take place? And can the distortion be predicted and possibly reversed in data reduction? All of these questions should be addressed before relying on the AVC output in making further measurements. As for Rayleigh scattering itself, the main problems are that it is extremely weak and narrow and the measurement of velocity will be difficult unless a very high velocity is present. These problems were well known prior to this research, which merely illustrated the difficulties.

7.2 Improvements and future work

Assuming the questions about the AVC result in a favorable response and it can be used for some measurements, there are many things that can be done to improve the chances of successfully measuring Rayleigh scattering. One option is to increase the diameter of the AVC in order to collect more light. Another improvement would be to remove the pulse picker and replace it with a laser with 3 – 4 ns pulse duration. This would remove alignment and efficiency problems and increase the power reaching the detector. The polarization of the light would also be less of an issue.

The next step would be to measure the Rayleigh scattering spectrum in something more interesting than a fiber, such as a liquid or gas. Given a steady state measurement volume, the spectrum should be partially resolved over a long measurement time. The scattered light would be polarized, eliminating some of the problems seen in the fiber

measurement. The spectral width is expected to be as broad as or broader than the fiber scattering FWHM due to the increased Doppler Effect caused by the movement of the gas molecules. The spectral shape would not need to be fully resolved in order to obtain temperature, pressure, and velocity information. If the location and intensity of the first two peaks in the three-peaked Rayleigh scattering spectrum could be resolved then the fluid properties could be estimated. Finally, the filters placed between the laser and the fiber in the fiber measurement could be removed, increasing power by a factor of 67. The beam splitter would also be removed, increasing the power by a further factor of four. Based on the measurements in Figure 6-2 and the suggested improvements, it is feasible to measure the Rayleigh scattering spectrum.

There are still challenges. One of the most daunting is the alignment of the system. Recall that in the case of the fiber measurement a visible light source was directed through the fiber and the system was aligned using this signal. In the case of scattering in a gas this is not possible. The scattered light will be too weak to use, but it is possible that by placing something, such as a pin, at the point where the laser focuses, the system could be aligned. Whatever is used would have to be removable so that it would not interfere with the actual measurement. The alignment system can be worked out, but it will take some effort. In order to produce a strong signal the gas will have to be high pressure, so it is unlikely that this technique could be used with the vortex tube.

As for the vortex tube, there are several possibilities. The method described in this research is not recommended. The difficulties are extreme and there are other options. Rather than measuring temperature, pressure, and velocity all with one technique, a focus on measuring just one of these parameters would lead to a simpler

method that provides enough information to improve computational fluid dynamic models. For example, a fluorescence method could be used to obtain spatially resolved measurements of temperature. In this method a tracer such as acetone or formaldehyde would be added to the vortex tube. Two different colored lasers would be focused into the vortex tube and the fluorescence intensity at each frequency would be measured at 90° to the direction of laser propagation. The ratio of the intensity of these two fluorescence signals would be calculated; this ratio varies with temperature. The density could be determined by using the two-photon xenon absorption method described in section 3.4.

7.3 Final thoughts

Although the original project goal was not met, this research was still successful in advancing the understanding of some complex concepts. Without conducting this research the problems associated with using an AVC would not have been revealed to these researchers, leading them to believe that this was a simple method. Although the AVC should not be abandoned, it should not be considered as a primary tool for wavelength-agile research until it is fully understood. Rayleigh scattering, likewise, should be further pursued. Many of the experimental difficulties were discovered in the process of this research and can therefore be avoided in future. If Rayleigh scattering is to be measured it is recommended that an etalon or a filtered Rayleigh scattering system [10] be used rather than creating a wavelength-agile spectrum.

References

[1] Aljuwayhel,N. F., 2003, "Internal Study of the Vortex Tube using a CFD Package," .

[2] McCartney,E. J., 1976*, Optics of the Atmosphere : Scattering by Molecules and Particles*, Wiley, New York, pp.xv, 408.

[3] Zhao,H., and Ladommatos,N., 1998, "Optical Diagnostics for in-Cylinder Mixture Formation Measurements in IC Engines," Prog.Energy Combust.Sci.**, 24**, pp. 297-336.

[4] Hecht,E., 2002*, Optics*, Addison-Wesley, Reading, Mass., pp.vi, 698.

[5] Miles,R. B., Lempert,W. R., and Forkey,J. N., 2001, "Laser Rayleigh Scattering," Measurement Science and Technology**, 12**, pp. R33-R51.

[6] Zhao,F. -Q, and Hiroyasu,H., 1993, "Applications of Laser Rayleigh Scattering to Combustion Diagnostics," Progress in Energy and Combustion Science**, 19**(6), pp. 447-485.

[7] Mansour,M. S., Bilger,R. W., and Dibble,R. W., 1988, "Raman/Rayleigh and Mie-Scattering Measurements in a Reverse Flow Reactor Close to Extinction," 22nd Symposium on Combustion/The Combustion Institute**, 22**, pp. 711-719.

[8] Miles,R. B., and Lempert,W. R., 1997, "Quantitative Flow Visualization in Unseeded Flows," Annu.Rev.Fluid Mech.**, 29**, pp. 285-326.

[9] Robben,F., 1975, "Comparison of Density and Temperature Measurement using Raman Scattering and Rayleigh Scattering," Proc.of the Project SQUID workshop on combustion measurements in jet propulsion systems, pp. 180-196.

[10] Forkey,J. N., Lempert,W. R., and Miles,R. B., 1998, "Accuracy Limits for Planar Measurements of Flow Field Velocity, Temperature and Pressure using Filtered Rayleigh Scattering," Exp.in Fluids**, 24**, pp. 151-162.

[11] Young,A. T., 1982, "Rayleigh Scattering," Phys Today**, 35**, pp. 42-48.

[12] Hanson,R. K., Webber,M. E., and Seitzmann,J. M., 1999-2000, "ME 264: Introduction to Spectroscopic Diagnostics for Gases," .

[13] Young,Andrew T., and Kattawar,George W., 1983, "RAYLEIGH-SCATTERING LINE PROFILES," **, 22**(23), pp. 3668-3670.

[14] Tenti,G., Boley,C. D., and Desai,R. C., 1974, "On the Kinetic Model Description of Rayleigh-Brillouin Scattering from Molecular Gases," Can.J.Phys.**, 52**, pp. 285-290.

[15] Howard,J. N., 1964, "John William Strutt, Third Baron Rayleigh," Appl. Opt.**,** **3**(10), pp. 1091-1011.

[16] Lindsay,R. B., 1970*, Lord Rayleigh the Man and His Work*, Pergamon Press Ltd., Oxford, pp.251.

[17] Physical and Theoretical Chemistry Laboratory, University of Oxford, , "Rotational Raman Spectroscopy," **, 4, 2005**.

[18] Demtroder,W., 1996*, Laser Spectroscopy*, Springer-Verlag, Heidelberg.

[19] Bednar,N. J., 2005"Pointwise Optical Sensing by Multi-Photon Absorption in Noble Gases: A Casestudy using Xenon,", University of Wisconsin-Madison, MSME.

[20] Tang,Z., Zaidi,S. H., and Miles,R. B., 2000, "Density Gradient Rubidium Dispersive Absorption Filter for Low Wavenumber Raman and Thomson Scattering,"*, AIAA -Aerospace Sciences Meeting and Exhibit, 38th, Reno, NV*, Anonymous eds.**, AIAA-2000-644**.

[21] Moore,J. H., Davis,C. C., and, Coplan,M. A., 1983*, Building Scientific Apparatus : A Practical Guide to Design and Construction*, Addison-Wesley Advanced Book Program/World Science Division, London ; Reading, Mass., pp.xiii, 483.

[22] Seasholtz,R. G., and Greer,L. C., III, 1998, "Rayleigh Scattering Diagnostic Measurement of Temperature and Velocity in Harsh Environments," AIAA.

[23] Seasholtz,R. G., Panda,J., and Elam,K. A., 2001, "Rayleigh Scattering Diagnostic for Dynamic Measurement of Velocity Fluctuations in High Speed Jets," AIAA**, 0847**.

[24] Pan,X., Shneider,M. N., and Miles,R. B., 2004, "Coherent Rayleigh-Brillouin Scattering in Molecular Gases," Phys. Rev. A**, 69**, pp. 33814-2.

[25] Sarkisyan,D., Varzhapetyan,T., Sarkisyan,A., Malakyan,Yu, and Papoyan,A., 2004, "Spectroscopy in an Extremely Thin Vapor Cell: Comparing the Cell-Length Dependence in Fluorescence and in Absorption Techniques," Phys. Rev. A**,** **69**(065802-1).

[26] Sarkisyan,D., Bloch,D., Papoyan,A., and Ducloy,M., 2001, "Sub-Doppler Spectroscopy by Sub-Micron Thin Cs Vapour Layer," Opt. Comm.**, 200**, pp. 201.

[27] Kranendonk,L. A., Walewski,J. W., Kim,T., and Sanders,S. T., 2005, "Wavelength-Agile Sensor Applied for HCCI Engine Measurements," Proc. Comb. Symp.**, 30**, pp. 1619-1627.

[28] Walewski,J. W., and Sanders,S. T., 2004, "High-Resolution Wavelength-Agile Laser Source Based on Pulsed Super-Continua," Appl.Phys.B**, 79**(4), pp. 415-418.

[29] Walewski,J. W., Borden,M. R., and Sanders,S. T., 2004, "Wavelength-Agile Laser System Based on Soliton Self-Shift and its Application for Broadband Spectroscopy," Appl.Phy. B**, 79**(8 SPEC ISS), pp. 937-940.

[30] Sanders,S. T., 2002, "Wavelength-Agile Fiber Laser using Group-Velocity Dispersion of Pulsed Super-Continua and Application to Broadband Absorption Spectroscopy," Applied Physics B**, 75**, pp. 799-802.

[31] Jeffries,J. B., Sanders,S. T., Zhou,X., Ma,L., Mattison,D. W., and Hanson,R. K., 2002, "Scanned-Wavelength Diode Laser Sensors for Harsh Environments," Proc.SPIE-Int.Soc.Opt.Eng.**, 4817**, pp. 88-95.

[32] Kranendonk,L. A., Caswell,A. W., Myers,A. N., and Sanders,S. T., 2002, "Wavelength-Agile Laser Sensors for Measuring Gas Properties in Engines," SAE 2003-01-1116.

[33] Chou,J., Han,Y., and Jalali,B., 2004, "Time-Wavelength Spectroscopy for Chemical Sensing," IEEE Photonics Technol.Lett.**, 16**(4), pp. 1140-1142.

[34] Tong,Y. C., Chan,L. Y., and Tsang,H. K., 1997, "Fibre Dispersion Or Pulse Spectrum Measurement using a Sampling Oscilloscope," Electron.Lett.**, 33**(11), pp. 983-985.

[35] Yalin,A. P., Barker,P. F., and Miles,R. B., 2000, "Characterization of Laser Seeding by use of Group-Velocity Dispersion in an Atomic-Vapor Filter," Opt.Lett.**, 25**(7), pp. 502-504.

[36] Kash,M. M., Sautenkov,V. A., and Zibrov,A. S., et al, 1999, "Ultraslow Group Velocity and Enhanced Nonlinear Optical Effects in a Coherently Driven Hot Atomic Gas," Phys.Rev.Lett.**, 82**(26), pp. 5229-5232.

[37] Phillips,D. F., Fleischhauer,A., Mair,A., and Walsworth,R. L., 2001, "Storage of Light in Atomic Vapor," Phys.Rev.Lett.**, 86**(5), pp. 783.

[38] Haag,H. W., Otten,E. W., Schick,M., and Weinheimer,C., 1999, "Discussion of Dispersion Relations in Atomic Spectra with Respect to Experimental Demonstration," Eur.J.Phys.**, 20**, pp. 221-229.

[39] Brillouin,L., 1960*, Wave Propagation and Group Velocity*, Academic Press, New York, pp.154.

[40] Wehe,S. D., 2000"Development of a Tunable Diode Laser Probe for Measurements in Hypervelocity Flows,", Stanford UniversityEditor.

[41] Arimondo,E., Inguscio,M., and Violino,P., 1977, "Experimental Determinations of the Hyperfine Structure in the Alkali Atoms," Rev.of Mod.Phys.**, 49**(1), pp. 31-75.

[42] Metcalf,H. J., and Van der Straten,P., 1999*, Laser Cooling and Trapping*, Springer, New York, pp.40-41, 277, 284-285.

[43] Condon,E. U., and Shortley,G., 1951*, The Theory of Atomic Spectra*, University Press, Cambridge [Eng.], pp.xiv, 441.

[44] Cockerill,T., 1995"Ranque-Hilsch Vortex Tube,", Cambridge University, http://www.southstreet.freeserve.co.uk/rhvtmatl/index.htm.

[45] White,J. U., 1942, "Long Optical Path of Large Aperture," JOSA**, 32**, pp. 285-288.

[46] Pertzborn,A. J., Walewski,J. W., and Sanders,S. T., 2005, "Wavelength-Agile Source Based on a Potassium Atomic Vapor Cell and Application for Absorption Spectroscopy of Iodine," Opt.Commun.

[47] Innes,K. K., Jackling,S. J.,III, and Tolbert,T. W., 1976, "Pressure Shift and/or Broadening of Lines in the Electronic Spectra of Cl/sub 2/, Br/sub 2/, I/sub 2/, O/sub 2/, HD, AlH and H/sub 2/CO," Journal of Quantitative Spectroscopy and Radiative Transfer**, 16**(5), pp. 443-50.

[48] Gerstenkorn,S., and Luc,P., 1978*, Atlas Du Spectre d'Absorption De La Molécule d'Iode, 14800-20000 cm*$^{-1}$, Centre national de la recherche scientifique, Paris.

[49] Gerstenkorn,S., Luc,P., and, Verges,J., 1993*, Atlas Du Spectre d'Absorption De La Molécule d'Iode : 7220 cm*$^{-1}$ *- 11200 cm*$^{-1}$, Laboratoire Aimé Cotton, Orsay, France.

[50] Gerstenkorn,S., Luc,P., Verges,J., and, Chevillard,J., 1978*, Atlas Du Spectre d'Absorption De La Molécule d'Iode*, Laboratoire Aimé Cotton, Orsay, France.

[51] Walewski,J. W., and Sanders,S. T., 2005, "Pulse Shape Distortion in the Vicinity of Atomic Absorption Lines and its Impact on Time-of-Flight Spectroscopy," in preparation.

[52] Siegman,A. E., 1986*, Lasers* , University Science Books, Stanford, pp.1283.

[53] Garrett,C. G. B., and McCumber,D. E., 1970, "Propagation of a Gaussian Light Pulse through an Anomalous Dispersion Medium," Physical Review A (General Physics)**, 1**(2), pp. 305-13.

[54] Engstrom,R. W., Dr., 1980*, Photomultiplier Handbook*, RCA Corporation.

[55] Horowitz,P., and Hill,W., 1989*, The Art of Electronics*, Cambridge University Press, New York, pp.1125.

[56] Hamamatsu Photonics, 2001, "Photon Counting using Photomultiplier Tubes," .

[57] Lorosch,J., Couzi,M., Pelous,J., Vacher,R., and Levasseur,A., 1984, "BRILLOUIN AND RAMAN SCATTERING STUDY OF BORATE GLASSES," J.Non Cryst.Solids**, 69**(1), pp. 1-25.

[58] Schroeder,J., Mohr,R., Macedo,P. B., and Montrose,C. J., 1973, "Rayleigh and Brillouin Scattering in K/sub 2/O-SiO/sub 2/ Glasses," J Am Ceram Soc**, 56**(10), pp. 510-14.

[59] Wait,P. C., and Newson,T. P., 1996, "Landau Placzek Ratio Applied to Distributed Fibre Sensing," Opt.Commun.**, 122**(4-6), pp. 141-6.

[60] Karapetyan,G. O., Maksimov,L. V., and Yanush,O. V., 1990, "Physical Consequences of Inhomogeneous Glass Structure from Scattered Light Spectroscopy Data," J.Non Cryst.Solids**, 126**(1-2), pp. 93-102.

[61] Li,Yongqian, Zhang,Fucai, and Yoshino,Toshihiko, 2003, "Wide-Range Temperature Dependence of Brillouin Shift in a Dispersion-Shifted Fiber and its Annealing Effect," J.Lightwave Technol.**, 21**(7), pp. 1663-1667.

[62] Atkins,P. W., 2001*, Physical Chemistry*, Oxford University Press, Italy, pp.997.

[63] Bird,R. B., Stewart,W. E., and, Lightfoot,E. N., 2002*, Transport Phenomena*, John Wiley & Sons, New York, pp.895.

[64] Radzig,A. A., and Smirnov,B. M., 1985*, Reference Data on Atoms, Molecules, and Ions*, Springer-Verlag, 0_, pp.463.

[65] Schott Optical Glass, 2001, "SF66 923209.603," **, 2004**.

[66] Boisset,G., 2005, "Luxpop: Index of Refraction Values and Photonics Calculations," **, 2004**.

[67] Painter,L. R., Birkhoff,R. D., and Arakawa,E. T., 1969, "Optical Measurements of Liquid Water in the Vacuum Ultraviolet," J. Chem. Phys.**, 51**(1), pp. 243.

[68] Raty,J., Keranen,E., and Peiponen,K-E, 1998, "The Complex Refractive Index Measurement of Liquids by a Novel Reflectometer Apparatus for the UV-Visible Spectral Range," Meas. Sci. Technol.**, 9**, pp. 95-99.

[69] Segelstein,D., 1981""the Complex Refractive Index of Water",", University of Missouri - Kansas City, MS, http://www.philiplaven.com/p20.html.

[70] Anonymous 1997, "Release on the Refractive Index of Ordinary Water Substance as a Function of Wavelength, Temperature and Pressure," .

[71] Kolesik,M., Katona,G., Moloney,J. V., and Wright,E. M., 2003, "Theory and Simulation of Supercontinuum Generation in Transparent Bulk Media," Appl. Phys. B**, 77**, pp. 185-195.

[72] Bevington,P. R., 1969*, Data Reduction and Error Analysis for the Physical Sciences*, McGraw-Hill, Boston.

Appendix A Glossary

Anode – In an electrically conductive cell this is the negatively charged electrode. In a PMT this is the material where the electrons are collected and directed out of the dynode chain and into the circuitry of the system [62].

Cathode – In an electrically conductive cell this is the positively charged electrode. In a PMT (photocathode) this is the material which emits an electron into the dynode chain [62].

Coherent – A laser beam is coherent if all of the frequencies it contains are in phase, or in step, with each other [62].

Collimated – Light is collimated when the rays are parallel. The light neither converges nor diverges [4].

Collisional broadening – One process which can decrease the amount of time an atom spends in the excited level. Collisional decay occurs due to perturbations of the energy levels when two atoms are close enough to interact (i.e. collide). This process occurs more quickly than natural decay and dominates when there is a high number density, which is why it is also referred to as pressure broadening. It is described in Equation (A-1), in which 2γ [Hz/Pa] is the broadening coefficient, P [Pa] is the pressure, and $\Delta\nu_c$ [Hz] is the FWHM. The line shape is described by a Lorentzian equation. See also Doppler broadening, line broadening, Lorentzian profile, natural broadening [12].

$$\Delta\nu_c = 2\gamma P \tag{A-1}$$

Dipole – Two electric charges of equal but opposite strength separated by a given distance. aka: electric dipole [62].

Dipole moment – Representation of a dipole in which the vector points from the negative to the positive charge. The magnitude of the vector is the value of the charge of the electric dipole times the separation between the charges. aka: electric dipole moment [62].

Dispersion – Refers to the fact that the index of refraction is a function of frequency in any material. Only vacuum is non-dispersive [4].

Dissociation – Breaking of bonds when a molecule is exposed to energy in excess of the dissociation energy (energy required to break the bonds) for that molecule [62].

Doppler broadening – This is a form of line broadening associated with the Doppler Effect. When an atom is moving with respect to the source of light, the frequency of light it will absorb is shifted. This effect causes an uncertainty in the location of the energy level, thereby broadening the absorption spectrum. The line shape follows a Gaussian equation and the FWHM, $\Delta\nu_D$ [Hz], is defined in Equation (A-2), where ν_o [Hz] is the center frequency of the transition, T [K] is the temperature at which the interaction is occurring, and M [g/mole] is the molecular mass of the atom. The constant is a combination of several constants. See also collisional broadening, Doppler Effect, Gaussian profile, line broadening, natural broadening [12].

$$\Delta\nu_D = \nu_o 7.1623 \cdot 10^{-7} \sqrt{\frac{T}{M}} \qquad \text{(A-2)}$$

Doppler Effect – Frequency shift (Doppler shift) created by the interaction between a moving atom and light. If the atom is moving away from the source of the light then the frequency of light which it will absorb is shifted to redder frequencies. Similarly, if light

is reflected or scattered from an object moving away from the light source the reflected or scattered light will be shifted toward redder frequencies [4].

Dynode – In a PMT this is an electrode that, via secondary emission of electrons, produces current amplification [54].

Electrode – Two are present in an electrically conductive cell. They are simply metallic conductors which have opposite charges [62].

Frequency – Measure of the period of a wave (time between peaks). Measure of color with units of inverse seconds or Hz which is generally represented by f or ν. Can be converted to wavelength using Equation (A-3), in which f [Hz] is frequency, λ [m] is wavelength, and c [m/s] is the speed of light in a vacuum. See also wavenumber and wavelength.

$$f\lambda = c \tag{A-3}$$

Gaussian profile – Equation (A-4) is the Gaussian profile. In this equation, $\Delta\nu$ [Hz] is the Gaussian FWHM, ν [Hz] is a frequency, and ν_o [Hz] is the center frequency [12].

$$G = \frac{2}{\Delta\nu}\left(\frac{\ln 2}{\pi}\right)^{\frac{1}{2}} \exp\left[-4\ln 2\left(\frac{\nu-\nu_o}{\Delta\nu}\right)^2\right] \tag{A-4}$$

Group velocity – In a dispersive medium, such as an atomic vapor cell, each color travels at a different speed. The velocity of the composite disturbance created by the various frequencies can be defined by the velocity of the leading edge of the disturbance. This group velocity defines the velocity of the group of frequencies [4].

Knudsen number – Ratio of the mean free path to a characteristic length of the measurement volume. A large value indicates a diffuse or rarefied gas and is

characterized as free molecule flow; there are few interactions between molecules. A small value indicates a denser gas which can be treated as a continuum; the individual molecules do not have to be accounted for. This is the simpler case in which traditional fluid mechanics equations, such as the Navier-Stokes equations, hold true [63].

Line broadening – When a photon interacts with an atom the atom can be excited to a higher energy level. The atom will remain excited for a given period of time before relaxing to a lower energy level via several possible processes. These processes perturb the atom's energy levels; this can be pictured as the energy levels becoming "fuzzy," their locations are not exactly known. This fuzziness, or uncertainty, in the location of the energy levels is increased when the time of the transition from the excited level to a lower level is small. This uncertainty in the location of the energy levels leads to broadening of the absorption line. See also collisional broadening, Doppler broadening, natural broadening [12].

Lorentzian profile – Equation (A-5) calculates the normalized Lorentzian profile. In this equation ν [Hz] is a frequency, ν_o [Hz] is the center frequency, $\Delta\nu$ [Hz] is the FWHM of the profile [18].

$$L = \frac{1}{2\pi} \frac{\Delta\nu}{(\nu - \nu_o)^2 + \left(\frac{\Delta\nu}{2}\right)^2} \tag{A-5}$$

Mode structure – Some lasers contain multiple modes, or resonant frequencies, which combine to create the laser spectrum. An example is shown below. On a temporal axis these modes are not visible because all frequencies travel at the speed of light in a vacuum.

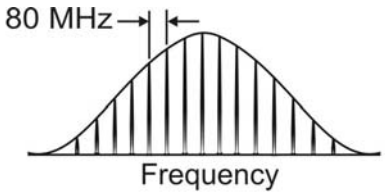

Natural broadening – The energy of an excited atom can be reduced via spontaneous emission of a photon. The amount of time required for this transition is dependent on the species and is determined by the Einstein A coefficient. This time is longer than the time for the transition to occur due to either collisional or Doppler decays, therefore, of the processes of line broadening, this one has the least impact. It is described by a Lorentzian line shape and defined in Equation (A-6). In this equation $\Delta\nu_N$ [Hz] is the FWHM, A_{ik} [s^{-1}] is the Einstein A coefficient (inverse of the time required for the spontaneous transition) for a transition from the upper state *i* to the lower state *k*, and A_{jk} [s^{-1}] is the Einstein A coefficient for a transition from the upper state *j* to the lower state *k*. The value of A_{jk} is zero if *j* is the ground state. See also collisional broadening, Doppler broadening, line broadening [12].

$$\Delta\nu_N = \frac{1}{2\pi}\left(\sum_k A_{ik} + \sum_k A_{jk}\right) \qquad \text{(A-6)}$$

Oscillating dipole – Dipole which is vibrating in a straight line [4].

Poynting vector – Mathematical representation of the flow of electromagnetic energy in a traveling wave. Assumes that the energy flows in the direction of propagation [4].

Q-switching – Method of creating a pulsed laser by modifying the resonance characteristics of the laser cavity. In general the excited state of the lasing medium is populated in a non-resonant cavity and then resonance is restored, resulting in a pulse [62].

Resonant – In a laser cavity only certain wavelengths have the right frequency to participate in the lasing process. These wavelengths are resonant with the cavity [62].

STP – Standard temperature and pressure. 298.15 K, 10^5 Pa [62].

Wavelength – Measure of the period of a wave. Measure of color in units of length such as nm. Can be converted to frequency using Equation (A-3) and to wavenumber using Equation (A-7). In this equation ν [cm^{-1}] is wavenumber and λ [nm] is wavelength.

$$\nu = \frac{10^7}{\lambda} \tag{A-7}$$

Wavenumber – Measure of the period of a wave. Measure of color in units of inverse length, cm^{-1}. It can be converted to wavelength via Equation (A-7). Equations (A-8) and (A-9) can convert differences in wavenumber, $\Delta\nu$ [cm^{-1}], to differences in frequency, Δf [GHz], or wavelength, $\Delta\lambda$ [nm].

$$\frac{\Delta\nu}{\nu} = \frac{\Delta\lambda}{\lambda} \tag{A-8}$$

$$\Delta f = 30\Delta\nu \tag{A-9}$$

Appendix B Etendue

Etendue is a measure of the collecting power of an optical system; the larger the value the more power that is collected, but the smaller the etendue the more collimated the light is (small divergence angle).

B.1 Summary of results

In this study Equation (B-1), which refers to Figure B-1, was used to calculate etendue, but other sources provide a different equation. For example, Demtröder [18] quantifies etendue by multiplying the cross sectional area by the solid angle.

$$Etendue = a_1 \sin\theta_1 = a_2 \sin\theta_2 \qquad \text{(B-1)}$$

Etendue is constant, at best, across a system but is not the same at each point in the system. For example, in Figure B-1 etendue is the same at the lens and at the focus, but it is not the same at all points in between.

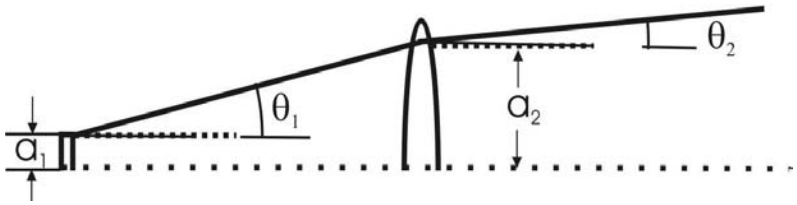

Figure B-1 Pictorial definition of etendue. Defines variables used in Equation (B-1).

In Figure B-2 the etendue is not the same at the lens, but it does have the same value at the two foci. Etendue was an important parameter in determining the optics that would be required if this measurement technique was used with a vortex tube.

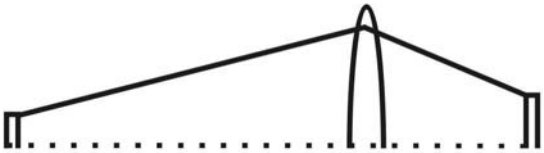

Figure B-2 The etendue has the same value at each focus, but the etendue at the lens is different.

The White-cell dimensions were initially determined based on the available mirrors; the resulting mirror diameters were 25.4 mm and 50.8 mm. The 7.62 cm diameter of the potassium AVC was based on several factors. The first was that it needed to be at least as large as the White-cell diameter if not a little larger to ensure beam passage through the cell. This effectively placed a lower limit on the cell dimension of 7.62 cm. Making the cell larger did not seem like a good option at the time because a larger cell would be more difficult to heat, build, and place on the optical table.

Assuming the above dimensions for the White-cell and the potassium AVC, the etendue of the White-cell was calculated. The size of the beam input into the cell was specified as 2 mm. The input beam diameter needed to be small in order for it to just pass the 50.8 mm mirror. The beam could be directed into the White-cell at a larger angle, i.e. further from the large mirror, but this would require a larger AVC. In order to collect the most light the small mirrors in the White-cell should be filled, but for the sake of a safety factor the dimension of the beam at the small mirrors was assumed to be 80% of the diameter of the mirror. Based on these two diameters and a 2 m baseline path length, a divergence angle of 0.0045 rad was calculated. The etendue of this cell was then 0.0000045 m; the etendue of the scattering spot had to match this value. Based on

the desired measurement resolution the scattering spot dimension was varied between 500 and 50 μm. The results of these calculations are presented in Table B-1.

Table B-1 White-cell etendue calculation. Etendue = 0.000045.

Scattering diameter (μm)	Divergence angle at scatterer (°)	Full cone angle at scatterer (°)
0.0005	1.031	2.063
0.00045	1.146	2.292
0.0004	1.289	2.579
0.00035	1.473	2.947
0.0003	1.719	3.438
0.00025	2.063	4.126
0.0002	2.579	5.158
0.00015	3.44	6.88
0.0001	5.164	10.33
0.00005	10.37	20.74

Any of these full cone angles could be measured, so no scattering spot dimension was eliminated based on practicality. However, the scattering power is proportional not only to the scattering diameter, but also to the angle in an approximately squared fashion. This means that a scattering spot of 500 μm diameter with the same etendue as a scattering spot with a 50 μm diameter will have roughly 1/10 the scattering power. It is better, therefore, to use a small scattering spot and a large cone angle.

Based on these calculations, if this experiment was performed again it would be preferable to use a larger potassium AVC and perhaps a larger White-cell. If the input beam diameter was larger than 2 mm and the divergence angle was either held constant or increased, the etendue and the power would increase. In order to increase these values the diameter of the potassium AVC would have to increase. Currently one problem with the AVC is that the windows are distorted, particularly near the edge of the cell. In order

to avoid the distortion as much as possible the AVC must be large enough so that the light can pass through the windows away from the edges. If the AVC was larger and the optical quality of the windows was improved, then a larger etendue would be possible. An increase in the input spot size would also lead to an increase in the size of the small White-cell mirrors such that the beam could have a large divergence angle. There is a limit to this, however, based on the resolution required for the measurement. Assuming a scattering half angle of 90°, which is experimentally impractical, the etendue of the scattering spot is simply the scattering spot diameter multiplied by one. If the etendue of the White-cell is large, then the scattering spot must also be large, and in some cases it may be larger than the upper resolution limit of 500 μm.

The final conclusion is that if this experiment is repeated a White-cell with a large mirror on the order of 0.1524 m should be used in conjunction with an approximately 0.2032 m diameter potassium AVC. The primary difficulties with this lie in the limitation on the scattering spot size, the difficulty in building a heater for the AVC, and the general difficulty of having a test component that large. The most important parameters in increasing etendue are increasing the input spot size while maintaining or increasing the divergence angle. In most cases this would require an increase in the diameter of the small White-cell mirrors.

One further note is that ray tracing perfomed in Zemax indicated that in the real world the etendue will get worse. In modeling the scattering from a 50 μm spot with a half angle of 10.37° in a vortex tube, the best optical setup resulted in a power loss of about 50%. The light did not focus as well at the entrance to the White-cell as

theoretically predicted and therefore the light expanded to a greater size than the small mirrors.

B.2 Text of EES (Engineering Equation Solver) code

Parameters for Potassium cell based on geometry (etendue) starting at White Cell.
Diameter of scattering spot is varied in a parametric table.

$Et = \frac{D_{scat}}{2} \cdot \sin(\theta_{scat})$ etendue based on diameter of scattering spot and collection angle

$Et = \frac{D_{spot}}{2} \cdot \sin(\theta_{spot})$ etendue at the point where the beam focuses before entering the white cell

$D_{spot,s} = 0.02$ size of beam at the small mirror based on the White cell geometry [m]

$D_{spot} = 0.002$ size of beam on large mirror, at cell inlet [m]

$\theta_{spot} = \arctan\left[\frac{D_{spot,s} - D_{spot}}{2 \cdot L_w}\right]$ angle at cell inlet [degrees]

$L_w = 2$ Length of white cell [m]

$D_{spot,l} = 2 \cdot 0.024$ Diameter of the large White cell mirror [m]

$N = \frac{D_{spot,l}}{D_{spot}}$ Number of spots that can fit on the large mirror

$\theta_{scat,full} = 2 \cdot \theta_{scat}$ full cone angle of scattering [degrees]

Appendix C Iodine Spectrum

In the course of verifying that the atomic vapor cell performed as required an iodine absorption feature was measured as described in section 5.5.2. In addition the full wavelength range of the diode laser was scanned through the iodine in order to measure the spectrum from 764.13 to 780.64 nm. The iodine cell conditions were as previously described. A 7.62 cm potassium cell was placed after the iodine cell as a frequency standard and the diode laser was scanned at a rate of 1.7 nm/s.

In Figure C-1 the iodine spectrum as measured by scanning the diode laser is shown for two different conditions. In part (a) the small 7.62 cm long potassium cell was heated so that the potassium absorption lines at 766 nm and 770 nm would be obvious. As the diode laser scans only approximately linearly and there are a large number of iodine absorption lines, these potassium absorption lines were used to locate the exact iodine feature measured in section 5.5.2. Part (b) shows the spectrum with very weak potassium absorption.

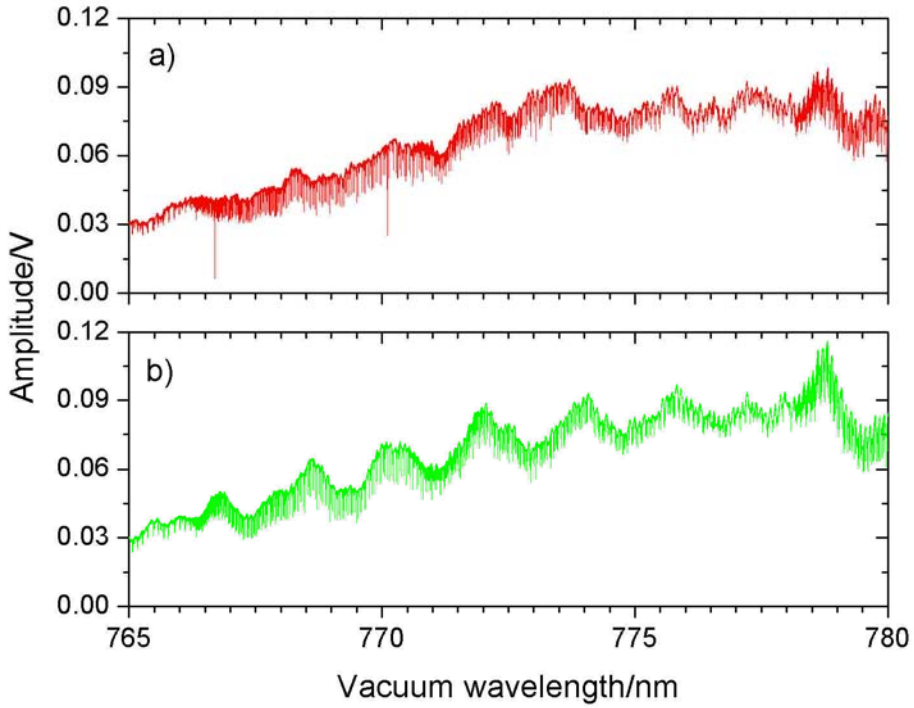

Figure C-1 Scan of iodine spectrum across approximately 16 nm. a) A potassium cell placed after the iodine cell was heated in order to locate the iodine feature of interest. The first tall downward spike is the potassium D2 absorption line near 766 nm and the second tall downward spike is the potassium D1 absorption line near 770 nm. b) The potassium cell was much cooler and the absorption lines were not obvious without magnification.

In Figure C-2 the full iodine scan across 16 nm is shown in part (c). Part (b) is created by magnifying the portion of this spectrum which contains the iodine feature of interest. Part (a) is created by further magnifying the spectrum to show only the iodine feature of interest. The top x-axis is a measure of how far the colors are from the center wavelength of the potassium line on a percentage basis. This axis serves two purposes; first, it illustrates that there are a lot of iodine absorption lines over a narrow spectral range. Second, it illustrates how narrow the iodine feature is.

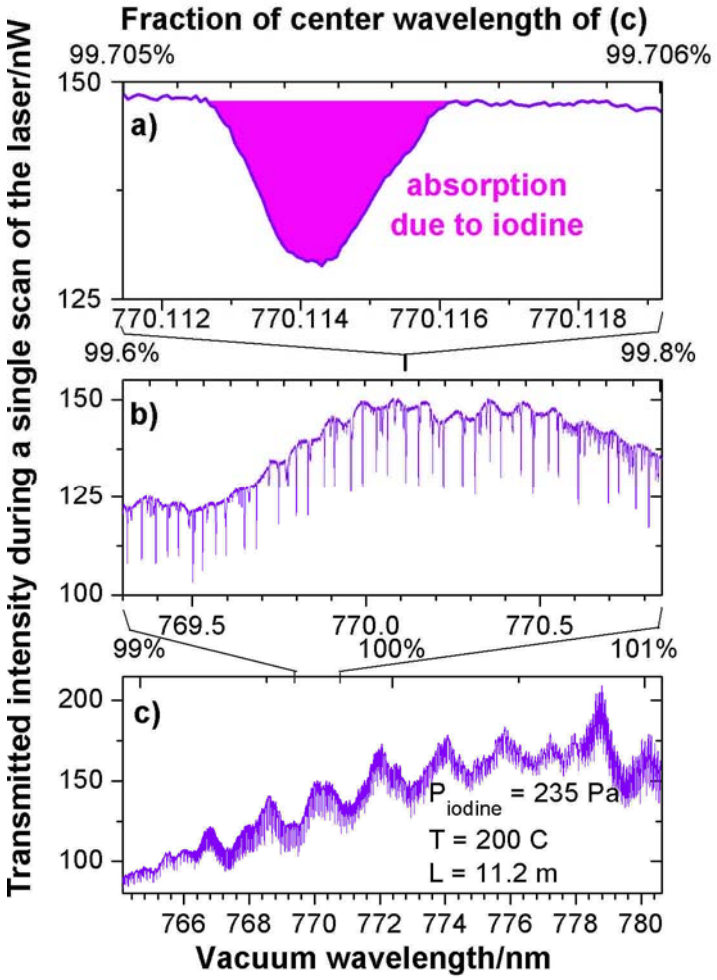

Figure C-2 Various images of the iodine absorption feature. a) Magnified iodine absorption line. b) Region of the iodine spectrum which contains the iodine feature of interest is magnified. c) The entire scan across the iodine spectrum from 764 nm to 781 nm.

Appendix D Uncertainty

The uncertainty in a given quantity can in general be calculated from the following equations, in which the measured value A is a function of experimental variables B and C as described by Equation (D-1). If more variables are present further terms can be added in order to include them.

$$A = \frac{B}{C} \tag{D-1}$$

$$u_A^2 = \left(\frac{\partial A}{\partial B}\right)^2 u_B^2 + \left(\frac{\partial A}{\partial C}\right)^2 u_C^2 \tag{D-2}$$

The variables u_A, u_B, and u_C denote the uncertainty in A, B, and C, respectively. $\partial A / \partial B$ and $\partial A / \partial C$ relate the three variables. Utilizing Equation (D-1) the derivatives can be determined and Equation (D-3) results.

$$u_A^2 = A^2 \frac{u_B^2}{B^2} + A^2 \frac{u_C^2}{C^2} \tag{D-3}$$

These equations were used as the basis of the uncertainty analyses. The following sections discuss the calculation of the uncertainty values displayed in the figures in section 5.5.2 with regard to the measurement of the iodine absorption line.

D.1 Diode laser measurements

First the uncertainty in the baseline measurements made using the diode laser was determined. The Doppler width, $\Delta\nu$ [cm^{-1}], was proportional to the square root of temperature, T [K], as indicated in Equation (D-4). It is assumed that the error in determining the location of the potassium and iodine lines, as taken from the literature, is

negligible. The value of a [$cm^{-1}/K^{1/2}$] in the equation was calculated from the constant in the equation for Doppler broadening ($7.16*10^{-7}$), Equation (A-2), multiplied by the center frequency in wavenumber and divided by the atomic mass of potassium.

$$\Delta\nu = a\sqrt{T} \tag{D-4}$$

$$a = \frac{7.16\cdot 10^{-7}}{\sqrt{39}} * 12985.17 \sim 0.00149 \tag{D-5}$$

Based on Equation (D-4) the uncertainty in the estimate of the Doppler width of potassium in Figure 5-7 was determined in Equations (D-6) to (D-8).

$$u_{\Delta\nu}^2 = \left(\frac{\partial\Delta\nu}{\partial T}\right)^2 u_T^2 \tag{D-6}$$

$$\left(\frac{\partial\Delta\nu}{\partial T}\right) = \frac{a}{2\sqrt{T}} \tag{D-7}$$

$$u_{\Delta\nu}^2 = \left(\frac{0.00149}{2\sqrt{T}}\right)^2 5^2 \sim \frac{1.39\cdot 10^{-5}}{T} \tag{D-8}$$

$u_{\Delta\nu}$ [cm^{-1}] is the uncertainty in the Doppler width measurement and the error in the temperature measurement, u_T, is estimated as 5 K.

It was assumed that in Figure 5-7 the Doppler width of potassium at room temperature was measured. Therefore, the number of data points which were equivalent to the FWHM was estimated and a ratio of wavenumber to data points was calculated in order to convert the x-axis to frequency. There was an error associated with this scale factor (*sf*) due to the combined error in the measurement of the Doppler width and the counting of data points (i.e. which data point was at the FWHM). The following equations were used to calculate the *sf* error, u_{sf} [cm^{-1}/point].

$$sf = \frac{\Delta\nu}{div} \tag{D-9}$$

$$u_{sf}^2 = \left(\frac{\partial sf}{\partial \Delta\nu}\right)^2 u_{\Delta\nu}^2 + \left(\frac{\partial sf}{\partial div}\right)^2 u_{div}^2 \tag{D-10}$$

Where *div* [point] represents the number of data points which equal $\Delta\nu$ [cm^{-1}]. $u_{\Delta\nu}$ and u_{div} [point] are the errors in the Doppler width measurement, as given above, and the error in determining the data points which represent the Doppler width, respectively. In this case u_{div} is estimated as 2.82, assuming that each of the two values for the FWHM is in error by ±2 points. Equation (D-12) is based on Equation (D-3).

$$u_{div} \sim \sqrt{2^2 + 2^2} \tag{D-11}$$

$$u_{sf}^2 = sf^2 \frac{u_{\Delta\nu}^2}{\Delta\nu^2} + sf^2 \frac{u_{div}^2}{div^2} \tag{D-12}$$

D.2 AVC scan measurements

Estimates in the uncertainty of the atomic vapor cell measurements were also made. First the uncertainty in the calculation of absorbance using Beer's law was estimated.

$$\alpha = -\ln\frac{I}{I_o} \tag{D-13}$$

α is the absorbance, I is the measurement after the potassium and iodine cells and I_o is the measurement after the potassium cell only.

$$u_\alpha^2 = \left(\frac{\partial \alpha}{\partial I}\right)^2 u_I^2 + \left(\frac{\partial \alpha}{\partial I_o}\right)^2 u_{Io}^2 \tag{D-14}$$

$$\frac{\partial \alpha}{\partial I} = -\frac{1}{I} \tag{D-15}$$

$$\frac{\partial \alpha}{\partial I_o} = \frac{1}{I_o} \tag{D-16}$$

$$u_\alpha^2 = \frac{1}{I^2} u_I^2 + \frac{1}{I_o^2} u_{Io}^2 \tag{D-17}$$

Based on the noise in the measured I and I_o spectra at the location of the iodine line, the uncertainties u_I [cm^{-1}] and u_{Io} [cm^{-1}] were estimated as 0.35% of I and I_o, respectively. u_α [cm^{-1}] is the uncertainty in absorbance introduced by Beer's law.

There were further sources of error in the measurement of the FWHM of the iodine absorption spectrum. The data were based on 1000 averages and it was estimated that the jitter was ±50 ps. This resulted in an error in the temporal measurement, u_t, of 50 ps divided by the square root of 1000 averages, or 0.00158 ns. The error in color due to jitter was determined by calculating the excess delay time associated with the two colors at the FWHM using Figure 5-6, (b). The maximum value for the FWHM was estimated by subtracting 0.00158 ns from the lower excess delay time and adding it to the higher time; these excess delays were then converted back to frequency using Figure 5-6, (b) and a maximum spectral FWHM was calculated. The minimum spectral FWHM was calculated in the same manner, except 0.00158 ns was added to the minimum delay time and subtracted from the maximum delay time. The difference between the maximum and minimum value of the FWHM resulted in the uncertainty due to jitter. Finally, there was once again an error associated with the selection of the data points which represent the

FWHM. Once all three of these error sources were summed in quadrature a final uncertainty of approximately 0.0004 cm^{-1} was calculated.

Appendix E HFS Matlab Code

This appendix contains the Matlab code used to calculate the relative strengths and positions of the hyperfine lines. The relative strength is valid only within a given line; for example, the relative strength of each hyperfine line of the D1 transition is only relative to the D1 line, it is not relative to the D2 line. The relative position is with respect to the quoted line center in the literature. When multiple isotopes are present they are accounted for in the calculations. The equations at the end of the code calculate the actual shape of each hyperfine line, sum the shapes together, and result in a final composite line. The locations and relative strengths of the lithium, sodium, potassium, rubidium, and cesium D1 and D2 transitions are shown in the figures in section E.2. The constants were found in the references [42, 64].

E.1 Hyperfine splitting calculations

E.1.1 Main code

```
clc
clear all
close all

%This program calculates hyperfine splitting
%Created 11-17-04
%References (in no particular order)
% Condon, E.U. and G. Shortley, The theory of atomic spectra. 1951,
Cambridge [Eng.]: University Press. xiv, 441.
    %strength equations
% Wehe, S.D., Development of a tunable diode laser probe for
measurements in hypervelocity flows, in Mechanical Engineering. 2000,
Stanford University: Stanford, CA. p. 186.
    %PhD thesis, strength equations, general theory
% Haag, H.W., et al., Discussion of dispersion relations in atomic
spectra with respect to experimental demonstration. Eur. J. Phys.,
1999. 20: p. 221-229.
    %Rubidium data used for comparison
% Metcalf, H.J. and P. Van der Straten, Laser cooling and trapping.
Graduate texts in contemporary physics. 1999, New York: Springer. 40-
41, 277, 284-285.
```

```
    %constants in calculations such as A, B, I, J, F,...
    %Used appendix D to verify strength calculations
% Radzig, A.A. and B.M. Smirnov, Reference data on atoms, molecules,
and ions. Springer series in chemical physics ; 31. 1985, Berlin ; New
York: Springer-Verlag. xi, 463.
    %isotope shift data as well as some duplication of data in Metcalf.
    %Probably best all around resource for constants
% Arimondo, E., M. Inguscio, and P. Violino, Experimental
determinations of the hyperfine structure in the alkali atoms. Rev. of
Mod. Phys., 1977. 49(1): p. 31-75.
    %relative location equation (DeltaE in this paper)
%Fricke-Begemann, C., Lidar investigations of the mesopause region:
temperature structure and variability, in Mathematics. 2004,
Universitat Rostock: Kuhlungsborn, Germany. p. 147
    %Verification of potassium calculations


%Constants for each element

%Enter the data in the same format that is shown.  This code was
written for alkali metals, so it assumes
%D1 and D2 lines.  If a different substance is used, the variables
Fe_d2_1,
%... should be set as empty matrices.  If only one isotope is used, set
the
%Fe_d2_2, ... variables as empty matrices.

%number of isotopes
iso=2;

%Reported line center cm-1 [D1,D2]
K_c=[12985.17,13042.88];    %enter the data as a row vector

%isotope shift in MHz [39K,41K]
K_shift=[0,660-425];    %enter the data as a row vector, each column is
an isotope

%Total angular momentum of the electron in the ground state
Jg=1/2; %There is only one ground state

%Total angular momentum of the ground state atom, I+J, [39K; 41K]
Fg=[1 2; 1 2];  %There is only one ground state

%Constant parameter for ground state in MHz [39K,41K]
Ag=[230.859,127.007];  %There is only one ground state

%Each Fe is for the excited state for each isotope.  Fe_d1_1 is the
excited
%state of the first isotope, Fe_d1_2 is for the second isotope.
Fe_d1_3 is
%for the third isotope, which in this case is zero.  The data are input
as
%J (total angular momentum of the electron), I (nuclear spin), isotopic
```

```
%abundance in %, value of A constant in MHz, value of B constant in MHz
%(zero for J less than 3/2), and then the F values, where F is the
total
%angular momentum of the atom

Fe_d1_1=[1/2 3/2 93.26 28.85 0 1 2];
Fe_d1_2=[1/2 3/2 6.73 15.2 0 1 2];    %enter as a row vector for each
isotope (i.e. one row per isotope)
Fe_d1_3=[];

%These variables are similar to those above, but they represent a
second line.  in the case of
%alkali metals, this is the D2 line.  The data are input as
%J (total angular momentum of the electron), I (nuclear spin), isotopic
%abundance in %, value of A constant in MHz, value of B constant in MHz
%(zero for J less than 3/2), and then the F values, where F is the
total
%angular momentum of the atom
Fe_d2_1=[3/2 3/2 93.26 6.06 2.83 0 1 2 3];
Fe_d2_2=[3/2 3/2 6.73 3.4 3.34 0 1 2 3]; %enter as a row vector for
each isotope (i.e. one row per isotope)
Fe_d2_3=[];

%If you want to calculate the actual lineshape of the absorption line,
%enter values for the following constants.  If you don't want to do
this
%calculation, which can take half an hour, enter 0 for A1.  These
values
%are for the first line.  Enter additional values for the second line
if
%desired.
PPa1= .004789;       %vapor pressure in Pa
T1= 374;         %corresponding temperature in K
A1= 3.802e7;         %Einstein A coefficient in rad/s
f1=.338;          %oscillator strength for the overall transition (the
value for each hyperfine line will be determined)
Pbroad1=3e3*10*1e6/133.322;     %The pressure broadening coefficient in
Hz/Pa
M1=39.1;          %Molecular weight in amu

%Input these data only if you want to calculate the lineshapes for a
second
%set of hyperfine lines
PPa2= .0135;       %vapor pressure in Pa
T2= 390;         %corresponding temperature in K
A2= 0;         %Einstein A coefficient in rad/s
f2=.338;          %oscillator strength for the overall transition (the
value for each hyperfine line will be determined)
Pbroad2=3e3*10*1e6/133.322;     %The pressure broadening coefficient in
Hz/Pa
M2=39.1;         %Molecular weight in amu
```

```
%The following sections calculate the locations and relative strengths
of
%each hyperfine line utilizing three functions.  the first portion of
each
%if statement is a check to verify that the line exists (i.e. not an
empty
%matrix)

if sum(Fe_d1_1)==0
    Fd1_1=[];
    stored1_1=[];
    Dnu1_1=[];
else
    Fd1_1=HFS_Fdiff(Fe_d1_1, Fg(1,:));  %Calculates difference between
ground and excited F states
    DFd1_1=Fd1_1(:,1);  %This is the vector of differences
    Fd1_1(:,1)=[];
    stored1_1=HFS_strength(Fd1_1, Jg);  %determine the relative
strength of each line
    Dnu1_1=HFS_location(Fe_d1_1, Fg(1,:), Ag(1,1), Jg, K_shift(1,1),
K_c(1,1)); %determine location of each hyperfine line
    [r1,c1]=find(DFd1_1(:,1)==-1|DFd1_1(:,1)==1|DFd1_1(:,1)==0);
%find where the selection rules are broken, the difference between the
F values can only be -1,0,1
    stored1_1=stored1_1(r1(1:end),:);   %removes data that violates the
selection rules

stored1_1=stored1_1(:,end)./sum(stored1_1(:,end)).*stored1_1(:,3)/100;
%scales relative strength based on isotopic abundance
    Dnu1_1=Dnu1_1(r1(1:end),:); %removes data that violates the
selection rules
end

if sum(Fe_d1_2)==0
    Fd1_2=[];
    stored1_2=[];
    Dnu1_2=[];
else
    Fd1_2=HFS_Fdiff(Fe_d1_2, Fg(2,:));
    DFd1_2=Fd1_2(:,1);
    Fd1_2(:,1)=[];
    stored1_2=HFS_strength(Fd1_2, Jg);
    Dnu1_2=HFS_location(Fe_d1_2, Fg(2,:), Ag(1,2), Jg,
K_shift(1,2),K_c(1,1));
    [r1,c1]=find(DFd1_2(:,1)==-1|DFd1_2(:,1)==1|DFd1_2(:,1)==0);
%find where the selection rules are broken
    stored1_2=stored1_2(r1(1:end),:);

stored1_2=stored1_2(:,end)./sum(stored1_2(:,end)).*stored1_2(:,3)/100;
    Dnu1_2=Dnu1_2(r1(1:end),:);
end

if sum(Fe_d1_3)==0
    Fd1_3=[];
    stored1_3=[];
```

```
    Dnu1_3=[];
else
    Fd1_3=HFS_Fdiff(Fe_d1_3, Fg(3,:));
    DFd1_3=Fd1_3(:,1);
    Fd1_3(:,1)=[];
    stored1_3=HFS_strength(Fd1_3, Jg);
    Dnu1_3=HFS_location(Fe_d1_3, Fg(3,:), Ag(1,3), Jg,
K_shift(1,3),K_c(1,1));
    [r1,c1]=find(DFd1_3(:,1)==-1|DFd1_3(:,1)==1|DFd1_3(:,1)==0);
%find where the selection rules are broken
    stored1_3=stored1_3(r1(1:end),:);
    stored1_3=stored1_3(r1(1:end),:);

stored1_3=stored1_3(:,end)./sum(stored1_3(:,end)).*stored1_3(:,3)/100;
    Dnu1_3=Dnu1_3(r1(1:end),:);
end

if sum(Fe_d2_1)==0
    Fd2_1=[];
    stored2_1=[];
    Dnu2_1=[];
else
    Fd2_1=HFS_Fdiff(Fe_d2_1, Fg(1,:));
    DFd2_1=Fd2_1(:,1);
    Fd2_1(:,1)=[];
    stored2_1=HFS_strength(Fd2_1, Jg);
    Dnu2_1=HFS_location(Fe_d2_1, Fg(1,:), Ag(1,1), Jg,
K_shift(1,1),K_c(1,2));
    [r1,c1]=find(DFd2_1(:,1)==-1|DFd2_1(:,1)==1|DFd2_1(:,1)==0);
%find where the selection rules are broken
    stored2_1=stored2_1(r1(1:end),:);

stored2_1=stored2_1(:,end)./sum(stored2_1(:,end)).*stored2_1(:,3)/100;
    Dnu2_1=Dnu2_1(r1(1:end),:);
end

if sum(Fe_d2_2)==0
    Fd2_2=[];
    stored2_2=[];
    Dnu2_2=[];
else
    Fd2_2=HFS_Fdiff(Fe_d2_2, Fg(2,:));
    DFd2_2=Fd2_2(:,1);
    Fd2_2(:,1)=[];
    stored2_2=HFS_strength(Fd2_2, Jg);
    Dnu2_2=HFS_location(Fe_d2_2, Fg(2,:), Ag(1,2), Jg,
K_shift(1,2),K_c(1,2));
    [r1,c1]=find(DFd2_2(:,1)==-1|DFd2_2(:,1)==1|DFd2_2(:,1)==0);
%find where the selection rules are broken
    stored2_2=stored2_2(r1(1:end),:);

stored2_2=stored2_2(:,end)./sum(stored2_2(:,end)).*stored2_2(:,3)/100;
    Dnu2_2=Dnu2_2(r1(1:end),:);
end
```

```
if sum(Fe_d2_3)==0
    Fd2_3=[];
    stored2_3=[];
    Dnu2_3=[];
else
    Fd2_3=HFS_Fdiff(Fe_d2_3, Fg(3,:));
    DFd2_3=Fd2_3(:,1);
    Fd2_3(:,1)=[];
    stored2_3=HFS_strength(Fd2_3, Jg);
    Dnu2_3=HFS_location(Fe_d2_3, Fg(3,:), Ag(1,3), Jg,
K_shift(1,3),K_c(1,2));
    [r1,c1]=find(DFd2_3(:,1)==-1|DFd2_3(:,1)==1|DFd2_3(:,1)==0);
%find where the selection rules are broken
    stored2_3=stored2_3(r1(1:end),:);

stored2_3=stored2_3(:,end)./sum(stored2_3(:,end)).*stored2_3(:,3)/100;
    Dnu2_3=Dnu2_3(r1(1:end),:);
end

%Create a vector of all data
s=[stored1_1;stored1_2; stored1_3];
l=[Dnu1_1; Dnu1_2; Dnu1_3];
s2=[stored2_1; stored2_2; stored2_3];
l2=[Dnu2_1; Dnu2_2; Dnu2_3];

%Create figures of the data
figure
bar( l(:, 1),s)
title('Position of hyperfine lines relative to line center')
xlabel('Relative frequency [MHz]')
ylabel('relative strength')
figure
bar( l(:, 2),s)
title('Position of hyperfine lines')
xlabel('Frequency [cm-1]')
ylabel('relative strength')

figure
bar( l2(:, 1),s2)
title('Position of hyperfine lines relative to line center')
xlabel('Relative frequency [MHz]')
ylabel('relative strength')
figure
bar( l2(:, 2),s2)
title('Position of hyperfine lines')
xlabel('Frequency [cm-1]')
ylabel('relative strength')
break
%Calculate the lineshapes of each hyperfine line and sums them together
to
%form one line.  In this case the absorbance and delay are based on a
path length of
%100m.  These values can be scaled for other lengths by multiplying by
the
%desired length/100.
```

```
if A1==0
    A1=0;
else
    shape=lineshape(s',l(:,1)'.*1e6*2*pi,PPa1, T1, K_c(1,1), A1, f1,
Pbroad1,M1);
    wvect=shape(1,:);   %frequency vector in rad/s
    fvect=wvect/2/pi;   %frequency vector in Hz
    wavenumber=fvect./30e9; %frequency vector in cm-1
    nminus1=shape(2,:); %index of refraction minus 1
    wvectdelay=wvect(2:end);    %The following lines adjust the length
of the frequency vectors to account for the shorter delay vector, which
is based on a differential
    fdelay=fvect(2:end);
    wdelay=wavenumber(2:end);
    tdelay=shape(3,2:end);  %delay time in ns due to passage through a
100m long cell
    kappa=shape(4,:);   %extinction coefficient
    kL=shape(5,:);  %alpha, the absorbance
    k=shape(6,:);   %absorption coefficient in cm-1
    halfxvect=shape(7,:);   %1/2 times the complex susceptibility
    figure
    plot(wdelay, tdelay)
    title('Delay time after light passes through 100m of the
substance')
    xlabel('frequency [cm-1]')
    ylabel('delay [ns]')
    figure
    semilogy(wavenumber, kL)
    title('Absorbance after light passes through 100m of the
substance')
    xlabel('frequency [cm-1]')
    ylabel('Absorbance')

end

if A2==0
    A2=0;
else
    shape2=lineshape(s2',l2(:,1)'.*1e6*2*pi,PPa2, T2, K_c(1,2), A2, f2,
Pbroad2,M2);
    wvect2=shape2(1,:);   %frequency vector in rad/s
    fvect2=wvect2/2/pi;   %frequency vector in Hz
    wavenumber2=fvect2./30e9; %frequency vector in cm-1
    nminus12=shape2(2,:); %index of refraction minus 1
    wvectdelay2=wvect2(2:end);    %The following lines adjust the
length of the frequency vectors to account for the shorter delay
vector, which is based on a differential
    fdelay2=fvect2(2:end);
    wdelay2=wavenumber2(2:end);
    tdelay2=shape2(3,2:end);  %delay time in ns due to passage through
a 100m long cell
    kappa2=shape2(4,:);   %extinction coefficient
    kL2=shape2(5,:);  %alpha, the absorbance
    k2=shape2(6,:);   %absorption coefficient in cm-1
    halfxvect2=shape2(7,:);   %1/2 times the complex susceptibility
```

```
    figure
    plot(wdelay2, tdelay2)
    title('Delay time after light passes through 100m of the
substance')
    xlabel('frequency [cm-1]')
    ylabel('delay [ns]')
    figure
    semilogy(wavenumber2, kL2)
    title('Absorbance after light passes through 100m of the
substance')
    xlabel('frequency [cm-1]')
    ylabel('Absorbance')
end

% Constants for Rb
% iso=2;
% K_c=[12578.95,12816.55];    %cm-1 enter the data as a row vector
% K_shift=[0,80];    % MHz enter the data as a row vector, each column
is an isotope
% Jg=1/2; %There is only one ground state
% Fg=[2 3;1 2];  %There is only one ground state
% Ag=[1011.91 3417.341];  %There is only one ground state
% Fe_d1_3=[];
% Fe_d1_1=[1/2 5/2 72.17 120.72 0 2 3];
% Fe_d1_2=[1/2 3/2 27.83 406.2 0 1 2];    %enter as a row vector for
each isotope (i.e. one row per isotope)
% Fe_d2_3=[];
% Fe_d2_1=[3/2 5/2 72.17 25.009 25.88 1 2 3 4];
% Fe_d2_2=[3/2 3/2 27.83 84.845 12.52 0 1 2 3]; %enter as a row vector
for each isotope (i.e. one row per isotope)

% Constants for Li
% iso=2;
% K_c=[14903.7 14904];    %cm-1 enter the data as a row vector
% K_shift=[0,18070-7540];    % MHz enter the data as a row vector, each
column is an isotope
% Jg=1/2; %There is only one ground state
% Fg=[1/2 3/2;1 2];  %There is only one ground state
% Ag=[152.137 401.752];  %There is only one ground state
% Fe_d1_3=[];
% Fe_d1_1=[1/2 1 7.5 17.375 0 1/2 3/2];
% Fe_d1_2=[1/2 3/2 92.5 45.914 0 1 2];    %enter as a row vector for
each isotope (i.e. one row per isotope)
% Fe_d2_3=[];
% Fe_d2_1=[3/2 1 7.5 -1.155 -.1 1/2 3/2 5/2];
% Fe_d2_2=[3/2 3/2 92.5 -3.055 -.221 0 1 2 3]; %enter as a row vector
for each isotope (i.e. one row per isotope)

% Constants for Cs
% iso=1;
% K_c=[11178.27 11732.31];    %cm-1 enter the data as a row vector
% K_shift=[0,0];    % MHz enter the data as a row vector, each column
is an isotope
% Jg=1/2; %There is only one ground state
% Fg=[3 4;0 0];  %There is only one ground state
```

```
% Ag=[2298.157 0];  %There is only one ground state
% Fe_d1_3=[];
% Fe_d1_1=[1/2 7/2 100 291.9 0 3 4];
% Fe_d1_2=[];    %enter as a row vector for each isotope (i.e. one row
per isotope)
% Fe_d2_3=[];
% Fe_d2_1=[3/2 7/2 100 50.34 -.38 2 3 4 5];
% Fe_d2_2=[]; %enter as a row vector for each isotope (i.e. one row per
isotope)

% Constants for Na
% iso=1;
% K_c=[16956.17 16973.37];    %cm-1 enter the data as a row vector
% K_shift=[0,0];    % MHz enter the data as a row vector, each column
is an isotope
% Jg=1/2; %There is only one ground state
% Fg=[1 2;0 0];  %There is only one ground state
% Ag=[885.813 0];  %There is only one ground state
% Fe_d1_3=[];
% Fe_d1_1=[1/2 3/2 100 94.3 0 1 2];
% Fe_d1_2=[];    %enter as a row vector for each isotope (i.e. one row
per isotope)
% Fe_d2_3=[];
% Fe_d2_1=[3/2 3/2 100 18.69 2.9 0 1 2 3];
% Fe_d2_2=[]; %enter as a row vector for each isotope (i.e. one row per
isotope)
```

E.1.2 Subfunctions

```
function a=HFS_Fdiff(F,Fg)

%Here the calculation of the difference between the F values in the
ground
%and excited states is made.

DF=[];  %variable in which the difference values are stored
Fd1=[];
for rindex1=1:size(F,1) %base index on number of rows in excited d1 F
matrix, each row is for a different isotope
    for index=1:size(Fg,2)  %base index on number of columns in ground
state F matrix
        F1=Fg(rindex1,index);     %select a value in the ground matrix.
there is only one row, so this step selects a corresponding column
        for index1=6:size(F,2) %base index on columns in  F matrix
            F2=F(rindex1,index1);   %select a value in the F matrix
            DF1=F2-F1;  %calculate the difference between the excited
and ground state F values
            DF=[DF; DF1];   %store the difference between the excited
and ground state F values
            Fd1=[Fd1; F(rindex1, 1:5) F1 F2]; %store the excited and
ground state F values, ground state in column 1
        end
```

```
    end
end
Fd1=[DF Fd1] ;  %put the difference values into the F values matrix
a=Fd1;



function a=HFS_location(F, Fg1, Ag, Jg, K_shift, K_c)

%Here the location of each line is calculated.  The formula for the
location varies.  If the excited J is less
%than 3/2, as in the case of the potassium D1 line, then a shorter
equation
%is used because the value of the B constant is 0. The values are in
MHz.

dnug1=[];
dnue1=[];

%These first steps only calculate the relative location with respect to
the
%energy level (i.e. ground state and excited state)
for index2=1:size(Fg1,1) %calculate relative locations of the ground
state.  These values are based on the ground state being at 0.
        kappa=Fg1(index2,:).*(Fg1(index2,:)+1)-F(1,2).*(F(1,2)+1)-
Jg*(Jg+1); %used in calculation
        dnug=1/2*Ag(1,index2).*kappa;
        dnug1=[dnug1; dnug];
end
if F(1,1)<3/2 & F(1,1)>0        %These steps are taken for J<3/2
        kappae=F(1, 6:end).*(F(1, 6:end)+1)-F(1,2).*(F(1,2)+1)-
F(1,1)*(F(1,1)+1); %used in calculation
        dnue=1/2*F(1,4).*kappae;
        dnue1=[dnue1; dnue];
elseif F(1,1)>=3/2       %These steps are taken for J>=3/2
        kappae1=F(1,6:end).*(F(1,6:end)+1)-F(1,2).*(F(1,2)+1)-
F(1,1)*(F(1,1)+1); %used in calculation
        dnue=1/2*F(1,4).*kappae1+F(1,5).*(3/2.*kappae1.*(kappae1+1)-
2*F(1,2)*(F(1,2)+1)*F(1,1)*(F(1,1)+1))./(2*F(1,2)*(2*F(1,2)-
1)*2*F(1,1)*(2*F(1,1)-1));
        dnue1=[dnue1; dnue];
else grr=0;
end

Dnu1=[];
%These steps calculate the relative locations with respect to the
ground
%state energy level.  The value of the isotope shift is included.
These
%values are in MHz.
for index=1:size(dnug1,1)
    for index1=1:size(dnug1,2)
        nug=dnug1(index, index1);
        for index2=1:size(dnue1, 2)
```

```
        nue=dnue1(1, index2);
        Dnu=nue-nug+K_shift;
        Dnu1=[Dnu1; Dnu];
        end
    end
end
Dnucm=Dnu1*1e6/30e9+K_c;    %The absolute location with respect to the
measured line center is calculated in cm-1 (1Hz/30e9cm-1)
a=[Dnu1, Dnucm];



function a=HFS_strength(F,Jg)

%Calculate the relative strength of each line
%First, I need to know which set of equations to use.  This is
determined
%by the variation in the J value from the ground to excited state.
With D1
%and D2 lines, the D1 line is J to J and the D2 line is J-1 to J.

store=[];

for index=1:size(F,1)  %base index on columns in excited J vector, only
one row
    if Jg==F(index,1)   %J=J case, from Condon and Shortley
            if F(index, 6)-F(index, 7)==-1    %the if statements choose
the correct equation based on the selection rules for DeltaF
              one=(F(index, 6)-F(index,2)+F(index,1)+1).*(F(index,
6)+F(index,2)-F(index,1)+1).*(F(index,2)+F(index,1)+F(index,
6)+2).*(F(index,2)+F(index,1)-F(index, 6))./(4*(F(index, 6)+1));
          elseif F(index, 6)-F(index, 7)==0
              one=(2*F(index, 6)+1)./(4*F(index, 6).*(F(index,
6)+1))*(F(index, 6)*(F(index, 6)+1)-
F(index,2).*(F(index,2)+1)+F(index,1)*(F(index,1)+1)).^2;
          else F(index, 6)-F(index, 7)==1
              one=(F(index, 6)-F(index,2)+F(index,1)).*(F(index,
6)+F(index,2)-F(index,1)).*(F(index,2)+F(index,1)+F(index,
6)+1).*(F(index,2)+F(index,1)+1-F(index, 6))./(4*F(index, 6));
            end
           store=[store;F(index,1:5) one] ; %store the results
    elseif Jg==F(index,1)-1  %J-1=J case, from Shawn Wehe's thesis
            if F(index,7)-F(index,6)==1

two=(F(index,1)+F(index,7)+F(index,2)+1).*(F(index,1)+F(index,7)+F(inde
x,2)).*(F(index,1)+F(index,7)-F(index,2)).*(F(index,1)+F(index,7)-
F(index,2)-1)./(F(index,7)) ;
            elseif F(index,7)-F(index,6)==0
                two=-
(F(index,1)+F(index,7)+F(index,2)+1).*(F(index,1)+F(index,7)-
F(index,2)).*(F(index,1)-F(index,7)+F(index,2)).*(F(index,1)-
F(index,7)-F(index,2)-
1).*(2*F(index,7)+1)./(F(index,7)*(F(index,7)+1));
            else F(index,7)-F(index,6)==-1
```

```
                two=(F(index,1)-F(index,7)+F(index,2)).*(F(index,1)-
F(index,7)+F(index,2)-1).*(F(index,1)-F(index,7)-F(index,2)-
1).*(F(index,1)-F(index,7)-F(index,2)-2)./(F(index,7)+1);
            end
            store=[store;F(index,1:5) two];
    else grr=0;
    end
end

a=store;



function a=lineshape(HFSamp, HFStrans, PPa, T, K_c, A, ftot, twogam, M)

format long e
%Modified 11-29-04
%equations based on Demtröder, W., Laser spectroscopy : basic concepts
and instrumentation. 3rd ed. Advanced texts in physics,. 2003, Berlin ;
New York: Springer. 65-69, 77, 655.
%Some data from Kurucz, R.L.B., B., Atomic Line Data. 1995, Smithsonian
Astrophysical Observatory: Cambridge, MA.
lam = 1/(K_c*100); %m, wavelength
f=ftot.*HFSamp;         %oscillator strength for each hyperfine line

%plotting inputs:
startaway = 10; %Ghz, frequency ranges from +/- startaway
pts = 3000 ; %Number of data points evaluated

L = 100;%m, length of cell
c = 3e8; %m/s, speed of light in a vacuum
Patm = PPa/101325; %atm
n = PPa/1.38e-23/T; %m^-3
wao = c/lam*2*pi+HFStrans;   %lambda converted to frequency in rad/s,
this is the center frequency for each hyperfine line
waolam = c/lam*2*pi;    %lambda converted to frequency in rad/s, this
is the center frequency for the composite line
delwL =(twogam*PPa*2*pi+A) ;  %homogeneous broadening due to pressure
broadening and natural broadening, want natural broadening greater than
pressure broadening
delwD = 7.17e-7*wao*sqrt(T/M) ;  %Doppler width, inhomogenous
broadening effect, want this larger than delwL

q=1.6e-19;  %[C] charge of an electron
eo=8.854e-12;    %[C2/N-m2] permittivity of free space
me=9.11e-31;     %[kg] mass of an electron
kb=1.38e-23;     %boltzman constant [J/K]
vp=sqrt(2*kb*T/M*6.026e26); %most probable velocity in m/s
halfchiconst= f.*c*n*q^2/vp/sqrt(pi)/2/eo/me./wao; %based on Demtroder,
this is the constant part of half of the susceptibility

limw1 = waolam-startaway*1e9*2*pi;  %Sets relative frequency for low
end (most negative)
```

```
wstep = (waolam-limw1)/pts*2 ;  %sets step size

%Set empty matrices that the data will be saved into
Nminus1=[];
Tdelay=[];
Kappa=[];
KL=[];
K=[];
geninttot=[];
Fvect=[];
Nuvect=[];
Fvectshort=[];
Xvect=[];
Wvect=[];
Wao=[];
zz=0;

while zz<length(HFSamp)
h=waitbar(0,'Calculating lineshape, please wait ...');
wvect = []; %frequency vector in rad/s
xvect = []; %susceptibility vector
w = limw1; %sets first value of frequency vector
lim1 = wao(:,zz+1)-5*delwD(:,zz+1); %Sets range of frequency values
lim2 = wao(:,zz+1)+5*delwD(:,zz+1);
step = min(delwL,delwD(:,zz+1))/100; %sets the step size
wa = lim1:step:lim2; %vector, wa is atomic transition frequency
for loop = 1:1:pts
    waitbar(loop/pts)
    w = w + wstep;
    term = c*(wa-wao(:,zz+1))./wao(:,zz+1)./vp; %vector, used as
shorthand
    y = 1./(wa.^2-w.^2+i*delwL*w).*exp(-term.^2); %vector, part of the
complex suspceptibility that is integrated
    genint = sum(y)*step;   %integral of part of complex susceptibility
    halfchi = halfchiconst(:,zz+1)*genint;  %half of the total complex
susceptibility
    wvect = [wvect,w];  %frequency vector in rad/s
    xvect = [xvect,halfchi];  %complex susceptibility
end
    Xvect=[Xvect;xvect];    %contains susceptibility for each hyperfine
line
    geninttot=[geninttot;genint];
    nrefract=real(xvect)+1;    %calculates index of refraction.
1+1/2chi
    nminus1=nrefract-1;     %calculates index of refraction minus 1
    kappa=-imag(xvect);%calculates the extinction coefficient, -1/2chi
    dndw=diff(nrefract)./diff(wvect);   %calculates change in index of
refraction with frequency in rad/s, Yalin, Barker and Miles
    wvectshort=wvect(2:end);    %in calculating dndw I lose a data
point, so I need to shorten the vectors
    nrefractshort=nrefract(2:end); %in calculating dndw I lose a data
point, so I need to shorten the vectors
    Vg=c./(nrefractshort+wvectshort.*dndw);   %calculates the GVD
    tdelay=(L./Vg-L/c).*1e9;   %calculates the delay time in ns
```

```
    lamall=2*pi*c./wao(zz+1);    %calculates center wavelength for each
hyperfine line
    %lamall=lam;             %center wavelength for composite line
    propagation=2*pi/(lamall); %m-1 propagation number, weird constant
in spectroscopy, usually cm-1
    kL=2.*kappa*propagation.*L; %absorbance
    k=2*kappa*propagation/100;  %cm-1
    Trans=exp(-kL);  %transmission
    fvect = (wvect-waolam)/2/pi/1e9; %GHz converts from rad/s to GHz
    nuvect = fvect/30; %cm-1    converts from GHz to wavenumber
    fvectshort=fvect(2:end);    %in calculating dndw I lose a data
point, so I need to shorten the vectors
    Nminus1=[Nminus1; nminus1];
    Tdelay=[Tdelay; tdelay];
    Kappa=[Kappa;kappa];
    KL=[KL;kL];
    K=[K;k];
    Nuvect=[Nuvect; nuvect];
    Wvect=[Wvect; wvect];
    zz=zz+1
    Fvect=[Fvect; fvect];
    close(h)
end

nminus1tot=sum(Nminus1);
tdelaytot=sum(Tdelay);
kappatot=sum(Kappa);
kLtot=sum(KL);
ktot=sum(K);
xvecttot=sum(Xvect);

figure
plot(fvect, nminus1tot)
xlabel('Relative frequency [GHz]')
ylabel('n-1')

figure
plot(fvectshort, tdelaytot)
xlabel('Relative frequency [GHz]')
ylabel('Excess time delay [ns]')

figure
plot(fvect, kappatot)
xlabel('Relative frequency [GHz]')
ylabel('Extinction coefficient')

figure
semilogy(fvect, kLtot)
xlabel('Relative frequency [GHz]')
ylabel('absorbance')

figure
plot(fvect, ktot)
xlabel('Relative frequency [GHz]')
```

```
ylabel('k [cm-1]')

figure
plot(fvect, Nminus1(1,:), fvect, Nminus1(2,:), fvect, Nminus1(3,:),
fvect, Nminus1(4,:), fvect, Nminus1(5,:), fvect, Nminus1(6,:), fvect,
Nminus1(7,:), fvect, Nminus1(8,:))
xlabel('Relative frequency [GHz]')
ylabel('n-1')

figure
plot(fvectshort, Tdelay(1,:),fvectshort, Tdelay(2,:),fvectshort,
Tdelay(3,:),fvectshort, Tdelay(4,:),fvectshort, Tdelay(5,:),fvectshort,
Tdelay(6,:),fvectshort, Tdelay(7,:),fvectshort, Tdelay(8,:))
xlabel('Relative frequency [GHz]')
ylabel('Excess time delay [ns]')

figure
plot(fvect, Kappa(1,:), fvect, Kappa(2,:), fvect, Kappa(3,:),fvect,
Kappa(4,:), fvect, Kappa(5,:), fvect, Kappa(6,:), fvect, Kappa(7,:),
fvect, Kappa(8,:))
xlabel('Relative frequency [GHz]')
ylabel('Extinction coefficient')

figure
semilogy(fvect, KL(1,:), fvect, KL(2,:), fvect, KL(3,:), fvect,
KL(4,:), fvect, KL(5,:), fvect, KL(6,:), fvect, KL(7,:),fvect, KL(8,:))
xlabel('Relative frequency [GHz]')
ylabel('absorbance')

figure
plot(fvect, K(1,:), fvect, K(2,:), fvect, K(3,:), fvect, K(4,:), fvect,
K(5,:), fvect, K(6,:), fvect, K(7,:), fvect, K(8,:))
xlabel('Relative frequency [GHz]')
ylabel('k [cm-1]')

tdelaytot=[0, tdelaytot];
a=[wvect; nminus1tot; tdelaytot; kappatot; kLtot; ktot; xvecttot;
Fvect];
```

E.2 Results of calculations

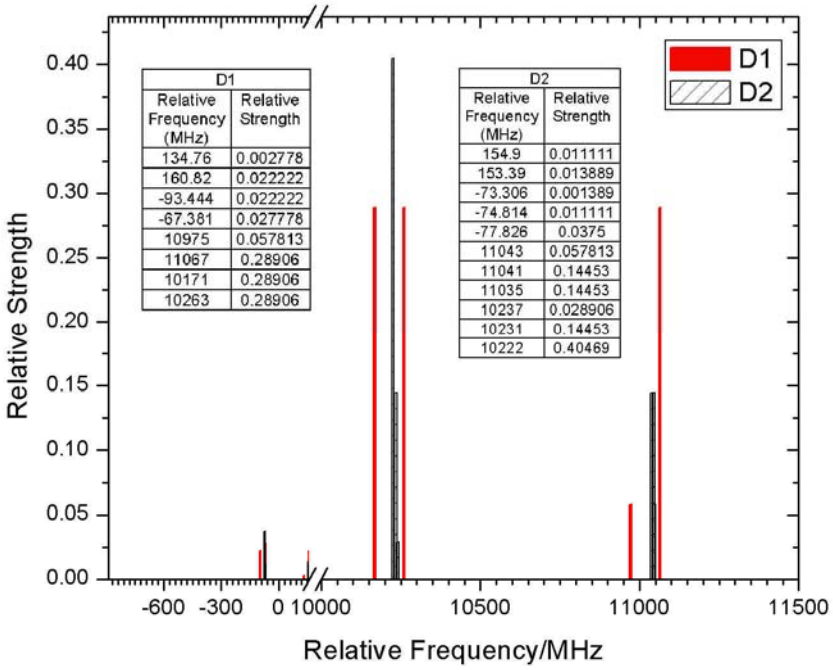

D1	
Relative Frequency (MHz)	Relative Strength
134.76	0.002778
160.82	0.022222
-93.444	0.022222
-67.381	0.027778
10975	0.057813
11067	0.28906
10171	0.28906
10263	0.28906

D2	
Relative Frequency (MHz)	Relative Strength
154.9	0.011111
153.39	0.013889
-73.306	0.001389
-74.814	0.011111
-77.826	0.0375
11043	0.057813
11041	0.14453
11035	0.14453
10237	0.028906
10231	0.14453
10222	0.40469

Figure E-1 Relative strengths and locations of lithium D1 and D2 hyperfine lines as well as tabular results.

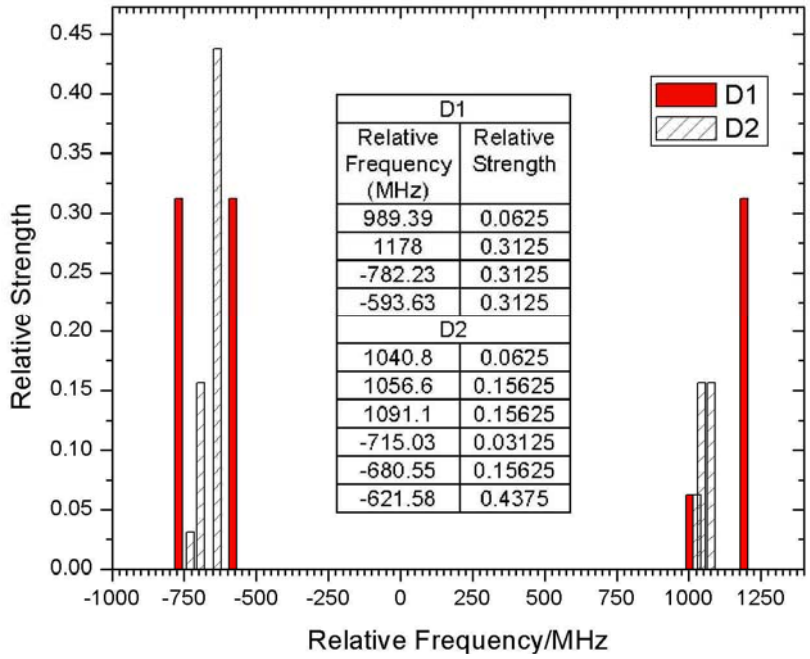

D1	
Relative Frequency (MHz)	Relative Strength
989.39	0.0625
1178	0.3125
-782.23	0.3125
-593.63	0.3125
D2	
1040.8	0.0625
1056.6	0.15625
1091.1	0.15625
-715.03	0.03125
-680.55	0.15625
-621.58	0.4375

Figure E-2 Relative strengths and locations of sodium D1 and D2 hyperfine lines as well as tabular results.

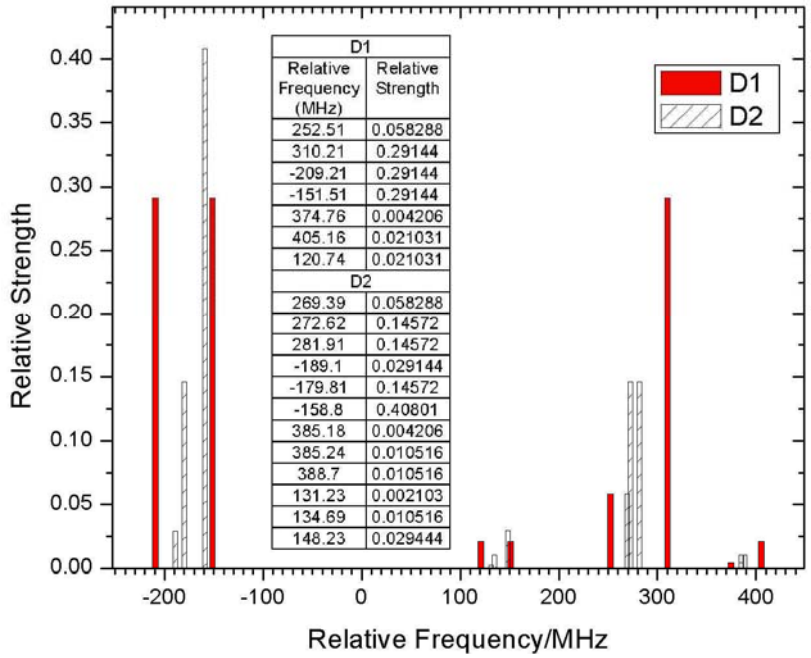

Figure E-3 Relative strengths and locations of potassium D1 and D2 hyperfine lines as well as tabular results.

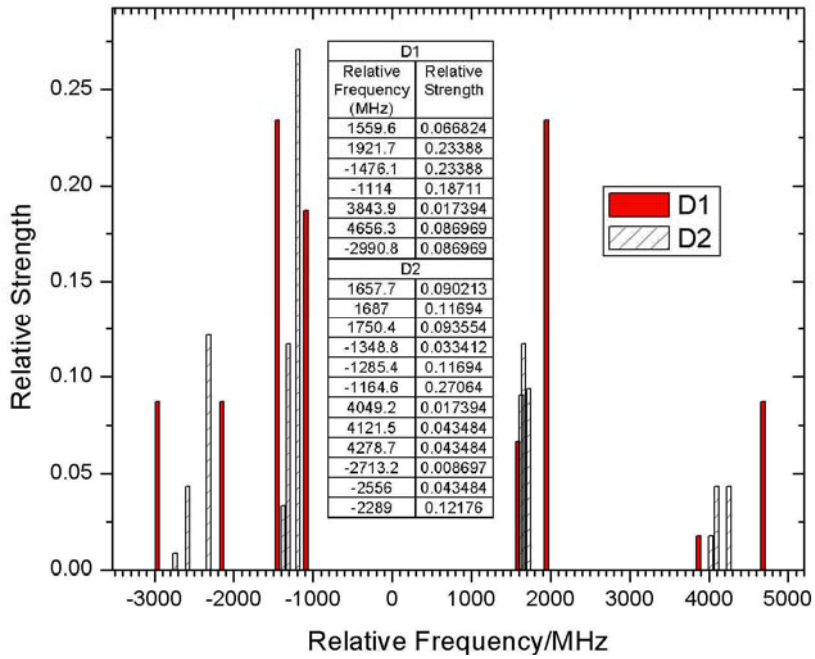

Figure E-4 Relative strengths and locations of rubidium D1 and D2 hyperfine lines as well as tabular results.

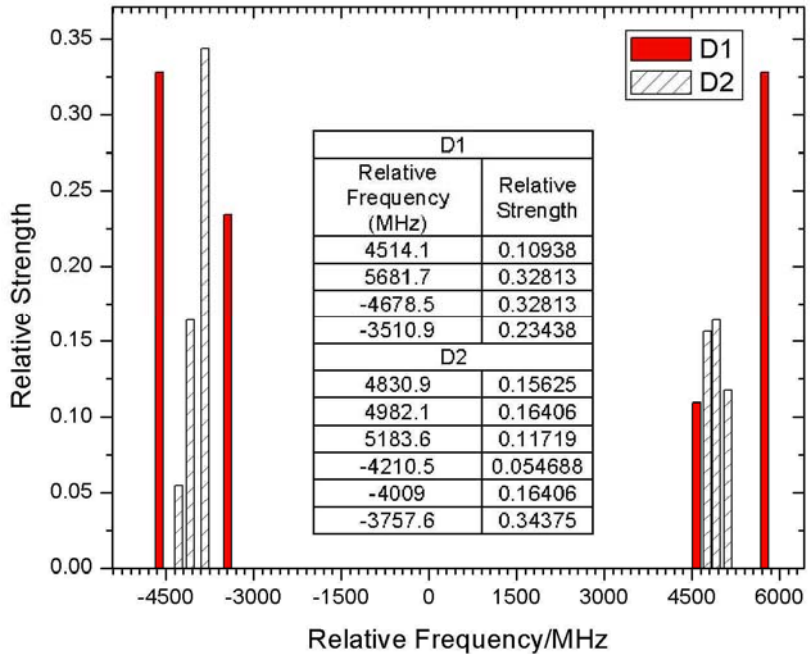

D1	
Relative Frequency (MHz)	Relative Strength
4514.1	0.10938
5681.7	0.32813
-4678.5	0.32813
-3510.9	0.23438
D2	
4830.9	0.15625
4982.1	0.16406
5183.6	0.11719
-4210.5	0.054688
-4009	0.16406
-3757.6	0.34375

Figure E-5 Relative strengths and locations of cesium D1 and D2 hyperfine lines as well as tabular results.

Appendix F Dispersion in Solids and Liquids

One of the most interesting facets of this research was the creation of a wavelength-agile source by passing light through a dispersive medium, in this case an atomic vapor cell. In some cases the high resolution of an AVC is unnecessary, but the ability to use the AVC at ultraviolet (UV) wavelengths, where most fibers perform poorly, is desired. A simulation was conducted in which a liquid or solid was placed in a White-cell in order to obtain a broad wavelength-agile source that operated in the UV. Particular wavelengths of interest are 227 nm, which is near a NO absorption line, and 308 nm, which is near an OH absorption line. Several possibilities were explored as outlined in the following sections.

F.1 SF66 glass

F.1.1 Description of analysis

SF66 glass from Schott Optical glass has a high index of refraction and a low Abbe number (high dispersion). Internal transmittance data versus wavelength as well as the constants for the Sellmeir equation were obtained from Schott [65]. The Sellmeir equation can be used to calculate the index of refraction, n, as shown in Equation (F-1), where λ [μm] is the wavelength.

$$n = \sqrt{1 + \frac{B1 \cdot \lambda^2}{\lambda^2 - C1} + \frac{B2 \cdot \lambda^2}{\lambda^2 - C2} + \frac{B3 \cdot \lambda^2}{\lambda^2 - C3}} \tag{F-1}$$

$$B1 = 2.07842233$$
$$B2 = 4.07120032 \cdot 10^{-1}$$
$$B3 = 1.76711292$$
$$C1 = 1.80875134 \cdot 10^{-2}$$
$$C2 = 6.79493572 \cdot 10^{-2}$$
$$C3 = 2.15266127 \cdot 10^{2}$$

The internal transmittance was provided for a 25 mm path length of glass. A wavelength of interest, such as 400 nm, was chosen and a vector of wavelengths covering a 1% range at 400 nm (i.e. 400 nm to 404 nm) was created. The transmittance and index of refraction at each of these colors were determined. Based on the minimum transmittance in the range of wavelengths chosen and the length of 25 mm, the length of glass at which the transmittance would be 1% was calculated from Equation (F-2), in which τ is the transmittance, k [m^{-1}] is the spectral absorption coefficient (calculated from the given data), and L [m] is the length.

$$\tau = e^{-kL} \tag{F-2}$$

The group velocity (Equation (4-9)) was calculated from the index of refraction and then the excess delay time (Equation (4-10)) was calculated based on the group velocity and the length of the glass at 1% transmittance. In order to assess the performance of the glass the total temporal separation between 400 and 404 nm, or delay, was calculated. Table F-1 lists several 1% wavelength ranges and the resulting temporal separation achieved by passing the light through a SF66 crystal of length L.

Table F-1 Performance of SF66 as a wavelength-agile source.

Wavelength Range (nm)		Delay (ps)	Length of Crystal (m)	Delay/Length (ps/m)
400	404	3.86	0.08	48.25
500	505	63.7	3.23	19.72
546	551.46	103	7.62	13.52

It is apparent from this table that SF66 does not produce much delay; it is also interesting to note that as wavelength increases the delay and length increase. The increase in length indicates that there is less absorption in SF66 at redder colors. The following section contains the Matlab code used to perform the analysis.

F.1.2 Matlab code used for analysis

```
%Constants of dispersion formula (Sellmeir equation) for SF66 glass
B1=2.07842233e0;
B2=4.07120032e-1;
B3=1.76711292e0;
C1=1.80875134e-2;
C2=6.79493572e-2;
C3=2.15266127e2;

c=3e8;  %speed of light, m/s
%values of internal transmittance for a 25mm path SF66 taken from
%www.schott.com
tau=[.7 .74 .92 .99 .995 .990 .989 .989 .988 .985 .965 .89 .77 .61 .34
.24 .05];
%wavelengths at which the tau is as in the vecotor, again in um SF66
taken from
%www.schott.com
taulam=[2.5 2.325 1.97 1.53 1.06 .7 .66 .62 .58 .546 .5 .46 .436 .42
.405 .4 .39];
mini=0.225;  %wavelength at the low end of the wavelength range [um]
maxi=mini+mini.*0.01;   %wavelength at the high end of the wavelength
range, 1% larger than minimum [um]
lam=[mini maxi];    %two point wavelength vector
lam2=mini:.001:maxi;    %multiple point wavelength vector with a
spacing of 0.001 um
tauinterp=interp1(taulam, tau, lam, 'cubic');   %value of the
transmittance at the maximum and minimum wavelengths
```

```
taunom=interp1(taulam, tau, mini);   %Nominal tau, based on the minimum
internal transmittance in the range
plot(taulam, tau)
knu=-log(tauinterp)./0.025; %spectral absorption coefficient m-1 for a
25 mm length of SF66
L=0.025*log(0.01)./log(taunom)  %length if we assume 1% transmittance
[m] (based on transmittance at 25 mm length)
omega=c./(lam2*1e-6)*2*pi;  %wavelength vector converted to frequency
[rad/s]
n=sqrt(1+B1*lam2.^2./(lam2.^2-C1)+B2*lam2.^2./(lam2.^2-
C2)+B3*lam2.^2./(lam2.^2-C3)); %index of refraction calculated from
Sellmeir equation
dndw=diff(n)./diff(omega);  %numerical derivative of index with respect
to frequency
Vg=c./(n(2:end)+omega(2:end).*dndw);    %group velocity delay [m/s]
Tdelay=L./Vg-L/c;        %time delay [s]
DELTAT=(max(Tdelay)-min(Tdelay))*1e9   %[ns] difference between time
delay at the nominal frequency and at 1% of the nominal frequency
```

F.2 RP-1

F.2.1 Description of analysis

The next material that was chosen for this study was RP-1, which is a jet fuel. This liquid was chosen because its properties are readily available [66]. In this case the values of the complex index of refraction for several wavelengths were available. Unfortunately, the variation in index with color was small over the range of wavelengths provided in the reference, so only one useful value of delay was calculated. In a 1% wavelength range of 476.5 to 481.27 nm and through a 1.32 m length of RP-1 corresponding to 1% transmittance, the delay was 85 ps (64.4 ps/m). Comparing these results to those obtained for SF66 at 500 nm it is apparent that RP-1 is an improvement; the delay is larger while the length is smaller. However, the performance at lower wavelengths is still questionable.

F.2.2 Matlab code used for analysis

```
%RP-1, values from www.luxpop.com
n=[1.501 1.448 1.446 1.447 1.439];  %value of the index of refraction
taken directly from luxpop
nlam=[.193 .4765 .488 .5145 .532];  %wavelength corresponding to each
index of refraction [um]
c=3e8;  %speed of light, [m/s]
mini=0.4765;  %lower end of wavelength range [um]
maxi=mini+mini.*0.01;  %upper end of wavelength range [um]
lam=[mini maxi];    %vector of wavelength range
lam2=mini:.001:maxi;    %creation of a wavelength vector covering the
range with 0.001 um separation
ninterp=interp1(nlam, n, lam2, 'cubic');    %index of refraction for
the new wavelength vector
k=[82039.518 3.455 2.601 1.92 .824];    %spectral absorption
coefficient from luxpop [m-1]
knom=interp1(nlam, k, mini, 'cubic');   %spectral absorption
coefficient for the new wavelength vector
tau=0.01;   %1% transmission
L=-log(tau)./knom  %length if we assume 1% transmittance [m]
omega=c./(lam2*1e-6)*2*pi;  %wavelength vector converted to frequency
[rad/s]
dndw=diff(ninterp)./diff(omega);  %numerical derivative of index with
respect to frequency
Vg=c./(ninterp(2:end)+omega(2:end).*dndw);    %group velocity delay
[m/s]
Tdelay=L./Vg-L/c;         %time delay [s]
DELTAT=(max(Tdelay)-min(Tdelay))*1e9   %[ns] difference between time
delay at the nominal frequency and at 1% of the nominal frequency
```

F.3 Water

F.3.1 Description of analysis

Water was a natural material to examine because it is very easy to obtain and work with and it has been well studied, so data on the index of refraction were readily available. In this case the analysis was performed in two ways, one used measurement data [67-69] and the other used an equation derived from measurement data [70]. The reason for using the equation is shown in Figure F-1, part (c); after interpolating the measurement data the results were noisy, whereas the equation results were smooth and similar enough to the measured values for this analysis. As in the previous investigations

the delay time and path length of water were calculated based on 1% transmittance and a 1% wavelength range. The calculated path length is shown in Figure F-1, part (a), and part (b) shows the expected delay over a 1% wavelength range. The color axis is based on the central color in the 1% range (i.e. 402 nm represents a range from 400 to 404 nm). In addition to the index of refraction data a figure of group velocity dispersion (GVD) was found [71]. The GVD was calculated using the index of refraction data previously mentioned and compared to the figure in order to verify the accuracy of the Matlab code. The results were in reasonably good agreement.

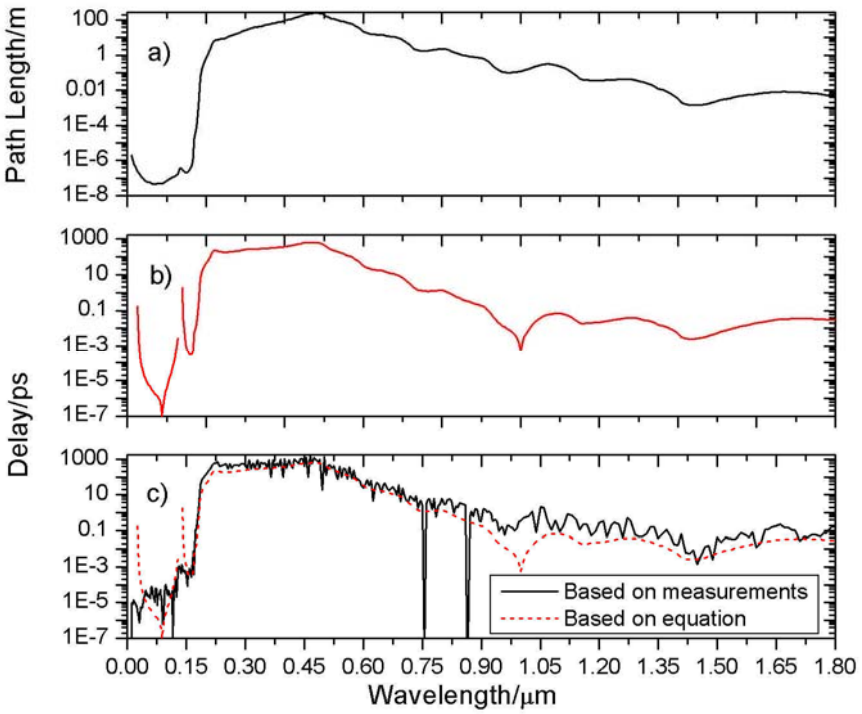

Figure F-1 Results of dispersion through water. a) Path length of water for 1% transmittance. b) Delay between the maximum and minimum wavelengths over a range of 1% of the minimum wavelength. c) Delay calculated from measured index of refraction and from calculated index of refraction.

The results for several wavelengths are presented in Table F-2. Looking back at Table F-1 it is apparent that water is more useful as a wavelength-agile source than SF66.

One problem with water is that the best performance occurs near 500 nm, but a substance with optimal performance around 225 nm is desired. This led to a search for a substance with absorption lines in the vacuum ultraviolet (VUV) and an absence of lines in the visible; the hope was that this substance would achieve its best performance further into the UV. Xenon, which is discussed in the following sections, met this requirement.

Table F-2 Performance of water as a wavelength-agile source.

Wavelength Range (nm)		Delay (ps)	Length of Crystal (m)	Delay/Length (ps/m)
223.875	226.125	219	7	31.3
400	404	370	93	3.98
500	505	447	200	2.24

F.3.2 Matlab code used for analysis

```
%Water, values from Painter, optical msmts of liq water in VUV, and
Raty
%complex refractive index of liquids, and Segelstein
data=load('F:\Calculations\liquid dispersion\water_complex.m'); %load
in the wavelength, index of refraction, and extinction coefficient
%data=load('C:\Documents and Settings\Mandy Pertzborn\Desktop\New
Briefcase\data etc\Calculations\water_complex.m');
paper=load('F:\Calculations\liquid dispersion\GVDfrompaper.m'); %loads
a plot of group velocity dispersion from Kolesik paper
xpaper=paper(:,1).*1e15;    %vector of x-values, which are angular
frequency [1/s]
ypaper=paper(:,2).*1e-25;   %vecotor of y-values, which are group
velocity dispersion [s2/m]
lam=data(:,1);    %vector of wavelengths corresponding to index of
refraction [um]
n=data(:,2);    %vector of index of refraction values
k=4*pi./(lam.*1e-6).*data(:,3); %convert extinction coefficient to
spectral absorption coefficient [m-1]
c=3e8;  %speed of light [m/s]
% mini=[.18 .2 .22 .24 .26 .28 .3 .4 .5 .6 .7 .8 .9 1 1.2 1.3 1.4 1.5
1.6 1.7];  %wavelength in um
% mini=.1:.01:.3;%[.2 .21 .22 .23 .24 .25 .26 .27 .28 .29 .3 .31 .32
.33 .34 .35 .36 .37 .38 .39 .4];
% maxi=mini+mini.*0.01;
% lam=[mini maxi];
```

```
%set up empty vectors that will be filled during the loop
dt=[];
len=[];
scatt=[];
kscatt1=[];
knew=[];
trans=[];
GVD=[];
ncen=[];

dteq=[];
GVDeq=[];

i=1;
lamcen=[];
while lam(i)<1.8
    lam2=lam(i)*(1-.005):(lam(i)*(1+.005)-lam(i)*(1-
.005))/100:lam(i)*(1+.005); %creates a wavelength vector where the
maximum value is 1% larger than the minimum value [um]
    Domega=3e8*2*pi*(1/min(lam2)-1/max(lam2))*1e6;  %calculates the
difference between the minimum and maximum wavelength in [rad/s]
    ninterp=interp1(lam, n, lam2, 'linear'); %finds a value for the
index of refraction for each wavelength
    knom=interp1(lam, k, lam(i), 'linear'); %finds a value for the
spectral absorption coefficient for each wavelength [m-1]
    tau=0.01;   %assumes 1% transmittance
    L=-log(tau)./knom;  %length if we assume 1% transmittance [m]
    transtot=exp(-knom*L);
    omega=c./(lam2.*1e-6)*2*pi; %convert wavelength to frequency
[rad/s]

    %calculate n based on equation from IAPWS release on the properties
of water
    %and steam
    %These first values are constants used in the equation
    a0=.244257733;
    a1=9.74634476e-3;
    a2=-3.73234996e-3;
    a3=2.68678472e-4;
    a4=1.5892057e-3;
    a5=2.45934259e-3;
    a6=.90070492;
    a7=-1.66626219e-2;
    lamUV=.2292020;
    lamIR=5.432937;
    lambar=lam2./.589;  %This is the wavelength vector for which index
of refraction will be calculated [um]
    Tbar=298/273.15;
    rhobar=998/1000;

X=a0+a1*rhobar+a2*Tbar+a3.*lambar.^2*Tbar+a4./lambar.^2+a5./(lambar.^2-
lamUV^2)+a6./(lambar.^2-lamIR^2)+a7*rhobar^2;
    ninterpeq=sqrt((1+2*rhobar.*X)./(1-rhobar.*X)); %calculated index
of refraction
```

```
    %calculations based on measured data
    dndw=diff(ninterp)./diff(omega);    %numerical derivative of index
with respect to frequency
    Vg=c./(ninterp(2:end)+omega(2:end).*dndw);    %group velocity delay
[m/s]
    Tdelay=L./Vg-L./c;        %time delay [s]
    DELTAT=(max(Tdelay)-min(Tdelay))*1e9;   %[ns] difference between
time delay at the nominal frequency and at 1% of the nominal frequency
    kscatt=997.8*6.026e26/18.02*8/3*pi^3/(lam(i)*1e-6)^4*((n(i)^2-
1)/(n(i)^2+2)).^2/(2.69e25)^2;%997.8*6.026e26/18.02*4*pi*4*pi^2*(n(i)-
1).^2./(2.69e25)^2./(lam(i).*1e-6).^4;
    scatt1=exp(-kscatt.*L);
    GVD1=DELTAT*1e-9/Domega/L;

    %calculations based on data calculated from equation
    dndweq=diff(ninterpeq)./diff(omega);
    Vgeq=c./(ninterpeq(2:end)+omega(2:end).*dndweq);    %group velocity
delay [m/s]
    Tdelayeq=L./Vgeq-L./c;        %time delay [s]
    DELTATeq=(max(Tdelayeq)-min(Tdelayeq))*1e9;   %[ns] difference
between time delay at the nominal frequency and at 1% of the nominal
frequency
    GVD1eq=DELTATeq*1e-9/Domega/L;

    %save the data
    kscatt1=[kscatt1, kscatt];
    knew=[knew,k(i)];
    dt=[dt, DELTAT];
    len=[len, L];
    lamcen=[lamcen,lam(i)];
    scatt=[scatt, scatt1];
    transtot=exp(-(kscatt+k(i)).*L);
    trans=[trans, transtot];
    GVD=[GVD, GVD1];

    dteq=[dteq, DELTATeq];
    GVDeq=[GVDeq, GVD1eq];

    i=i+1;
end

figure
semilogy(lamcen, dt.*1000, lamcen, dteq.*1000)
title('Delay(ps)over 1% wavelength vs. the lower end wavelength (um)')
figure
semilogy(lamcen, len)
title('length (m) vs. lower end wavelength')
figure
semilogy(lamcen, dteq.*1000)
title('Delay(ps) over 1% wavelength vs. the center wavelength (um)')
ylabel('Delay over 1% [ps]')
xlabel('Wavelength [um]')
```

F.4 Xenon

F.4.1 Description of analysis

Xenon has absorption lines in the range of 104 to 147 nm and then no lines until 340 nm; xenon therefore appeared to be ideal for creating a wavelength-agile source near 225 nm. Unfortunately this did not turn out to be the case. Both glass and water performed better than liquid xenon, which achieved a delay time of about 35 ps over a length of 116 km (0.0003 ps/m) at 225 nm. Even if the delay of 35 ps was acceptable, the 116 km path length was unacceptable. Figure F-2 shows the results of the xenon calculations. In this case the index of refraction was calculated using a method similar to that outlined in Chapter 4 for the atomic vapor cell. However, in the case of xenon the pressure was high enough that a Lorentzian line shape dominated, thereby simplifying the calculation. This domination of the Lorentzian rather than the Gaussian line shape led to the poor performance of xenon versus something like glass or water. In the case of a Lorentzian line shape the index of refraction, and therefore the group velocity, does not change quickly with color except right near the peak of the absorption line. As seen in Figure F-2 the location of the absorption lines is not near 225 nm. In fact, the lines are located too far into the UV to make them useful for measuring species such as OH. The long Lorentzian tail does mean that it is possible to obtain the desired delay, but the path length of xenon would be prohibitively long.

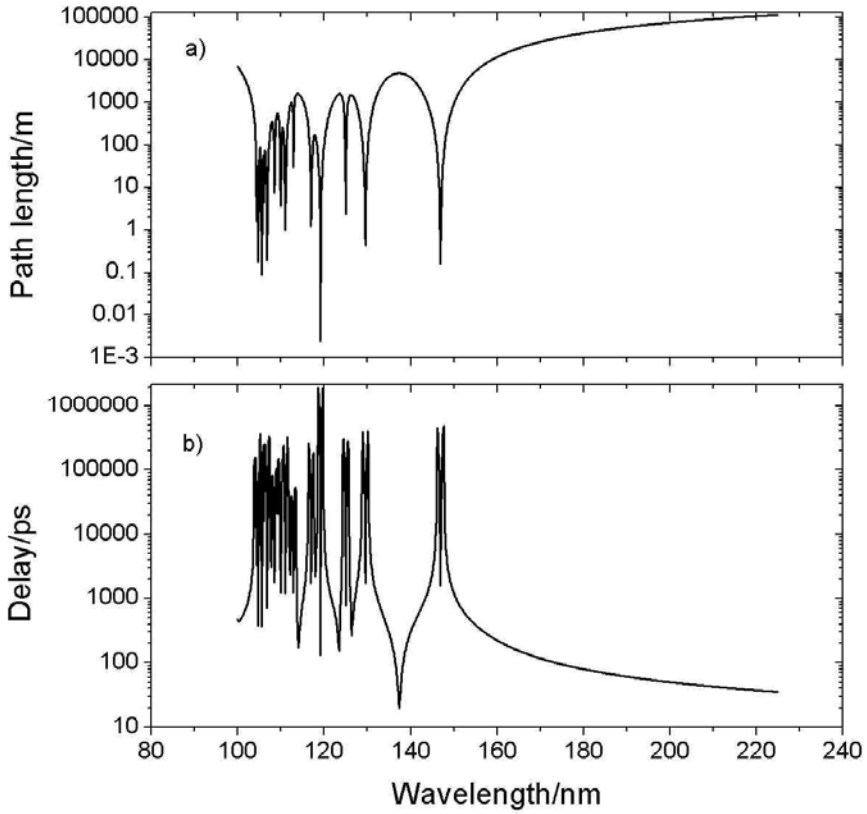

Figure F-2 Results of modeling xenon as a wavelength-agile source. a) The path length of xenon near 225 nm, which is the desired wavelength of operation, is extremely long. b) The delay near 225 nm is not very large.

F.4.2 Matlab code used for analysis

```
clear all
clc
close all
format long e
%12-3-2004
%Designed to calculate spectra for each xenon absorption line
%Element specific items:    PPa, T (vapor pressure curve), lam
(composite
%line frequency), A, HFSamp and HFStrans (hyperfine line amplitudes and
%locations), f, twogam, M, L (not element specific, but may vary), and
the
%indices used in plotting the individual hyperfine line results.

%inputs are wavelength, Einstein A coefficients, and oscillator
strengths.
const=load('F:\Calculations\liquid dispersion\xenonconstants.m');

PPa =5e4; %Pa, pressure
T =300;%298; %K, temperature
```

```
rho=.02632;   %density kg/m3
twogam =1.1348e6; %Hz/Pa    estimate of pressure broadening coefficien
M=131.29 ;   %amu, mass of absorption element
pts = 100000 ; %Number of data points evaluated
L = 1;%m, length of cell
c = 3e8; %m/s, speed of light in a vacuum
Patm = PPa/101325; %atm
n = rho/M*6.026e26;%number density [m-3]

%Set empty matrices that the data will be saved into
Nminus1=[];
Tdelay=[];
Kappa=[];
KL=[];
K=[];
geninttot=[];
Fvect=[];
Nuvect=[];
Fvectshort=[];
Wvect=[];
WL=[];
Wao=[];
kappa=[];
Xvect=[];
wLs=[];
scale=(1/100-1/230)*2*pi*3e8/1e-9;

for z=1:size(const,1)
    lam=const(z,1)*1e-9;    %selects the wavelength from the input
matrix
    A=const(z,2);    %selects the A coefficient from the input matrix
    f=const(z,3);       %selects the oscillator strength from the input
matrix

    wao = c/lam*2*pi;   %lambda converted to frequency in rad/s, this
is the center frequency for each line
    delwL =(twogam*PPa*2*pi+A) ;  %homogeneous broadening due to
pressure broadening and natural broadening
    delwD = 7.17e-7*wao*sqrt(T/M) ;  %Doppler width, inhomogenous
broadening effect, in this case delwL dominates

    q=1.6e-19;  %[C] charge of an electron
    eo=8.854e-12;    %[C2/N-m2] permittivity of free space
    me=9.11e-31;     %[kg] mass of an electron
    kb=1.38e-23;     %boltzman constant [J/K]

    limw1 = wao-scale;  %Sets frequency for low end (most negative)
    limw2=wao+scale;    %sets frequency for upper end
    wstep = (wao-limw1)/pts*2 ;  %sets step size

    w=[limw1:wstep:limw2];  %creates frequency vector [rad/s]
```

```
    ncomplex=f*n*(q)^2./(2*eo*me.*(wao^2-w.^2+i.*delwL.*w));
%calculates the complex index of refraction for a Lorentzian dominated
line shape

    nrefract=real(ncomplex)+1;  %calculates the index of refraction

    nminus1=real(ncomplex);     %calculates index of refraction minus 1

    kappa=-imag(ncomplex);  %calculates the extinction coefficient
    dndw=diff(nrefract)./diff(w);   %calculates change in index of
refraction with frequency in rad/s, Yalin, Barker and Miles
    wvectshort=w(2:end);    %in calculating dndw I lose a data point,
so I need to shorten the vectors
    nrefractshort=nrefract(2:end); %in calculating dndw I lose a data
point, so I need to shorten the vectors
    Vg=c./(nrefractshort+wvectshort.*dndw);   %calculates the GVD
    tdelay=(L./Vg-L/c).*1e9;   %calculates the delay time in ns
    propagation=2*pi/(lam); %m-1 propagation number, weird constant in
spectroscopy, usually cm-1
    kL=2.*kappa*propagation.*L; %absorbance
    k=2*kappa*propagation;  %m-1 spectral absorption coefficient
    Trans=exp(-kL);  %transmission
    fvect = (w-wao)/2/pi/1e9; %GHz converts from rad/s to GHz
    nuvect = fvect/30; %cm-1    converts from GHz to wavenumber
    fvectshort=fvect(2:end);    %in calculating dndw I lose a data
point, so I need to shorten the vectors
    Nminus1=[Nminus1; nminus1];
    Tdelay=[Tdelay; tdelay];
    Kappa=[Kappa;kappa];
    KL=[KL;kL];
    K=[K;k];
    Nuvect=[Nuvect; nuvect];
    Wvect=[Wvect; w];
    Fvect=[Fvect;fvect];
    Fvectshort=[Fvectshort; fvectshort];
    Wao=[Wao; wao];

 end



close all
clear all
clc
format long e
%11-11-04
%Calculations using xenon as the wavelength agile source.  The goal is
to
%find a substance which can produce a wavelength agile source near 225
nm.
%The first step was to find the absorption lines for xenon which are in
the
%VUV and range from 104 nm to 147 nm.  These lines were then fit with a
```

```
%Lorentzian line shape using another Matlab code.  The results were
loaded
%into this code.
load('F:\Calculations\liquid dispersion\12_7_04_ncheck.mat');
c=3e8;  %speed of light [m/s]
lambda=[100:.1:225];    %wavelength vector [nm]
omega=c./(lambda*10^(-9)).*2*pi;    %frequency vector [rad/s]

%setup empty vectors to store variable data
wvectlong=[];
totalkap=[];
totaln=[];
totalk=[];
dt=[];
len=[];
tau1=[];

%This loop will determine what the extinction coefficient, index of
%refraction, and spectral absorption coefficient are for the specified
%wavelengths
for z=1:size(Kappa, 1)
    inter=interp1(Wvect(z,:), Kappa(z,:), omega, 'cubic');
    totalkap=[totalkap; inter];
    inter=interp1(Wvect(z,:), Nminus1(z,:), omega, 'cubic');
    totaln=[totaln; inter];
    inter=interp1(Wvect(z,:), K(z,:), omega, 'cubic');
    totalk=[totalk; inter];
end

%These lines add the results for the individual absorption lines
together
%so that the result is just one long spectrum.
totalkappa=sum(totalkap);
totalindex=sum(totaln)+1;
totalabscoeff=sum(totalk);

%This is a plot of the wavelength versus the index of refraction
plot(3e8*1e9*2*pi./omega, totalindex-1)

%This loop calculates the group velocity for each wavelength range
h=waitbar(0,'length')
for z=1:length(omega)
    waitbar(z/length(omega))
    mini=omega(1,z)*(1-.005);   %lower end of the 1% wavelength range
    maxi=omega(1,z)*(1+.005);   %upper end of the 1% wavelength range
    range=[mini:.0001*omega(1,z):maxi]; %vector creating full
wavelength range
    ninterp=interp1(omega, totalindex, range, 'cubic'); %calculation of
index of refraction for the wavelength range
    kinterp=interp1(omega, totalabscoeff, omega(1,z), 'cubic');
%calculation of spectral absorption coefficien for the wavelength range
    tau=.01;    %transmittance of 1%
    L=-log(tau)./(kinterp); %path length based on 1% transmittance
```

```
    dndw=diff(ninterp)./diff(range);    %derivative of index of
refraction with respect to the frequency
    Vg=c./(ninterp(2:end)+range(2:end).*dndw);    %group velocity
delay, m/s
    Tdelay=L./Vg-L./c;        %time delay, s
    DELTAT=(max(Tdelay)-min(Tdelay))*1e9;   %ns difference between time
delay at the nominal frequency and at 1% of the nominal frequency
    dt=[dt, DELTAT];
    len=[len, L];
    tau1=[tau1,tau];
end
close(h)

%plots of the results
figure
semilogy(3e8*1e9*2*pi./omega, totalabscoeff)
title('k (m-1) vs. wavelength (nm)')
figure
semilogy(3e8*1e9*2*pi./omega, dt.*1000)
title('Delay(ps) over 1% wavelength at 1% transmission vs. the center
wavelength (nm)')
figure
semilogy(3e8*1e9*2*pi./omega, len)
title('length (m) vs. center wavelength')
```

F.5 Conclusions

These calculations yielded mixed results. It appears that at the wavelengths of interest, such as 227 nm, the only material that may be useful as a wavelength-agile source is water. Table F-3 compares the results for water at this wavelength to the results for materials which can be used in optical fibers (and therefore obtained in long lengths). The water based system outperforms the sapphire and KCI glasses and is comparable to UV grade fused silica.

Table F-3 Comparison of materials used to create wavelength-agile sources at 225 nm with 1% transmittance over a 1% wavelength range.

Material	Length (m)	Delay (ps)	Delay/Length(ps/m)
Sapphire	0.2	7.6	38
KCI	0.42	33	79
UV grade fused silica	15	255	17
Water	7	219	31

Appendix G Synthetic Measurement Data

In the course of this research a method was developed to create synthetic measurement data that could be used to verify the data analysis method prior to making any measurements. The method was based on substituting a Gaussian curve for the Rayleigh scattering spectrum; the energy of the Gaussian curve was equal to the estimated scattering energy. It was in the course of calculating this energy that it was determined that less than one photon was expected to reach the detector during a measurement; the decision to use photon counting was, therefore, made at this point. Once the synthetic data were created the results were fitted using weighted and un-weighted non-linear least squares fits [72].

G.1 General method

The creation of the synthetic data involved multiple steps which are outlined in this section. Figure G-1 shows the major steps in creating synthetic data and then fitting that data in order to determine certain characteristics. This flow chart specifically details the steps in fitting a Gaussian curve. First the *FWHM* and *center* of the curve were set and a random number generator was utilized in several steps in order to create an array of amplitudes, y, which represented the number of electrons arriving at the PMT in a given time range, t; these values composed the synthetic data. These data were then compared to the values calculated from a Gaussian equation. In this case a Matlab optimization code varied the amplitude (*Amp*), *FWHM*, and *center* until the measured and calculated y-values were close. The *Amp* variable was just a scale factor so that the y data could

have arbitrary units. In the case of Rayleigh scattering in a gas the values of temperature and pressure would be the variables. This fit was then evaluated.

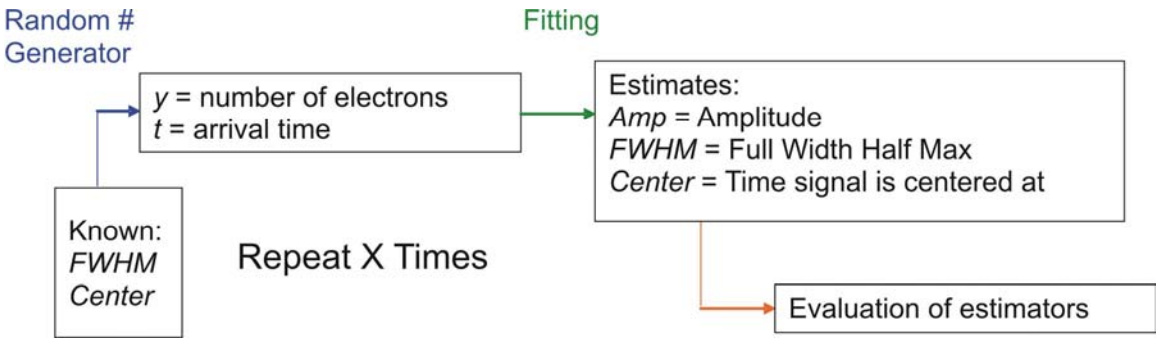

Figure G-1 Flow chart illustrating the process of first creating synthetic measurement data and then fitting that data in order to verify the fitting procedure. The value of X can be as large as desired, but 1000 is recommended.

The following steps outline the creation of synthetic measurement data in detail.

1) Estimate the amount of energy scattered for each laser pulse (see section 2.3.2).

2) Estimate the number of photons arriving at the detector based on the result of step 1 and the energy of one photon.

3) Estimate the number of electrons that are emitted by the photocathode based on the PMT QE and the results of step 2. An event occurs whenever an electron is emitted from the photocathode.

4) Use a Poisson random number generator to generate the number of electrons expected in a given number of measurements. The results of step 3 are an input to this step.

5) Create a signal function, in this case a Gaussian line shape (this could be a model of the Rayleigh scattering spectrum). In this experiment the FWHM was 10 ns, the total spread of the data was 80 ns, and the curve was centered at 40 ns.

6) Create a comparison function that entirely encloses the curve of step 5. In this experiment a line was used. It is important that this function is close to the function from step 5; if it is too much larger then the program will take longer to run. This function is amplitude versus time, just like the function in step 5.

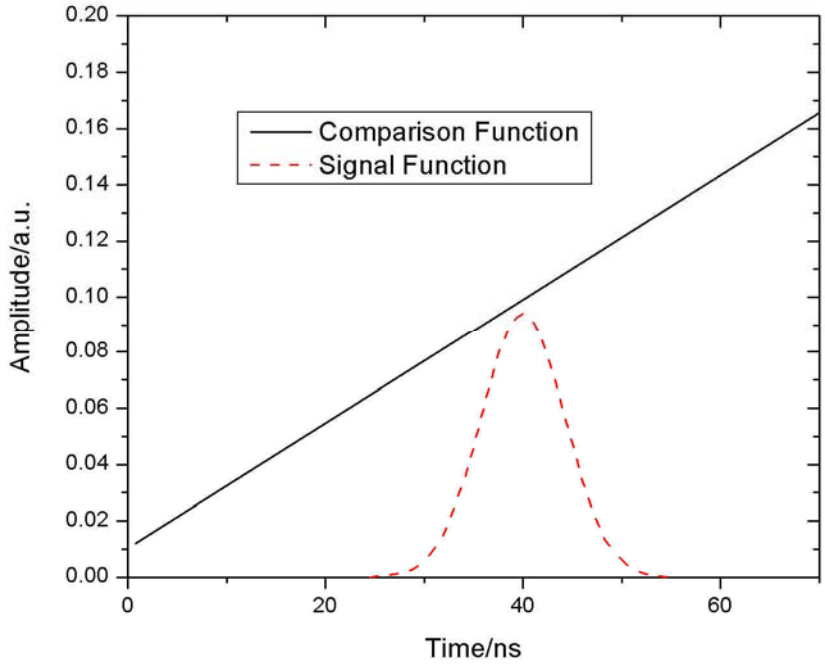

Figure G-2 Image of the comparison function enclosing the Gaussian signal function.

7) Calculate the total area enclosed by the comparison function.

8) Use a uniform random number generator to generate an area that is between 0 and the value calculated in step 7.

9) Integrate the comparison function and solve for the time at which the area of the function is equal to the area in step 8.

10) Calculate the y-value of the comparison function that corresponds to the time calculated in step 9.

11) Use the uniform random number generator to calculate a y-value that is between zero and the value calculated in step 10.

12) Calculate the value of the signal function at the time calculated in step 9.

13) Is the value from step 11 less than the value in step 12? Does the signal function enclose the randomly generated y-value? If the answer is yes then the time generated in step 9 is a valid time. It corresponds to the arrival time of an electron. If no, then the time generated in step 9 is rejected.

14) Repeat steps 8 through 13 until an arrival time has been calculated for each electron.

The result of the above steps is a matrix of arrival times which determine when photons which will result in the emission of an electron from the photocathode arrive at the PMT. Several things can be done with these data. Initially the data were binned based on a 4 ns width (based on the pulse duration after the pulse picker). A histogram was created by determining how many photons arrived in a given 4 ns period; this value became the amplitude and the x-value was based on the time at the center of the 4 ns bin. The result was a small array of times and amplitudes which mimicked what the signal would like when it was measured, as shown in Figure G-3. This was the synthetic data.

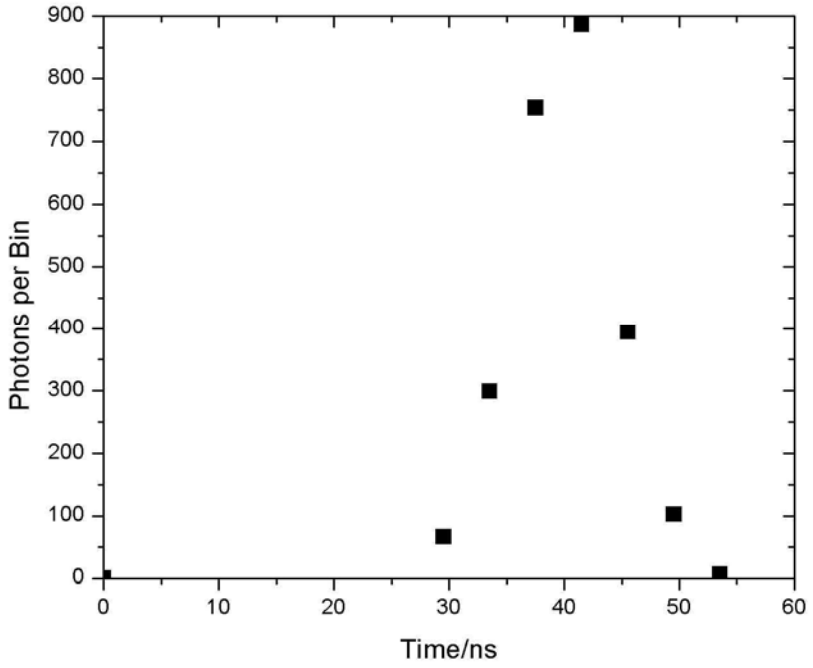

Figure G-3 Synthetic measurement data. The data have been put into 4 ns bins.

In later analyses, instead of binning the data a Gaussian line shape was applied to each point. The reason for this modification was that the photon counting process does not bin the measurement. For each photon that is counted the discriminator outputs an approximately Gaussian signal to the oscilloscope. Therefore, in order to model the results of photon counting each event was given a Gaussian line shape (2 ns FWHM) and these curves were then summed to create the synthetic data. This result is not valid for the final measurement technique, which used histograms. In that technique only the location of the peak of each discriminator output pulse was important; the result was similar to the original binning method.

The synthetic measurement data were treated as the actual measurements and input into the data analysis code. In the final iteration the data analysis code compares the measurement to the results of the theoretical S6 model. In this iteration the signal

function was Gaussian, which is a known equation, so the results were compared to the Gaussian equation which contained the known *FWHM* and *center*.

The fitting function compared the measured y-value for a given time, *t*, to the calculated y-value for that time based on a Gaussian equation. Equation (G-1) is the Gaussian equation used with the non-linear least squares optimization function in Matlab. The variables were *Amp*, *FWHM*, and the *center* of the Gaussian equation; recall that the known values were 1, 10 ns, and 40 ns, respectively. These values were varied by the Matlab function in order to find the parameters which minimized the value of Equation (G-2). In this equation σ is a weighting factor. For an un-weighted fit its value is one and for a weighted fit its value is the square root of the measured y-value. The results are shown in Figure G-4.

$$y_{calculated} = Amp\frac{2}{FWHM}\sqrt{\frac{\ln(2)}{\pi}}\exp\left[-4\ln(2)\left(t-\frac{center}{FWHM}\right)^2\right] \qquad \text{(G-1)}$$

$$lsq = \sum\left[\frac{1}{\sigma}\left(y_{measured} - y_{calculated}\right)\right]^2 \qquad \text{(G-2)}$$

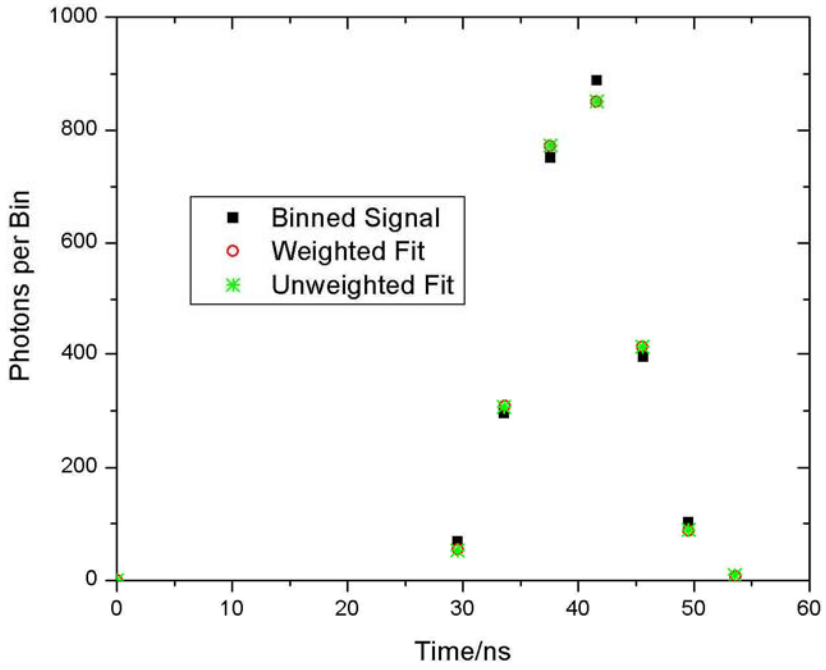

Figure G-4 The result of the fits is overlaid onto the raw synthetic data.

The outcome of the fitting code found *FWHM* and *center*, however, the "goodness of fit" still needed to be evaluated. The goodness of fit was determined by examining the relative uncertainty in the fit of the *FWHM* as the number of measurements was varied (step 4 above). The fit was performed 1000 times and the standard deviation and average were calculated based on the 1000 values obtained for the *FWHM*. The relative uncertainty is the standard deviation divided by the average value. Figure G-5 shows the results of the calculations. As the number of measurements increased the relative uncertainty approached an asymptote, indicating that after 10,000 measurements no further gains were made. Part (b) shows how well the fit "temperature" compared to the actual temperature. In this case, of course, the synthetic data had no temperature, but Doppler broadening as shown in Equation (A-2) does depend on temperature and is Gaussian. In these calculations the width, $\Delta\nu_D$, was set to the value of the *FWHM* and the

center, v_o, was set to the value of the *center*; both had units of ns. The final desired value was a ratio, so the ratio of T_f (fit temperature) to T_{act} (actual temperature) was calculated in Equation (G-3).

$$\frac{T_f}{T_{act}} = \left[\frac{FWHM_f}{FWHM_{act}} \frac{center_{act}}{center_f} \right]^2 \tag{G-3}$$

Part (b) of Figure G-5 indicates that like relative uncertainty, the fit of temperature was essentially as good as possible around 10,000 measurements. This figure also shows that the ratio does not reach a value of one, indicating that there was some bias in the fit.

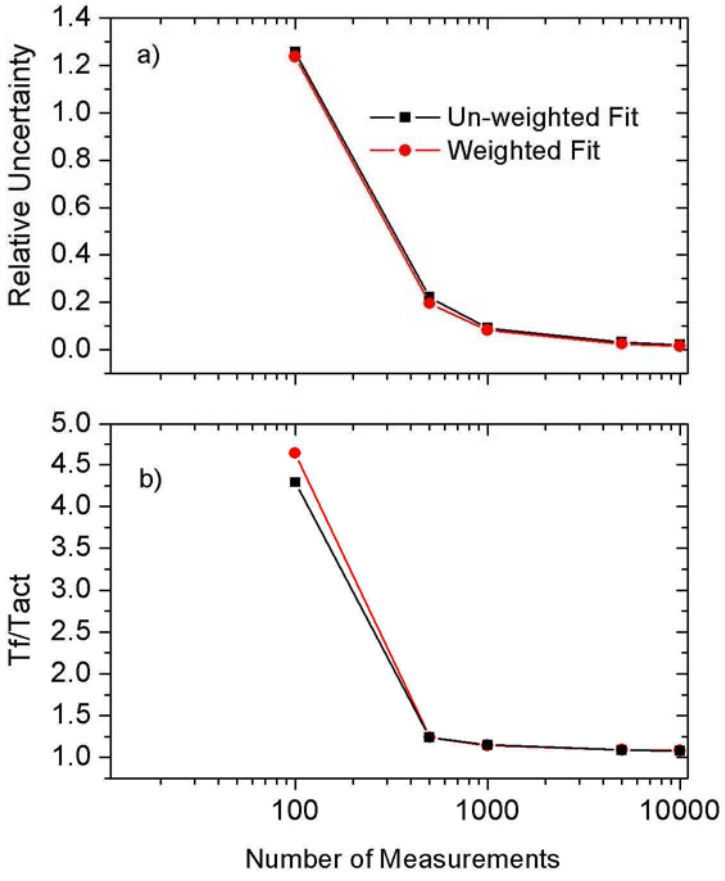

Figure G-5 Measure of the goodness of fit of the data analysis code. a) Relative uncertainty approaches an asymptote around 10,000 measurements. b) Ratio of the temperature provided by the fit, T_f, to the actual temperature. The temperature was calculated based on Doppler broadening.

In order to make this process more realistic the Gaussian curve has to be replaced by one representing the Rayleigh scattering spectrum and the fit must be made using the S6 model rather than the equation for a Gaussian curve. Both of these factors significantly complicated the code and in the end synthetic measurement data were not generated for the scattering spectrum. The signal was so weak and the comparison function was so difficult to develop that the generation of the synthetic data required too much time. However, the initial process was useful in developing an understanding of the fitting process and the complications that would be encountered.

G.2 Matlab codes

G.2.1 Main code

```
clear all
clc
close all
tic

%Creation of pdf based on Poisson Distribution based on power
calculations
%from distsingleKconv.m (470K, 0.3m cell, 2.54m diameter, -4.5 to -1.5
on
%the absorption curve.
Energy=6.5e-19 ;  %J, total energy per pulse
Lambda=770;  %nm
c=3e8;       %m/s
nu=c/(Lambda*1e-9); %Hz
PulseWidth=4e-9;     %s
h=6.63e-34 ;     %Js
phi_p=Energy/(h*nu);    %photons per pulse
QE=.1;             %Quantum Efficiency based on best available PMT's
for 770nm
mu=phi_p*QE;    %electrons per pulse
allx1=[];
res1=[];
allx2=[];
res2=[];
time=[];
event=[];
exit1=[];
exit2=[];
fitall=[];
```

```
k=1;
total=201;

while k<total

%Create a Poisson distributed data set based on mu and the desired
number of measurements.  Can use normplot to
%determine if it follows a normal distribution.
measurements=1e4;
data=poissrnd(mu,1,measurements);

%Calculate the total number of electrons inside the detector.  Multiple
%events can occur with each pulse.
photon=sum(data);

%Create signal pdf.  Right now it is based on Gaussian equation.
deltaT=10;   %ns, FWHM pulsewidth
T=80;   %ns, total width of pulse
t=[0:deltaT/60:T]; %ns, time vector
%calls function that has the equation for the pdf.  It may also be raw
%data, although that will require some code modification
pdf=signalpdf(deltaT,T,t);

%Create a function that will enclose the pdf.  The closer the function
is
%to the actual shape, the faster the selection of random numbers.  For
this
%project, just use a line.  Reality, I will have to look at the
%actual pdf and try to come up with a fit.
ft=fx(pdf,deltaT,T,t);

%What is the area of the comparison signal?
A=trapz(t,ft);

%Here the reject code does its stuff and returns a vector of random
times
%whose size is equal to the number of electrons
arrival=reject(pdf,deltaT,T,t,photon,A);

%Here we need to create the final measurement curve based on the rise
time
%of the detector.  These steps also associate each electron with an
arrival
%time
totaltime=max(arrival)-min(arrival);
risetime=4; %rise time of PMT based on photon counting
numberbins=totaltime/risetime;
[photonbin,centers]=hist(arrival,numberbins); %determines the number of
photons per bin and provides a time vector

%(numberbins)corresponding to the average arrival time in each bin
```

```
%When there are few runs, there is the possibility of there being no
electron in one of the bins.  These lines remove zeros.
[r1,c1]=find(photonbin==0);
photonbin(c1)=[];
centers(c1)=[];

%This line sets the guess values for the fitting function.  Here the
first
%value is amplitude, the second is FWHM, and the third is the location
of
%the center of the function.  The fitting function requires good guess
%values.
x=[2*pi*max(photonbin),10,max(centers)/2];
lb=[];
ub=[];
options=optimset('MaxFunEvals', 1e5, 'MaxIter', 1e5);
%These lines call the non linear least squares funciton.  lsq is for
%weighted least squares, lsqnoweight is for unweighted.
[x1,resnorm, residual1,
exitflag1]=lsqnonlin('lsq',x,lb,ub,options,photonbin,centers);
[x2,resnorm,
residual2,exitflag2]=lsqnonlin('lsqnoweight',x,lb,ub,options,photonbin,
centers);
%Here the various data are saved to matrices for each run of the loop.
%allx contains the fitting parameters, residual contains the residuals,
%exit contains the exit flags, event contains the photonbin values
(i.e.
%number of electrons in a given bin) and time contains the related
arrival
%times.  The reason for the totlength and zer factors is that the
number of
%bins can vary.  I add zeros to the function in order to make sure each
row
%is of the same length.
allx1=[allx1;x1];
z=length(photonbin);
totlength=20;
zer=zeros(1,totlength-z);
residual1=[residual1,zer];
res1=[res1;residual1];
allx2=[allx2;x2];
residual2=[residual2,zer];
res2=[res2;residual2];
exit1=[exit1;exitflag1];
exit2=[exit2;exitflag2];
photonbin=[photonbin,zer];
centers=[centers,zer];
event=[event;photonbin];
time=[time;centers];

k=k+1
end

%Calculate average values of amplitude, FWHM, and center as well as
%standard deviation for weighted least squares (w) and unweighted least
```

```
%squares
Ampmeanw=mean(allx1(:,1));
FWHMmeanw=mean(allx1(:,2));
Centermeanw=mean(allx1(:,3));

Ampmean=mean(allx2(:,1));
FWHMmean=mean(allx2(:,2));
Centermean=mean(allx2(:,3));

Ampstdw=std(allx1(:,1));
FWHMstdw=std(allx1(:,2));
Centerstdw=std(allx1(:,3));

Ampstd=std(allx2(:,1));
FWHMstd=std(allx2(:,2));
Centerstd=std(allx2(:,3));

%This plot is the comparison and signal functions
figure
plot(t,ft,t,pdf)
title('Signal and Comparison Function')
xlabel('time(ns)')
%plots the distribution of the arrival times
figure
hist(arrival)
title('Histogram of Arrival Times')
xlabel('time (ns)')
ylabel('Photons Arriving During that Time Interval')

toc
```

G.2.2 Subfunctions

```
function p=signalpdf(deltaT,T,t)
%This function defines the original signal which will be manipulated.

%p=1/2/pi*deltaT./((t-T/2).^2+(deltaT/2).^2);  %Lorentzian equation
p=2/deltaT*sqrt(log(2)/pi)*exp(-4*log(2)*((t-T/2)/deltaT).^2);
%Gaussian equation


function f=fx(pdf,deltaT,T,t)

%This function creates the comparison function used in the rejection
method.  The comparison function
%must enclose the pdf.  A good comparison function will fit the shape
of
%the signal pdf.  The comparison function must be integrable.

f=(max(pdf)-(pdf(1,1)+0.005))/(T/2).*t+(pdf(1,1)+.01);   %equation that
encloses pdf
```

```
function r=reject(pdf,deltaT,T,t,photon,A)
%This function determines the random table of arrival times based on
the
%number of photons at the detector, the signal pdf, and the comparison
%function.  It will generate a random arrival time for each photon.

i=1;
arrival=[];
track=[];
%These matrices can be utilized if more information is desired.
ytrack=[];
A1track=[];
totrack=[];

%h = waitbar(0,'Ho hum...');
while i<photon
    A1=unifrnd(0,A,1,1);            %generate random area
    t0=to(pdf,T,A1);   %Integrated fx by hand and solved for t.
    y=fx(pdf,deltaT,T,t0); %point on fx that corresponds to to
    yo=unifrnd(0,y,1,1);       %generate random y value.
    pdfo=signalpdf(deltaT,T,t0);    %pdf of the signal at to

    %The if loop determines if the selected to produces a y value that
is
    %enclosed by the signal pdf or one that is enclosed between the
    %comparison function and the signal pdf.  If the y value at to is
    %within the pdf then to is placed in the arrival matrix.  If it
isn't,
    %it is placed in the track matrix.  The track matrix is a measure
of
    %the efficiency of the comparison function.  If it is a good
function,
    %the size of the track matrix will not greatly exceed the size of
the
    %arrival matrix.

    if (yo<pdfo)&(yo>=0)
        arrival=[arrival,t0];
    else
        track=[track,t0];
    end
%     waitbar(i/photon,h)
    i=length(arrival);
%     ytrack=[ytrack,yo];
%     totrack=[totrack,t0];
%     A1track=[A1track,a11];
    x=length(track);
end
% close(h)
r=arrival;
efficiency=i/x;
```

```
function t=to(pdf,T,A1)
%This function creates the integral of the comparison function and
solves for the time at which the integral is equal to
%a randomly generated area.  In this case the function is analytical,
but
%it may be possible to do this numerically.  hmmm....

m=(max(pdf)-(pdf(1,1)+.005))/(T/2);
b=(pdf(1,1)+.01);
t=(-b+sqrt(b^2-4*m/2*(-A1)))/m;


function l=lsq(x,y,t)
%This function creates the equation that is minimized by the nonlinear
%least squares fitting function.  This provides the weighted fitting.

Amp=x(1);
FWHM=x(2);
center=x(3);
sigma=sqrt(y);  %Poisson dist.
ycalc=Amp.*2/FWHM*sqrt(log(2)/pi)*exp(-4*log(2)*((t-center)/FWHM).^2);
%Calculation of Gaussian based on fitting
l=1./sigma.*(y-ycalc);  %Function to be minimized.  The least squares
fitting will minimize the sum of the squares of this function.


function l=lsqnoweight(x,y,t)
%This function creates the equation that is minimized by the nonlinear
%least squares fitting function.  This provides the unweighted fitting.

Amp=x(1);
FWHM=x(2);
center=x(3);
sigma=1;
ycalc=Amp.*2/FWHM*sqrt(log(2)/pi)*exp(-4*log(2)*((t-
center)/FWHM).^2);%Calculation of Gaussian based on fitting
l=1./sigma.*(y-ycalc);  %Function to be minimized.  The least squares
fitting will minimize the sum of the squares of this function.
```

Appendix H Codes Related to S6 Model of Rayleigh Scattering

The following sections contain the codes used to calculate the theoretical Rayleigh scattering spectrum. Unless otherwise noted the code is written in Fortran.

H.1 EES code

This code calculates the constants required by the S6 code written by Tenti, et al.

$$Tmaxsep = 58.5 \quad \text{[K] estimate of max temperature separation in vortex tube for atomics, T radial separation = 21.9}$$

$$fluid\$ = \text{'argon'} \quad \text{fluid identification}$$

$$\theta = 90 \quad \text{[degrees] angle between input laser beam and output scattering}$$

$$\lambda = \frac{1 \times 10^{7}}{12985.17} \quad \text{[nm] laser wavelength}$$

$$P = 14.7 \cdot \left| 0.068948 \cdot \frac{bar}{psi} \right| \quad \text{[bar] pressure}$$

$$Ppsi = P \cdot \left| 14.5038 \cdot \frac{psi}{bar} \right|$$

$$P1 = P \cdot \left| 100000 \cdot \frac{Pa}{bar} \right| \quad \text{[Pa]}$$

$$Tmean = 300 \quad \text{[K] input compressed air temperature}$$

$$m = \frac{\textbf{MolarMass}(fluid\$)}{6.022169e26 \ \text{[1/kmole]}} \quad \text{[kg] molar mass of the fluid}$$

$$kb = 1.381 \times 10^{-23} \quad \text{[J/K] Boltzmann's constant}$$

$$Tmin = Tmean - \frac{Tmaxsep}{2} \quad \text{[K] minimum temperature}$$

$$Tmax = Tmean + \frac{Tmaxsep}{2} \quad \text{[K] maximum temperature}$$

$$K = 4 \cdot \frac{\pi}{\lambda \cdot \left| 1.0 \times 10^{-9} \cdot \frac{m}{nm} \right|} \cdot \sin\left[\frac{\theta}{2}\right] \quad \text{[1/m] constant used in calculations}$$

Variables determined based on Tmin

$\mu_{min} = \mathbf{Visc}(fluid\$, T = Tmin, P = P1)$ [kg/m-s] viscosity of the fluid

$tc_{min} = \mathbf{k}(fluid\$, T = Tmin, P = P1)$ [W/m-K] thermal conductivity of the fluid

$$etalam_{min} = kb \cdot \frac{\mu_{min}}{tc_{min} \cdot m}$$ [ ] input for S6 code

$$nu0_{min} = \sqrt{kb \cdot \frac{Tmin}{m}}$$ [m/s] thermal velocity

$$y_{min} = \frac{P1}{\sqrt{2} \cdot K \cdot nu0_{min} \cdot \mu_{min}}$$ input for S6 code

Variables determined based on Tmax

$\mu_{max} = \mathbf{Visc}(fluid\$, T = Tmax, P = P1)$ [kg/m-s] viscosity of the fluid

$tc_{max} = \mathbf{k}(fluid\$, T = Tmax, P = P1)$ [W/m-K] thermal conductivity of the fluid

$$etalam_{max} = kb \cdot \frac{\mu_{max}}{tc_{max} \cdot m}$$ [ ] input for S6 code

$$nu0_{max} = \sqrt{kb \cdot \frac{Tmax}{m}}$$ [m/s] thermal velocity

$$y_{max} = \frac{P1}{\sqrt{2} \cdot K \cdot nu0_{max} \cdot \mu_{max}}$$ input for S6 code

$$FOM = \frac{y_{min}}{y_{max}}$$ figure of merit

convert x axis to GHz

$$CF = \frac{\sqrt{2}}{2 \cdot \pi} \cdot K \cdot \frac{nu0_{max}}{1 \times 10^{9}}$$

H.2 S6 code

H.2.1 Main code

Tsttenti.for

```
c .. Fortran program "tsttent.for"
c .. to test Tenti subroutines
c .. calls J. Lock's subroutine TENT, which in turn calls
c     subroutines in TENTISUB as supplied by G. Tenti

c .. cv = internal specific heat/Boltzmann's constant
c       = 0 for monoatomic gases
c       = 1 for diatomic gases where rotational degrees of
c             of freedom have fully kicked in (JL)
c .. etalam = ratio of shear viscosity to thermal conductivity
c             (reciprocal of Eucken ratio = viscosity*kb/therm cond)
c .. etazet = ratio of shear viscosity to bulk viscosity
c             (bulk viscosity = 0 for monoatomic gases, so
c              let etazet = 1000 for computational purposes)
c             (for diatomic gas, the bulk viscosity depends on
```

```
c            the Cv, the rotational relaxation time, and is
c            linear in pressure. For N2 at 1 atm, published
c            values are between 1.367 and 1.407,( JL))
c .. refs.    Boley et al., Can. J. Phys, Vol. 50, p. 2173, 1972
c            Tenti et al., Can J. Phys, Vol. 52, p. 285, 1974
c            Young and Kattawar, Appl. Opt., Vol.22, p. 3668, 1983

c .. writes Tenti S6 and Gaussian spectra to file
c .. note that NX,NY,I6,Y2,Y3,IY in TENT are calculated
c       but not used in the calculation of the S6 spectrum

c .. also note that the calculation for G1 through GBAR in tenti.for
c      needs to be done only once for each spectrum

c .. R. Seasholtz, NASA Lewis
c .. revision date 2/3/94

c .. S. Sanders, UW Madison
c .. revised 7/3/02

      program tsttent

c ,, use values for cv, etalam, and etazet from Young and Kattawar
c      to compare with their figure 2

      data cv/1.0/,etalam/0.266190/,etazet/1000/,y/.961110/
      data delx/0.001/,pi/3.1415927/

      write(1,100)
100   format('       x      s6'/)

      do i = 1,3001
        call tent(y,x,cv,etalam,etazet,s6)
        write(1,101) x, s6
101      format(f20.15,2f20.15)
        x=x+delx
      enddo

      stop
      end
```

H.2.2 Subfunctions

Tentisub.for

```
c .. Subroutines for Tenti Program
c .. from G. Tenti, University of Waterloo, Sept. 7, 1989
c .. calls from J. Lock's program TENTI.FOR
c .. CALL TENT(y,x,cv,etalam,etazet,s)
c .. called by TESTTENT.FOR
c .. cv = internal specific/Boltzmann's constant
c      = 0 for monoatomic gases
c      = 1 for diatomic gases where rotational degrees of
```

```
c              of freedom have fully kicked in (JL)
c .. etalam = reciprocal of Eucker ratio = viscosity*kb/therm cond
c .. etazet = ratio of shear viscosity to bulk viscosity
c             (bulk viscosity = 0 for monoatomic gases, so
c              let etazet = 1000 for computational purposes)
c             (for diatomic gas, the bulk viscosity depends on
c              the Cv, the rotational relaxation time, and is
c              linear in pressure. For N2 at 1 atm, published
c              values are between 1.367 and 1.407,( JL))

c .. revised for MS Fortran by J. Lock
c .. revision date 12/9/90

C     SUB1.FOR
C
      SUBROUTINE IMN(INTG,NMAX,X,Y)
      COMPLEX*16 Z,INTG(10),W,UNI,ZLAM,SQ2,ACPL
      REAL*8 RSQ2,XX,YY,A
      UNI=(0.D+0,1.D+0)
      RSQ2=DSQRT(2.0D+0)
      SQ2=DCMPLX(RSQ2,0.0D+0)
      KMAX=NMAX+1
      XX=DBLE(X)
      YY=DBLE(Y)
      Z=DCMPLX(XX,YY)
      ZLAM=UNI*SQ2*Z
      K=1
      INTG(1)=UNI*W(Z)/SQ2
      AK=1.0
      A=DBLE(1.0)
      ICG=2
      GO TO 30
    5 GO TO (10,20),ICG
   10 AK=AK*(K-2)
      A=AK
      ICG=2
      GO TO 30
   20 A=0.0
      ICG=1
   30 ACPL=DCMPLX(A,0.0D+0)
      INTG(K+1)=(ACPL-ZLAM*INTG(K))*UNI
      K=K+1
      IF(K.LE.KMAX) GO TO 5
      RETURN
      END
C     SUB2.FOR
C
      COMPLEX FUNCTION W*16(Z)
      COMPLEX*16 Z,ZSQ,SRIES,TERM,TERM1,A0,A1,B0,B1,A,B,AN1,BN1
      COMPLEX*16 W1,W2,SUM,SQRPI
      REAL*8 PI,AA
      COMPLEX CZ,CZ1
      CZ=Z
      X=REAL(CZ)
```

```
      Y=AIMAG(CZ)
      PI=3.141592653589793
      PI=DSQRT(PI)
      SQRPI=DCMPLX(0.0D0,PI)
      IF((X.GE.0.0).AND.(Y.GE.0.0)) GO TO 1
      WRITE(1,1001)
 1001 FORMAT(' X AND Y ARE NOT IN THE FIRST QUADRANT')
      STOP
    1 IF((X.LE.5.0).AND.(Y.LE.1.5)) GO TO 50
      IF(Y.GE.1.5) GO TO 30
C
      N=1
      ZSQ=Z*Z
      TERM=5.0D-1/ZSQ
      SRIES=DCMPLX(1.0D0,0.0D0)
    5 N=N+1
      SRIES=TERM+SRIES
      TERM1=TERM/2/ZSQ*(2*N-1)
      CZ=TERM
      CZ1=TERM1
      XY=ABS(REAL(CZ))+ABS(AIMAG(CZ))
      XY1=ABS(REAL(CZ1))+ABS(AIMAG(CZ1))
      IF((XY.LT.1.0E-15).OR.(XY1.GT.XY)) GO TO 6
      TERM=TERM1
      GO TO 5
    6 W1=-(SRIES)/Z
      WRITE(1,1002) N,XY,XY1
 1002 FORMAT(' ASYMPTOTIC SERIES--N,XY,XY1',3X,I4,2X,2E16.5)
      W=W1
      IF(Y.NE.0.0) RETURN
c     W=SQRPI*CDEXP(-ZXQ)+W1  'changed 12/9/90
      w=sqrpi*cdexp(-zsq)+w1
      RETURN
C
   30 N=0
      A0=DCMPLX(1.0D0,0.0D0)
      A1=DCMPLX(0.0D0,0.0D0)
      B0=A1
      B1=A0
      AN1=Z
      BN1=-Z*Z+DCMPLX(5.0D-1,0.0D0)
      ICG=1
   35 A=BN1*A1+AN1*A0
      B=BN1*B1+AN1*B0
      GO TO(31,34),ICG
   31 AN1=DCMPLX(0.0D0,0.0D0)
      W1=A/B
      ICG=2
      GO TO 33
   34 W2=A/B
      W=W2
      CZ=W2-W1
      XY=ABS(REAL(CZ))+ABS(AIMAG(CZ))
      IF(XY.LT.1.0E-15) RETURN
```

```
      W1=W2
   33 A0=A1
      B0=B1
      A1=A
      B1=B
      BN1=BN1+DCMPLX(2.0D0,0.0D0)
      AA=-2.0*N-0.5
      AN1=AN1+DCMPLX(AA,0.0D0)
      N=N+1
      IF(N.LT.80) GO TO 35
      WRITE(6,1003) N,XY
 1003 FORMAT(' CONTINUED FRACTION--N,XY',3X,I4,2X,E16.5)
      RETURN
C
   50 N=1
      ZSQ=Z*Z*DCMPLX(-2.0D0,0.0D0)
      SUM=DCMPLX(1.0D0,0.0D0)
      TERM=ZSQ/(3.0D0)
   55 SUM=SUM+TERM
      N=N+1
      TERM=TERM*ZSQ/(2*N+1)
      W1=TERM/SUM
      CZ=W1
      XY=ABS(REAL(CZ))+ABS(AIMAG(CZ))
      IF(XY.LT.1.0E-15) GO TO 60
      IF(N.LT.3000) GO TO 55
      WRITE(1,1004) N,XY
 1004 FORMAT(' POWER SERIES--N,XY',3X,I4,2X,E16.5)
   60 SUM=SUM*(-2.0)*Z
      W=SQRPI*CDEXP(ZSQ/2.0)+SUM
      RETURN
      END
C     SUB3.FOR
C
      SUBROUTINE S6GET(Y1,G11,GP11,G10,GP10,G2,G011,INTG,IE,S,SE)
      COMPLEX*16 INTG(10),GAM(5,5),B(6,6),C(6),BE(4,4),CE(4)
      COMPLEX*16 UNIT,ONE,ZERO
      REAL*8 BB(12,12),CC(12),BBE(8,8),CCE(8)
      UNIT=(0.D0,1.D0)
      ONE=(1.D0,0.D0)
      ZERO=(0.D0,0.D0)
      PI=3.14159265
      CALL GAMMA(GAM,INTG,4)
        DO 10 I=1,4
      IF(I.LE.3) K=I
      IF(I.EQ.4) K=5
      C(I)=GAM(K,1)
      B(I,1)=-Y1*GAM(K,1)
      B(I,2)=-Y1*GAM(K,2)
      B(I,3)=-Y1*(G11-.5)*GAM(K,3)
      B(I,4)=-Y1*(G10-.5)*GAM(K,5)
      B(I,5)=-Y1*GP10*GAM(K,5)
      B(I,6)=-Y1*GP11*GAM(K,3)
      IF(IE.EQ.0) GO TO 10
```

```
      CE(I)=C(I)
      BE(I,1)=B(I,1)
      BE(I,2)=B(I,2)
      BE(I,3)=-Y1*GAM(K,3)/3.
      BE(I,4)=-Y1*GAM(K,5)
   10 CONTINUE
        DO 14 I=1,4
        DO 15 J=1,4
      IF(I.NE.J) GO TO 15
      B(I,J)=B(I,J)-ONE
      IF(IE.EQ.1) BE(I,J)=BE(I,J)-ONE
   15 CONTINUE
   14 CONTINUE
      C(5)=ZERO
      C(6)=ZERO
      B(5,1)=ZERO
      B(5,2)=ZERO
      B(5,3)=-Y1*GP11*GAM(1,2)
      B(5,4)=-Y1*GP10*GAM(1,1)
      B(5,5)=-Y1*(G2-.5)*GAM(1,1)-ONE
      B(5,6)=-Y1*(G011-.5)*GAM(1,2)
      B(6,1)=ZERO
      B(6,2)=ZERO
      B(6,3)=-Y1*GP11*GAM(2,2)
      B(6,4)=-Y1*GP10*GAM(2,1)
      B(6,5)=-Y1*(G2-.5)*GAM(2,1)
      B(6,6)=-Y1*(G011-.5)*GAM(2,2)-ONE
        DO 17 I=1,6
      CC(I)=C(I)
      CC(I+6)=-UNIT*C(I)
      IF((I.GT.4).OR.(IE.EQ.0)) GO TO 19
      CCE(I)=CC(I)
c     CCE(II+4)=-UNIT*CE(I)  'changed 12/9/90
      cce(I+4)=-unit*ce(I)
   19   DO 18 J=1,6
      BB(I,J)=B(I,J)
      BB(I+6,J+6)=BB(I,J)
      BB(I,J+6)=UNIT*B(I,J)
      BB(I+6,J)=-BB(I,J+6)
      IF((I.GT.4).OR.(J.GT.4).OR.(IE.EQ.0)) GO TO 18
      BBE(I,J)=BE(I,J)
      BBE(I+4,J+4)=BBE(I,J)
      BBE(I,J+4)=UNIT*BE(I,J)
      BBE(I+4,J)=-BBE(I,J+4)
   18 CONTINUE
   17 CONTINUE
      CALL SIMQ(BB,CC,12,KS,12)
      IF(KS.EQ.1) WRITE(1,1005)
 1005 FORMAT(' MATRIX BB6 IS SINGULAR')
      S=CC(1)/PI
      IF(IE.EQ.1) GO TO 32
      SE=0.
      RETURN
   32 CALL SIMQ(BBE,CCE,8,KS,8)
```

```
      IF(KS.EQ.1) WRITE(1,1006)
 1006 FORMAT(' MATRIX BBE6 IS SINGULAR')
      SE=CCE(1)/PI
      RETURN
      END
C     SUB4.FOR
C
      SUBROUTINE GAMMA(GAM,INTG,INDEX)
      COMPLEX*16 INTG(10),INTMN,GAMA,GAM(5,5)
      REAL*8 CRL,BARNES,BIGG
      INTEGER IRME(5)/0,0,1,0,1/
      INTEGER LME(5)/0,1,1,2,0/
        DO 100 IME=1,5
      IF(IME.EQ.INDEX) GO TO 100
      IR=IRME(IME)
      L=LME(IME)
        DO 200 JME=1,5
      IF(JME.EQ.INDEX) GO TO 200
      IRT=IRME(JME)
      LT=LME(JME)
   10 CRL=DBLE(1.0)/DBLE(2.0**(1.5*(L+LT)+1.0))
      CRL=CRL*(BARNES(1.0,2*L)/BARNES(1.0,L)**2)*(BARNES(1.0,2*LT)/
     CBARNES(1.0,LT)**2)/DSQRT(BARNES(1.0,IR)*BARNES(1.0,IRT))
   15 CRL=CRL*DSQRT((2*L+1)*(2*LT+1)/BARNES(0.5,L+IR+1)/BARNES(0.5,LT+
     CIRT+1))
      KM=L/2+1
   20 KMT=LT/2+1
      JM=IR+1
      JMT=IRT+1
      GAMA=0.0
   30   DO 70 J=1,JM
          DO 70 JT=1,JMT
          DO 70 K=1,KM
          DO 70 KT=1,KMT
      BIGG=DBLE((-1.0)**(J+JT+K+KT))/DBLE(2.0**(2*(K+KT)-4+JM-J+JMT-JT))
   40 BIGG=BIGG*BARNES(JM-J+1.0,J-1)/BARNES(1.0,J-1)*BARNES(JMT-JT+1.0,
     CJT-1)/BARNES(1.0,JT-1)
      BIGG=BIGG*BARNES(IRT+LT+2.5-JT,JT-1)/BARNES(LT+1.5-KT,KT-1)*BARNES
     C(IR+L+2.5-J,J-1)/BARNES(L+1.5-K,K-1)
      BIGG=BIGG*BARNES(L-2*K+3.0,2*(K-1))/BARNES(1.0,K-1)*BARNES(LT-2*KT
     C+3.0,2*(KT-1))/BARNES(1.0,KT-1)
   42 GAMA=BIGG*INTMN(IR+IRT-J-JT+K+KT,L+LT-2*(K+KT)+4,INTG)+GAMA
   70 CONTINUE
   90 GAMA=GAMA*CRL*DSQRT(2.0D0)
      GAM(IME,JME)=GAMA
  200 CONTINUE
  100 CONTINUE
      RETURN
      END
C     SUB5.FOR
C
      REAL FUNCTION BARNES*8(B,M)
      BARNES=1.0D0
      IF(M.EQ.0) RETURN
```

```
      DO 10 N=1,M
     BARNES=BARNES*(B+DFLOAT(N-1))
   10 CONTINUE
     RETURN
     END
C    SUB6.FOR
C
     COMPLEX FUNCTION INTMN*16(M,N,INTG)
     COMPLEX*16 INTG(10)
     REAL*8 SUBS,BARNES
    1 IP=0
     INTMN=(0.0D+0,0.0D+0)
    5 IQMX=M-IP
    7 SUBS=0.0D+0
   10 IQ=0
   15 SUBS=BARNES(0.5,IQ)/BARNES(1.0,IQ)*BARNES(0.5,M-IP-IQ)/
    CBARNES(1.0,M-IP-IQ)+SUBS
     IQ=IQ+1
     IF((IQ-1).LT.IQMX) GO TO 15
     INTMN=SUBS*INTG(N+2*IP+1)*(2.0D+0**(M-IP))/BARNES(1.0,IP)+INTMN
     IP=IP+1
     IF((IP-1).LT.M) GO TO 5
     INTMN=INTMN*BARNES(1.0,M)
   30 RETURN
     END
C    SUB7.FOR
C
     SUBROUTINE SIMQ(A,B,N,KS,M)
     REAL*8 A(M,M),B(1),TOL,BIGA,SAVE
     TOL=0.0
     KS=0
      DO 65 J=1,N
     JY=J+1
     BIGA=0
      DO 30 I=J,N
C
     IF(DABS(BIGA)-DABS(A(I,J))) 20,30,30
   20 BIGA=A(I,J)
     IMAX=I
   30 CONTINUE
C
     IF(DABS(BIGA)-TOL) 35,35,40
   35 KS=1
     RETURN
C
   40   DO 50 K=J,N
     SAVE=A(J,K)
     A(J,K)=A(IMAX,K)
     A(IMAX,K)=SAVE
C
   50 A(J,K)=A(J,K)/BIGA
     SAVE=B(IMAX)
     B(IMAX)=B(J)
     B(J)=SAVE/BIGA
```

```
C
      IF(J-N) 55,70,55
   55   DO 65 IX=JY,N
        IT=J-IX
          DO 60 JX=JY,N
   60 A(IX,JX)=A(IX,JX)-(A(IX,IX+IT)*A(IX+IT,JX))
   65 B(IX)=B(IX)-(B(J)*A(IX,IX+IT))
C
   70 NY=N-1
        IT=N*N
          DO 80 J=1,NY
        IB=N-J
        IC=N
          DO 80 K=1,J
        B(IB)=B(IB)-A(IB,IC)*B(IC)
   80 IC=IC-1
        RETURN
        END
```

Tenti.for

```
C     PROGRAM TENTI.FOR
C
      SUBROUTINE TENT(Y,X,CV,ETALAM,ETAZET,S)
      COMPLEX*16 INTG(10)
      NY=1
      NX=1
      I6=1
C
      G11=5./6.-(5./9.)*((CV/(1.5+CV))**2)*ETAZET
      GP11=SQRT(5./(2.*CV))*ETAZET*((CV/(1.5+CV))**2)/3.
      GP11=-GP11
      G10=1.5-(2./3.)*ETAZET*(CV/(1.5+CV))**2
      GP10=ETAZET*SQRT(2.*(CV**3)/3.)/(1.5+CV)**2
      GP10=-GP10
      G2=1.5-ETAZET*CV/(1.5+CV)**2
      G011=.4*(1.5+CV)**2+CV*(1.+CV/3.)*ETAZET+((CV/(1.5+CV))*ETAZET)**2
     C/(6.*ETALAM)
      DEN=4./15.-ETALAM+(2./9.)*ETAZET*(CV/(1.5+CV))**2
      G011=G011/DEN
      G011=G011*2.*CV*ETALAM/(3.*(1.5+CV)**2)
      G011=1.5-G011
C
      IY=1
      DTBAR=1./(ETALAM*(2.5+CV)*2.*Y)
      GBAR=(4./3.+1./ETAZET)/(2.*Y)+DTBAR/(1.5+CV)
c     Y2=1.5*Y
c     Y3=H*Y
      S6=0.
      CALL IMN(INTG,6,X,Y)
      CALL S6GET(Y,G11,GP11,G10,GP10,G2,G011,INTG,0,S6,S6E)
      S=S6
      RETURN
      END
```

Appendix I Pictures of Experimental Setup

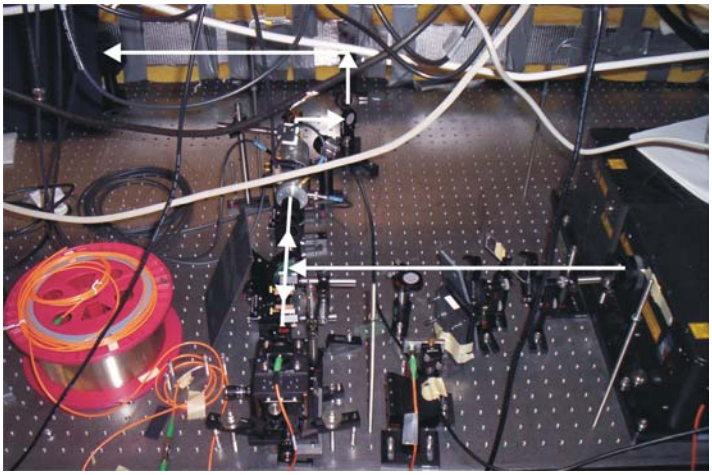

Figure I-1 Initial portion of the fiber measurement setup. The fiber is on a spool and the laser is at the right. The light path is indicated by the arrows.

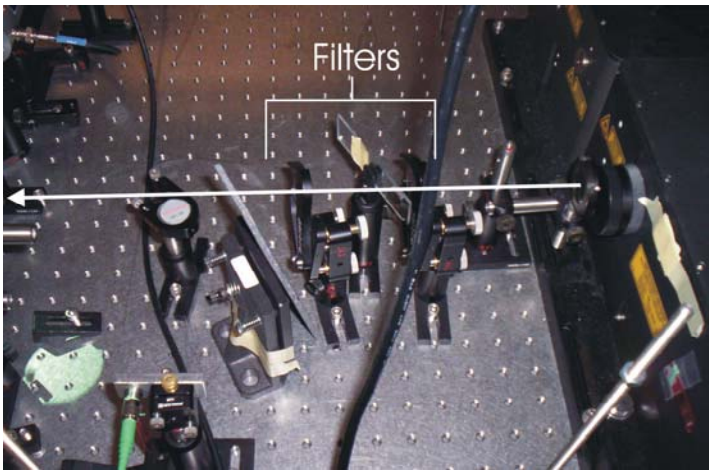

Figure I-2 Portion of the setup closest to the laser. An iris is placed near the laser output in order to block stray light from the laser and prevent reflections from entering the laser. The flipper mirror can be flipped up in order to direct the laser into the fiber at the bottom left of the figure. This fiber can be coupled to the scattering fiber for alignment purposes.

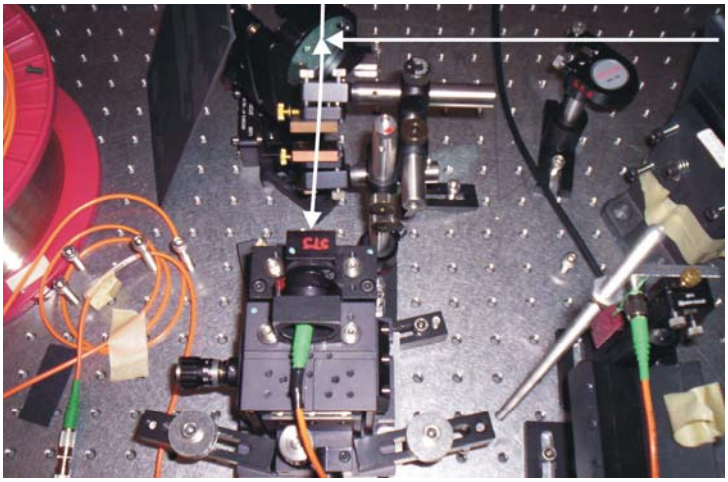

Figure I-3 Close up of the scattering fiber. The laser reflects off of a beam splitter. Two mirrors are then used to elevate the laser to the height of the fiber. An aspheric lens focuses the light into the fiber. The fiber alignment is optimized using a micrometer stage.

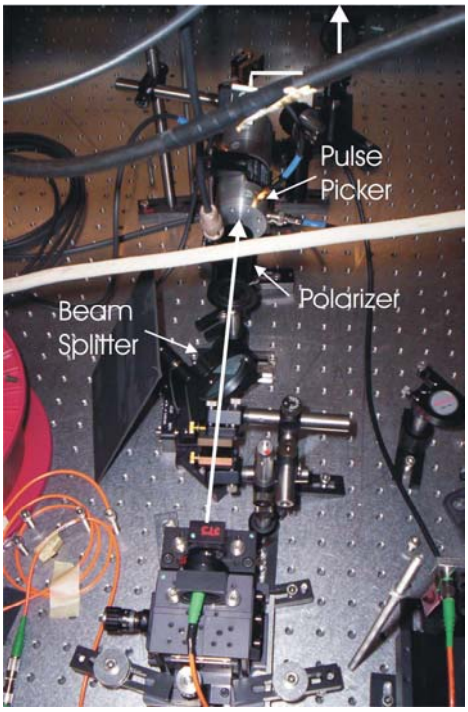

Figure I-4 The scattered light passes through the beam splitter, polarizer, and pulse picker.

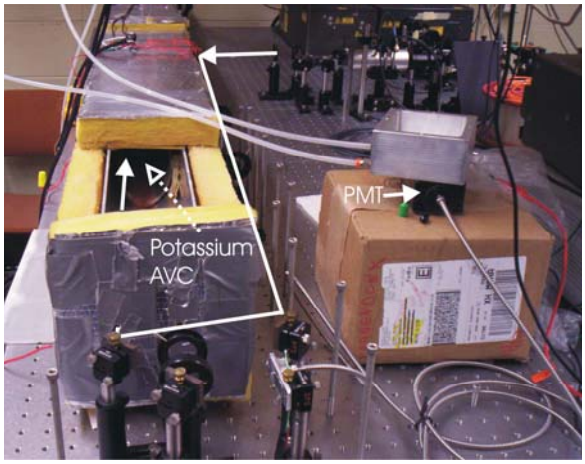

Figure I-5 The laser light is directed into the potassium AVC. The light is focused at the entrance to the White-cell and then expands through the AVC. The PMT is seen at the right with the water cooled aluminum block on top. A metal fiber is used to prevent room light from entering the PMT.

Figure I-6 Close up of the optics at the entrance and exit of the White-cell. The output is focused through a lens and into a metal fiber with a core diameter of 600 μm.

Figure I-7 This is a view of the large 50.8 mm White-cell mirror.

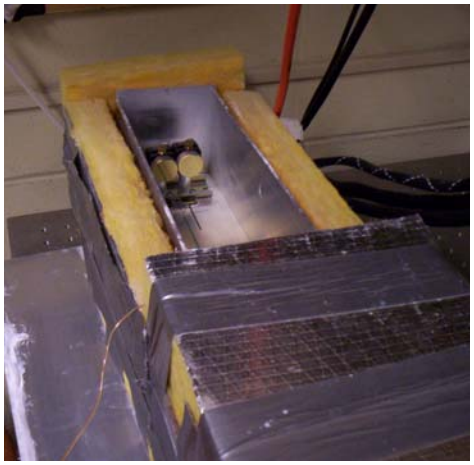

Figure I-8 This is an image of the small 25.4 mm White-cell mirrors.

Figure I-9 This is a picture of the entire setup. The cold finger in the AVC which was used to keep the center cooler than the ends is shown. The area around the White-cell input/output is covered by fabric to eliminate stray room light.